UNIVERSITÀ DEGLI STUDI DI TRIESTE

XXXVIII CICLO DEL DOTTORATO DI RICERCA IN INGEGNERIA INDUSTRIALE E DELL'INFORMAZIONE

High Frequency Transceiver Systems For Small Satellites From Ka Band Towards Q/V

Settore scientifico-disciplinare: **ING-INF/01 ELETTRONICA**

DOTTORANDO / A
SIMONE PAULETTO
Simone Pauletto

COORDINATORE
PROF. FULVIO BABICH
Babich

SUPERVISORE DI TESI
PROF. SERGIO CARRATO

CO-SUPERVISORE DI TESI
PROF.SSA ANNA GREGORIO

ANNO ACCADEMICO 2024/2025

UNIVERSITÀ DEGLI STUDI DI TRIESTE

Dipartimento di Ingegneria e Architettura

XXXVIII Ciclo del Dottorato di Ricerca in
Ingegneria Industriale e dell'Informazione

High frequency transceiver systems for small satellites, from Ka band towards Q/V

Dottorando	Supervisore
Simone Pauletto	**Chiar.mo Prof. Sergio Carrato**
	Co-Supervisore
	Prof.ssa Anna Gregorio

Anno Accademico 2024/2025

Abstract

This thesis addresses the design, prototyping, and evaluation of a Q/V–band satellite front–end for small spacecraft that supports two operating modes: a transparent (bent–pipe) frequency conversion payload and a regenerative transceiver when attached to commercial modems or software–defined radios (SDRs). Motivated by the migration of feeder links toward Q/V band for capacity scaling, this thesis addresses a lack of publicly documented regenerative prototypes at these frequencies, proposing a device–first, modular methodology intended to maximize reproducibility in academia and early–stage industry.

A superheterodyne architecture with a common intermediate frequency (IF) of 5.7 GHz is developed to cover Q–band downlink (37.5–42.5 GHz) and V–band uplink (47.2–52.4 GHz). Breadboarding and measurements validate the main subsections; behavioural models (AM/AM, AM/PM, phase noise) and waveform–level simulations quantify constellation impairment and symbol error rates versus SNR, determining output–back–off choices. A link–budget study with the synthesized front-end (FE) parameters illustrates clear–sky margins and the sensitivity to propagation fades showing how multi-Gigabit links can be achieved with considerable margin.

The activities were partially founded by PICOSATS S.r.l. (Trieste, Italy) and all measurements took place in their laboratories. The results demonstrate that Q/V–band front–ends for small satellites can be reliably realized with commercial off–the–shelf components at low cost and short lead time while enabling regenerative experiments with SDRs/modems that remain under–represented in the open literature. The thesis contributes a practical hardware platform and a repeatable methodology for research at millimetre–wave.

Sommario

Questa tesi affronta la progettazione, la prototipazione e la valutazione di un front–end satellitare in banda Q/V per piccoli satelliti, capace di operare in due modalità: come payload trasparente (bent–pipe) a sola conversione di frequenza e come ricetrasmettitore rigenerativo da collegare a modem commerciali o a software defined radio (SDR). Spinta dalla migrazione dei feeder link verso la banda Q/V per aumentare la capacità, questa tesi colma la scarsità di prototipi rigenerativi documentati in pubblicazioni scientifiche a tali frequenze, proponendo una metodologia modulare basta interamente su componenti commerical off-the-shelf (COTS) pensata per massimizzare la riproducibilità in ambito accademico e nelle fasi iniziali dell'industrializzazione.

È stata sviluppata un'architettura supereterodina con una frequenza intermedia (IF) comune di 5.7 GHz che copre downlink in banda Q (37.5 – 42.5 GHz) e uplink in banda V (47.2–52.4 GHz). Vengono presentate prove su breadboard e misure che validano le principali sottosezioni; attraverso modelli comportamentali (AM/AM, AM/PM, rumore di fase) e simulazioni a livello di forma d'onda viene valutato il degrado delle costellazioni e il tasso di errore di simbolo in funzione del rapporto segnale–rumore, determinando le scelte di *output back–off*. Viene presentato inoltre uno studio di link budget, basato sui parametri del FE progettato, che mette in evidenza i margini in cielo sereno e la sensibilità alle attenuazioni di propagazione, mostrando come collegamenti multi–gigabit siano ottenibili con margini considerevoli.

Le attività sono state parzialmente finanziate da PICOSATS S.r.l. (Trieste, Italia) e si sono interamente svolte presso i loro laboratori. I risultati dimostrano che front–end in banda Q/V per piccoli satelliti possono essere realizzati in modo credibile con componenti commerciali off–the–shelf, a basso costo e con tempi ridotti, abilitando al contempo esperimenti rigenerativi con SDR/modem ancora poco rappresentati nella letteratura accademica. La tesi fornisce una piattaforma hardware pratica e una metodologia ripetibile per la ricerca alle onde millimetriche.

Contents

Acronyms

ACM adaptive coding and modulation.

ADC analog-to-digital converter.

ADI Analog Devices.

ADS-B automatic dependent survelliance-broadcast.

AIS automatic identification system.

ALC automatic level control.

AM amplitude modulation.

AWGN average white gaussian noise.

BDUA broadband distributed user access.

CCSDS Consultative Committee for Space Data Systems.

CMOS complementary metal oxide semiconductor.

COTS commercial off the shelf.

DAC digital-to-analog converter.

DC direct current.

DSA digital step attenuator.

DSP digital signal processor.

DTP digital transparent processor.

DVB-S2X Digital Video Broadcasting Satellite Second Generation Extensions.

DVB-S2 Digital Video Broadcasting Satellite Second Generation.

EDRS European data relay system.

EHF extremely high frequency.

EIRP equivalent isotropic radiated power.

EM engineering model.

eMBB enhanced mobile broadband.

EMC electro-magnetic compatibility.

EO earth observation.

EVB evaluation board.

EVM error vector magnitude.

FE front-end.

FET field-effect transistor.

FIR finite impulse response.

GEO geostationary earth orbit.

GGW groove-gap waveguide.

GSaaS ground station as a service.

HAPS high-altitude platform station.

HEMT high electron mobility transistor.

IC integrated circuit.

IF intermediate frequency.

IFC in-flight connectivity.

IIP3 input intercept-point of third order.

IIR infinite impulse response.

ITU International Telecommunication Union.

LEO low earth orbit.

LNA low noise amplifier.

LO local oscillator.

LSB lower-side band.

MDS minimum detectable signal.
MEC multi-access edge computing.
MEO medium earth orbit.
MMIC monolithic microwave integrated circuit.
mMTC massive machine-type communications.
MODCOD modulation and coding.

NDA non-disclosure agreement.
NF noise figure.
NFV network functions virtualization.
NR New Radio.
NTN non-terrestrial network.

OBO output back off.

PA power amplifier.
PAE power added efficiency.
PCB Printed Circuit Board.
PFD phase frequency detector.
PIMT propagation impairment mitigation techniques.
PLL phase locked loop.
PM phase modulation.

RF radio frequency.
RSSI received signal strength indicatior.

SAR synthetic aperture radar.
SDN software defined networking.
SDR software defined radio.

SEE single event effect.

SEFI single event functional interrupt.

SEL single event latch-up.

SER symbol error rate.

SEU single event upset.

SFDR spurious free dynamic range.

SIW substrate integrated waveguide.

SMT Surface Mount Technology.

SNR signal to noise ratio.

SSPA Solid State Power Amplifier.

SSPP spoof-surface-plasmon-polariton.

TID total ionizing dose.

TWT travelling wave tube.

UAV unmanned aerial vehicles.

ULPC up-link power control.

URLLC ultra-reliable low-latency communications.

USB upper-side band.

VCO voltage controlled oscillator.

VGA variable gain amplifier.

VLEO very low earth orbit.

VSAT very small aperture terminal.

VVA voltage variable attenuator.

WG waveguide.

WR rectangular waveguide designation.

Introduction

In the last decade the so–called *New Space* paradigm has transformed the space economy and, in particular, the small-satellite segment. The steady miniaturization and performance improvement of electronic components now allow small spacecraft to host advanced payloads and to deliver a wide range of services that were formerly possible only on large platforms. In lower orbits the radiation environment is less harsh than in GEO, relaxing parts of the environmental constraints on electronics and materials and so opening the door to the use of commercial off–the–shelf (COTS) components. This, in turn, shortens development cycles and reduces cost and risk for both industry and academia, widening access to space systems and experimentation. In parallel, the market has expanded from a small sector largely characterized by national agencies and defense actors to an increasingly transversal domain where private companies design, launch, and operate constellations to provide services directly to the consumer. Among all applications, broadband and narrowband telecommunications remain the most prominent drivers, also under the momentum of 5G/6G non–terrestrial networks (NTN) and related standardization efforts and funding initiatives.

Within this context, feeder links are progressively migrating from Ka to Q/V band to unlock contiguous multi–GHz spectrum, to facilitate co-existence between service links and feeder links, and to exploit the higher antenna gain available at millimetre–wave frequencies. Q/V operation, however, raises concrete challenges in front–end (FE) design: low–phase–noise local oscillators above 40 GHz, compact and low–loss filters, linear and efficient power amplification, and receiver noise figures compatible with high–order DVB–S2/S2X modulations. Moreover, while the open literature contains several studies and a few in–orbit demonstrations of transparent (bent–pipe) Q/V transponders, publicly documented regenerative Q/V transceivers suitable for small satellites remain scarce. This motivates research prototypes that can be reproduced and evolved in academic and industrial settings.

The objective of this work is to design, prototype, and evaluate a high–frequency satellite front–end (FE) that covers the practical Q/V feeder link ranges (Q–band downlink around 37.5–42.5 GHz and V–band uplink around 47.2 – 52.4 GHz) operating in two modes: first as a transparent bent-pipe payload but also as a regenerative transceiver when attached to commercial modems or software–defined radios (SDRs). The design philosophy deliberately privileges COTS devices and modular PCB assemblies over custom MMICs, to demonstrate feasibility at lower cost and lead time, and to maximize reproducibility for research and education. The work adopts a device–first process:

- start from the best–available packaged components;
- architect a coherent superheterodyne FE around a common intermediate frequency (IF);
- breadboard and measure each subsection;
- model the end–to–end behaviour at waveform level (AM/AM, AM/PM, phase noise) and at link level (margin and availability).

A classical superheterodyne topology is selected because present direct–RF data–converters do not span the full Q/V range, and a homodyne (direct–conversion) approach at 40–50 GHz would demand accurate quadrature generation and very power demanding and impractical LO chain. The chosen IF is 5.7 GHz, derived from a spurious–analysis trade–off and from the need to interface existing SDRs. On the receive side (V band) the FE employs packaged LNAs and a broadband mixer driven by a two–stage active multiplication LO chain followed by a filtering and amplifying IF chain; on the transmit side (Q band) the chain combines the same IF components as the receiver, an up–converter with a two–stage active multiplication LO chain, and a 6W power amplifier stage driven by two Q-band driver stages. The IF sections of both the receiver and the transmitter include programmable attenuation to enable automatic level control and to support both narrowband transparent operation and widerband SDR–based testing. Throughout the design, bias sequencing and protection are addressed explicitly for depletion–mode GaAs/GaN devices.

The research project was partially funded by PICOSATS S.r.l. (Trieste, Italy) and all design, assembly, and testing activities were carried out at their laboratories. Working within an industrial R&D workflow shaped the emphasis on packaged COTS parts, repeatable biasing and measurement procedures, and compatibility with existing ground assets. The resulting prototype is expressly intended to operate not only as a transparent FE but also in regenerative scenarios by attaching SDRs/modems at IF, an operating mode that is still largely absent from the available state of the art at Q/V band for small satellites.

Chapter 1 reviews the state of the art of Q/V–band space transceivers, from New Space drivers and standards to enabling components and the few reported transparent Q/V payloads. Chapter 2 introduces the project objective and COTS–oriented design philosophy, compares canonical transceiver topologies, and motivates the adoption of a superheterodyne architecture with a common IF. Chapter 3 details the V–band receiver, including the LO chain, RF front–end, and IF stages, together with breadboarding and measurements. Chapter 4 presents the Q–band transmitter design and measurements. Chapter 5 develops the behavioural models, the waveform level evaluation (constellation impairment and SER vs. SNR with back–off optimization), and the link budget built on the measured FE parameters. The thesis closes with the conclusions and directions for future work.

During this research, the following publications were produced, and their findings are also incorporated into this thesis.

- Pauletto S., Sesto Gorella N., Zanchetta F., Zebochin I. E., Fragiacomo M., Gregorio A., Carrato S., "A K/Ka Band 5G Satellite Payload For LIDE Mission", 2025 IEEE Proceedings Of EuMC – European Microwave Conference, (accepted 16/06/2025).

- Adamo F., Simoncini G., Pauletto S., Carrato S., Gregorio A., "Design of a 17.3-21.2 GHz SATCOM Upconverter Based On COTS With Low Spurious Emission", 2025 IEEE Space Hardware and Radio Conference, SHaRC 2025, pp. 12 - 15, DOI: 10.1109/SHARC63955.2025.10908962.

- Parigi F., Deva L., Pauletto S., Adamo F., Perticaroli S., Cheikh A., Vallauri R., Vicentini A., "IOD Mission For Direct 5G Broadband Access From LEO" (2025) Proceedings Of SPIE - The International Society For Optical Engineering, 13546, Art. No. 1354642, DOI: 10.1117/12.3062775.

- Orecchini G., Schiavolini G., Mezzanotte P., Pauletto S., Loppi A., Beltramello A., Dogo F., Manià D., Palazzi V., Simoncini G., Roselli L., Gregprio A., Fragiacomo M., Alimenti F., "Low-Noise Block Downconverter Based On COTS And SIW Filters For Ku-Band Cubesat Transponders", 2023 IEEE Space Hardware and Radio Conference, SHaRC 2023, Pp. 1 - 4, DOI: 10.1109/SHARK56958.2023.10046247.

- Schiavolini G., Orecchini G., Beltramello A., Loppi A., Pauletto S., Adamo F., Gorella N.S., Dogo F., Manià D., Fragiacomo M., Palazzi V., Roselli L., Mezzanotte P., Gregorio A., Alimenti F., "Novel Architecture For Beacon Signal Generation In Satellite Applications" (2023) IEEE MTT-S International Microwave Symposium Digest, 2023 June, pp. 815 - 818, DOI: 10.1109/IMS37964.2023.10188082.

- Orecchini G., Schiavolini G., Mezzanotte P., Pauletto S., Loppi A., Beltramello A., Dogo F., Manià D., Palazzi V., Simoncini G., Roselli L., Gregorio A., Fragiacomo M., Alimenti F. "Low-Noise Ku-Band Receiver Frontend With Switchable SIW Filters For Cubesat Applications", ICECS 2022 - 29th IEEE International Conference On Electronics, Circuits And Systems, DOI: 10.1109/ICECS202256217.2022.9971113.

Moreover, the following work was published before the start of this research:

- Alimenti F., Mezzanotte P., Simoncini G., Palazzi V., Salvati R., Cicioni G., Roselli L., Dogo F., Pauletto S., Fragiacomo M., Gregorio A., "A

Ka-Band Receiver Front-End With Noise Injection Calibration Circuit For Cubesats Inter-Satellite Links" (2020) IEEE Access, 8, Art. No. 9110602, pp. 106785 - 106798, DOI: 10.1109/Access.2020.3000675.

1. State of the Art on Q/V-Band Space Transceivers

This chapter presents the state of the art on Q/V-band transceivers for space systems. It opens with an overview of satellite communications in the New Space era and the motivations for employing Q/V bands. It then surveys enabling components and technologies (e.g., LNAs, PAs, PLLs, filters), followed by a review of complete Q/V transceivers, receivers, transmitters, and transponders reported in academic literature. Subsequently, the Alphasat "Aldo Paraboni" (TDP5) mission is examined focusing on the communication payload and briefly on the scientific beacon payload, and the principal in-orbit results are summarized.

1.1 Satellite communications in the New Space era

The Satellite Communications (SatCom) market is going through a structural shift in the New Space era driven by significant reductions in launch cost, series and standard production for Small-Satellites (smallsats), and rapid advances in digital payloads and cloud access to the ground segment [1]. Multi-orbit architectures (LEO/MEO/GEO) with inter-satellite links dominated by smallsats are being employed as part of 5G/6G non-terrestrial networks (NTN), while commercial Ground Station as a Service (GSaaS) models drastically reduce data transport latencies from orbit to cloud analytics [2, 3]. Together with the IMT-2020 vision [4] and the subsequent 3GPP NTN work items [5, 6, 7], this is turning SatCom from a sector used only as backhaul and broadcast medium into a programmable, scalable infrastructure for global connectivity and data relay.

In [1], four interrelated reasons are identified that explain the changes just reported. First, new constellation types, reported as mega-LEO and hybrid MEO/GEO overlays, unlock wide-area capacity with low round-trip times, seamless handover across orbits, and improved spatial multiple access through multibeam active arrays, all made possible by industrialized manufacturing and rideshare launches [1]. Second, on-board capabilities have matured: digital transparent processors (DTPs) and regenerative payloads add flexible channelization, beamforming, precoding, dynamic routing and even on-board predistortion, which shortens control loops and enables spectrum and energy efficient operation [1]. Third, NTN standardization has converged on concrete deployment scenarios, channel models and architecture options: 3GPP TR 38.811 [5] and TR 38.821 [6] scoped NR-NTN support, while TR 38.822 [7] captured service and system aspects for satellite access in 5G, enabling the introduction of Rel-17/18 features. Finally, the New Space paradigm, where private capital is involved with vertically integrated supply chains and software operations including cloud-native ground segments, accelerates iteration and reduces risks even in more ambitious architectures [1].

Concrete applications and use cases were derived from these drivers. 5G NTN is one of the most important use cases, where satellites enhance the network reliability by ensuring service continuity, extend coverage to remote and maritime/airborne areas, and improve scalability through efficient multicast and broadcast. Within the IMT-2020 framework [4], three service families are targeted: enhanced Mobile Broadband (eMBB), aimed at high-throughput content delivery and backhaul offload for video, software updates, and cloud/edge access; massive Machine-Type Communications (mMTC), addressing very large populations of energy-constrained devices that generate sporadic low-rate telemetry (e.g., IoT sensors) over wide areas; and Ultra-Reliable Low-Latency Communications (URLLC), focused on stringent availability and service continuity for safety-critical and control applications, where NTN enhances robustness and continuity rather than latency. The SaT5G project, presented in [8], further catalogs eMBB satellite use cases including 5G backhaul for rural cells, connectivity for moving platforms, and on-demand multicast/broadcast for content distribution, and proposes reference architectures such as transparent vs. regenerative payloads, gateways based on Software-Defined Networking (SDN) and Network Functions Virtualization (NFV), and integration with Multi-access Edge Computing (MEC).

A rapidly maturing use case is the tight integration of Very-Low Earth Orbit (VLEO) constellations with SatCom-assisted aerial networks. In this multi-tier architecture, satellites in VLEO (typically 200–450 km) provide wide-area backhaul, inter-satellite routing, and control-plane functions, while airborne platforms called High-Altitude Platform Stations (HAPS), at 17-25 km, and lower-altitude Unmanned Aerial Vehicles (UAVs) act as agile access cells that can be rapidly positioned over demanding hotspots [9]. The satellite layer shortens the slant range and round-trip time relative to higher orbits and improves the link budget to small terminals, at the cost of increased aerodynamic drag and more frequent station-keeping; the aerial layer complements coverage with reconfigurable beams and rapid restoration [10]. Recent surveys quantify these operational trade-offs and control challenges, and show how VLEO/HAPS/UAV assets can be integrated with NTN to support joint communications and sensing scenarios, e.g. Synthetic Aperture Radar/communications (SAR/COM) and edge computation for timely analytics [11].

Another key application is aeronautical and maritime tracking and communications. Space-based Automatic Dependent Surveillance–Broadcast (ADS-B) and Automatic Identification System (AIS) extend global situational awareness and safety-of-life services by detecting aircraft and vessels beyond terrestrial receiver footprints. In parallel, broadband mobility, e.g. in-flight connectivity (IFC) and maritime Very Small Aperture Terminals (VSATs) support passenger internet access and airline/ship operational data links [1].

Scientific and earth observation applications remain key importance sectors for satellite communications. For Earth-observation (EO) data collection, laser-assisted GEO relays such as the European Data Relay System (EDRS) and shared ground-station networks route multi-Gb/s EO data to cloud computing regions for real-time exploitation, reducing the delay between data acquisition and decision-making [3]. Finally, for deep space communications the link budgets and delays push systems toward powerful FEC (LDPC/turbo) and robust synchronization and coding stacks as per CCSDS blue books, with satellite relays and optical feeder links emerging for next-gen missions [12, 13].

The scenarios considered require addressing several system-level aspects [1]. Constellation design must take into consideration latency, satellite revisit time, throughput capacity per served area and ISL topology across GEO/MEO/LEO/VLEO and hybrid overlays. Communication architectures are typically classified as transparent payloads or regenerative payloads: the former maximize waveform agnosticism and upgradability, the latter prioritize SNR gains and enable on-board routing and caching [1]. At the ground segment, commercial antenna farms and cloud-native infrastructures turn “space data access” into a managed interface for rapid application delivery [2]. Protocol standardization (DVB-S2/S2X for broadband; 3GPP NR-NTN for satellite access) is advancing in lockstep with a move to higher frequencies for feeder and inter-satellite links. The combined effect is a natural pull toward Q/V-band (and above), where wider spectrum supports capacity scaling and gateway densification.

1.2 Architectural drivers and the case for Q/V

More in detail, three converging reasons motivate operation at Q/V for feeder links. The first is spectrum contiguity: beyond Ka, wide adjacent allocations enable high-order modulations and multi-carrier operation. The second reason is coexistence, as freeing Ka for user links while migrating feeders to Q/V reduces cross-interference, so enabling ground station diversity. Finally link budget scaling is a strong reason to move in Q/V band, where massive

MIMO at gateways and advanced coding/modulation (DVB-S2/S2X) allow high spectral efficiency when combined with availability-oriented design [14].

More precisely, operation at Q/V for feeder links is driven by three converging factors that reinforce one another. In terms of spectrum, the contiguity and width of the ITU-R allocations above Ka are markedly larger [15]: Q/V downlink around 37.5–42.5 GHz provides roughly 5 GHz of contiguous spectrum versus about 2.5 GHz at Ka (17.7–20.2 GHz), and the uplink around 47.2–52.4 GHz totals roughly 5 GHz versus about 2.5 GHz at Ka (27.5–30.0 GHz). Depending on regional footnotes and sharing, this yields about 2× more bandwidth, enabling higher symbol rates and more carriers per gateway. From a coexistence standpoint, Ka is increasingly reserved for service (user) links; migrating feeder links to Q/V separates the high-power gateway carriers from user traffic, reducing self-interference and easing EMC/linearity constraints in both payload and ground segment, while simplifying gateway diversity without in-band coupling between feeder and service links. Finally, link-budget scaling favors Q/V because, for a given physical aperture, antenna gain grows with frequency ($G \propto f^2$), so moving from Ka to Q/V yields $\sim$6–8 dB per end (and $\sim$12–16 dB two-way) of additional gain in clear sky, enabling narrower beams, higher frequency reuse, and higher instantaneous C/N_0; when this is paired with adaptive coding and modulation (ACM), uplink power control, and multi-gateway with site diversity and high-order DVB-S2/S2X modcods, systems can achieve higher spectral efficiency despite the stronger atmospheric attenuation at Q/V [14].

The propagation penalties at EHF (gaseous absorption, rain, clouds/fog, scintillation) are well quantified in ITU-R models [16, 17, 18, 19]. At Q/V, attenuation is dominated by rain and oxygen lines, i.e. discrete absorption peaks of atmospheric O_2 notably around 60 GHz in V-band that raise the baseline path loss and cloud liquid water, and scintillation that add fast dynamics (channel variations on second-to-minute time scales driven by turbulent, convective cells). Short-term fades (deep, brief drops in received power, often tens of dB for seconds to minutes during heavy rain) are routine and spatially selective across gateway clusters. Academic studies and standards converge on a toolbox of propagation impairment mitigation techniques (PIMTs): adaptive coding and modulation (ACM), uplink power control (ULPC), gateway diversity/site switching, and frequency diversity [20, 14, 21]. In this context, DVB-S2/S2X comes again into play by providing fine-grained spectral-efficiency steps and robust LDPC/BCH coding suited to ACM under rapidly varying fades [22, 23].

1.3 Enabling components and technologies at Q/V and above

Indium Phosphide (InP) HEMT technology remains the noise benchmark for space receivers across Q,V and W. At frequencies even above ∼150 GHz, state-of-the-art InP LNAs report noise figures on the order of ∼3 dB, and when operated cryogenically can drive the system noise temperature much lower. These drivers make InP LNAs widely used in deep-space and radio-astronomy front-ends. Cryogenic operation, and more in general InP, is atypical in GEO/LEO telecom [24, 25] where Gallium Arsenide (GaAs) pHEMT LNAs achieve very competitive performance in the V band. The survey in [26] reports GaAs designs up to ∼55 GHz with noise figures around ∼2 dB, making GaAs attractive for cost/power-sensitive front-ends where W/D-band reach is not required. In [27] an InP Q/V-band LNA that delivers ∼18–20 dB gain with ∼3 dB noise figure over 33-50 GHz is presented with designs paying close attention to stability, ruggedization for thermal cycling and robustness to interfering signals. The devices was tested by injecting a millimeter-wave input power of 13 dBm for 10 minutes, and no degradation in a small signal gain was observed. That said, at V band the disadvantages of InP (higher die and packaging cost, limited foundry availability, longer lead times, and poor scale economy for high-volume builds) are not compensated by its noise-figure improvement over state-of-the-art GaAs pHEMTs, making GaAs the pragmatic choice for many designs.

Regarding power amplifiers, GaN-on-SiC MMICs have enabled watt-class saturated power into V-band, and tens of watts at Q-band. A series of academic and industrial papers detail compact Q-band SSPAs for space: a 20 W GaN-on-Si Q-band SSPA for space communication systems [28], a 20 W Q-band unit equipped with a linearizer that allows to achieve a Noise to Power Ratio (NPR) better than 16 dBc at 3 dB of Output Back-off (OBO) [29], and broader surveys on W-band GaN discussing the dispersion of parameters on a sample of 80 amplifiers (same wafer) presenting array-level implications where 1.2 W are reached in the 72 to 90 GHz range [30].

Also silicon platforms have matured into the Q/V regime for power delivery when aided by power combining. A recent JSSC paper proposes a Q/V-band SiGe HBT cascode PA that employs a novel four-way Wilkinson combiner balun to achieve compactness and high efficiency suitable for SATCOM [31]. The work emphasizes the trade-off between breakdown margin, output swing, and transformer loss at V-band, as well as the linearity vs. efficiency balance required by DVB-S2X waveforms.

On the tube side, NASA, in collaboration with L3 Technologies Electron Devices Division, (L3 EDD) and L3 Technologies Narda Microwave West (L3 NMW), has reported space-qualified Q-band helix TWTs achieving up to ∼200 W saturated power across 37.5-42.5 GHz tested with multi-gigahertz bandwidths approaching the whole 5 GHz available span [32, 33]. Such devices remain attractive for very-high-$EIRP$ broadcast carriers, while GaN SSPAs (often linearized) compete strongly in multicarrier regimes due to graceful back-off characteristics and easier redundancy management [21].

Moving to the LO chain components, to achieve low-jitter, low-spur LO distribution above 40 GHz is challenging. Representative silicon PLLs use V-band VCOs with injection-locked frequency dividers and CML ring-based prescalers [34]. W-band integer-N PLLs for 80+ GHz targets have been shown in 65 nm CMOS for Frequency Modulated Continuous Wave (FMCW) sensing [35], while silicon frequency synthesizers based on harmonic/tripler and injection techniques provide compact LO generation with acceptable phase noise for superheterodyne Q/V receivers [36].

When talking about Q/V band filters waveguide technologies offer low insertion loss and high power handling at Q/V, but SIW/LTCC integration reduces mass and volume. Surveys report SIW filter/multiplexer design flows and transitions that scale to V-band [37, 38]. New technologies are also employed such as the groove-gap waveguide (GGW) presented in [39]. They uses parallel plates lined with periodic electromagnetic-bandgap pins (an artificial magnetic conductor) that suppress parallel-plate modes, so that energy is confined to an open metal groove. This results in an all-metal device that delivers low loss and wide stopbands with excellent thermal properties suited to high power SSPAs. [39]. Another Q/V band technology is given by the advanced E-plane filters that employ split-block waveguide along the electric-field plane and load the aperture with corrugations or spoof-surface-plasmon-polariton (SSPP) structures to realize higher-order resonances, achieving strong out-of-band rejection with low insertion loss and in a compact, fabrication-friendly assembly [40].

1.4 Transponder and Transceiver Architectures in Q/V Band

Despite extensive feasibility studies, only a limited number of end-to-end Q/V-band flight experiments and pre-operative demonstrations have been reported in the open literature; two representative and widely cited milestones are the Italian TRANSPONDERS study (2009) and the Aldo Paraboni payload on Alphasat (TDP5, 2013) [41, 42].

The TRANSPONDERS activity, funded by ASI, scoped a broadband GEO system with Q/V-band feeder links and Ka-band service links in a star topology, using DVB-S2 on the forward link and an enhanced DVB-RCS on the return link. The mission scenario block diagram is shown in Figure 1.1. The reference Broadband Distributed User Access (BDUA) mission split Europe into 0.5 ° Ka spot beams (with about 64 beams) served by 8 geographically distributed gateways; feeder coverage used one Q/V beam per gateway with full reuse, assuming adequate inter-spot isolation. [41]

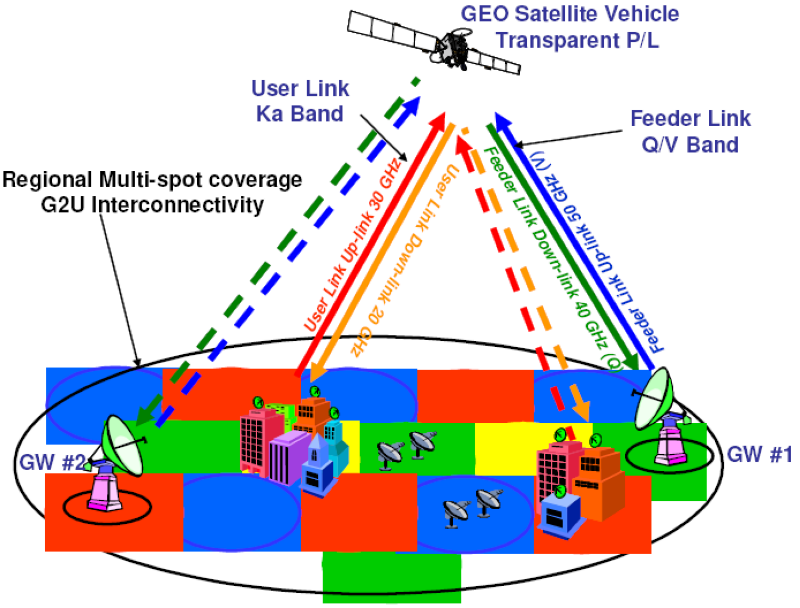

Figure 1.1: TRANSPONDERS/BDUA mission scenario (Q/V feeder; Ka service; multi-gateway star network), [41].

At payload level, TRANSPONDERS defined a transparent multi-channel architecture with separate forward and return repeaters and frequency plan partitioned across the Ka (user) and Q/V (feeder) sections. To de-risk technology and validate Propagation Impairment Mitigation Techniques (PIMTs - such as ACM, ULPC, site diversity, inter-beam partitioning), a scaled BDUA (SBDUA) payload was proposed. This is composed of a forward repeater (V/Ka), a return repeater (Ka/Q), a Q/V Rx/Tx antenna (single beam), and 8 Ka RX and 8 Ka TX antennas in order to serve 8 beams. The study reported mass/power estimates (i.e. ∼172 kg, ∼1.7 kW) and RF power figures consistent with multi-carrier DVB operation (e.g. 16 W RF per forward-link carrier with hundreds of carriers aggregated), highlighting the need for high-linearity HPAs and careful channelization [41]. The block diagram of the SBDUA payload is shown in Figure 1.2.

The Aldo Paraboni hosted payload comprises two independent subsystems: a Communication Experiment (ComEx) and a Scientific Experiment (SciEx). ComEx implements two transparent single-channel transponders, each linking one V-band uplink spot to one Q-band downlink spot. Center frequencies are 47.9/48.1 GHz (uplink) and 37.9/38.1 GHz (downlink), with 10 MHz useful bandwidth per channel. The Q/V Communication Antenna (QVCA) uses three fixed reflectors to form single-spot coverages with landing points over the cities of Tito (IT1, always active), Spino (IT2, switch-

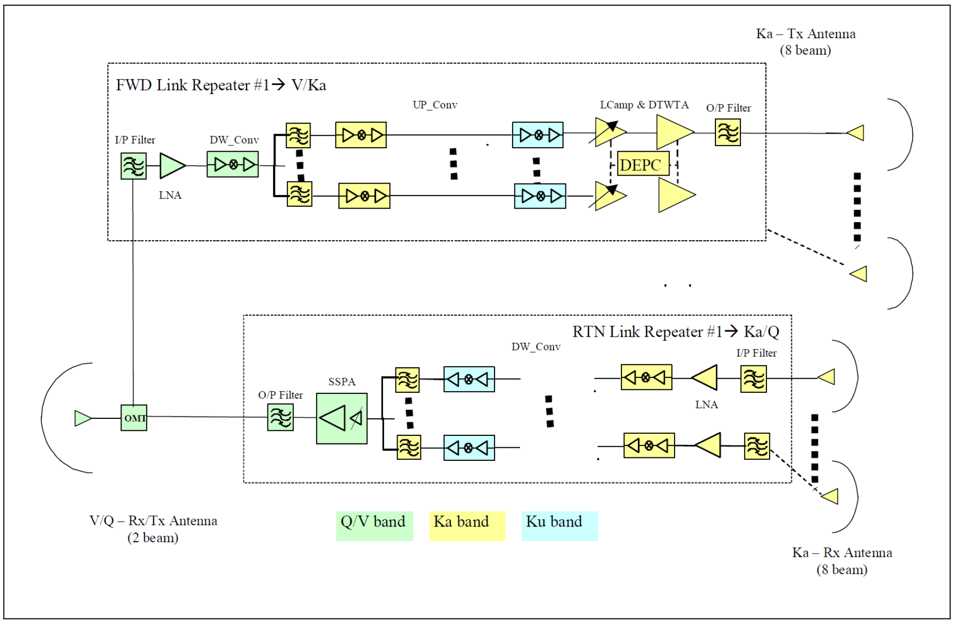

Figure 1.2: TRANSPONDERS SBDUA payload block diagram (V/Ka forward repeater; Ka/Q return repeater; Q/V single-beam and Ka 8-beam antennas), [41].

selectable), and Graz (EU1, switch-selectable). The mission scenario block diagram is shown in Figure 1.3. Payload configuration allows loop-mode (Tx/Rx within the same ground station) and cross-mode (Tx at one station, Rx at another) tests, enabling in-orbit verification of EIRP, G/T, frequency conversion stability, C/IM3, gain flatness, and phase noise [42].

SciEx provides coherent beacon transmitters at Ka (19.701 GHz, linear vertical) and Q (39.402 GHz, linear 45°), generated from a common reference and radiated by dedicated horns to map gaseous/rain attenuation, depolarization, and stability across Europe. While SciEx is primarily propagation-oriented, ComEx captures the communications-payload aspects of a Q/V feeder link with transparent frequency conversion, narrow-band channel filters, automatic-level-control (ALC), and switchable coverage, providing a rare in-orbit reference for Q/V transponder behavior under operational conditions. Figure 1.4 shows the block diagram of the ComEx payload.

SciEx results are presented in reviews and journal articles that report multi-site European statistics for gaseous/rain attenuation, depolarization, and scintillation, alongside long-term availability curves under ACM and gateway diversity [43, 44, 45]. The published datasets confirm strong seasonal variability, the necessity of multi-gateway architectures for 99.9–99.99% availability targets, and the feasibility of adaptive operation under fast-fading rain events using ACM and ULPC. These findings align with the

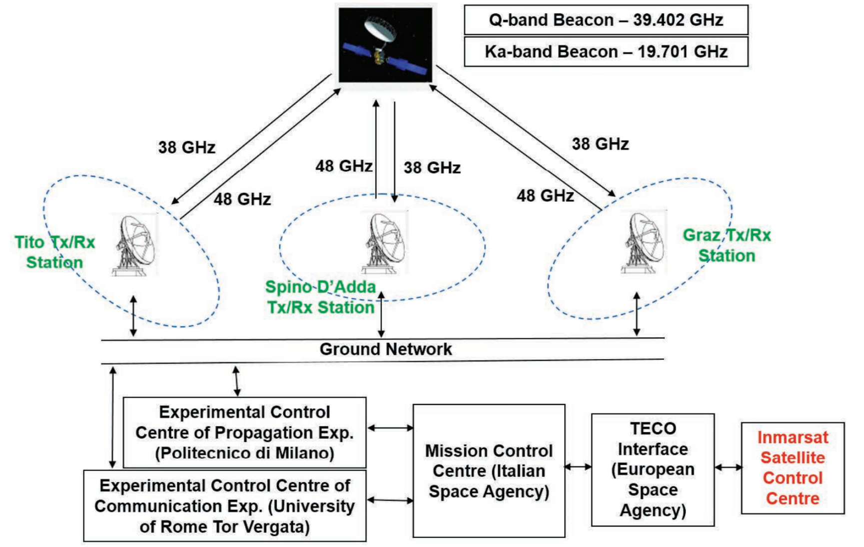

Figure 1.3: Aldo Paraboni (TDP5) mission/system scenario (space segment + Italian/Austrian ground and mission segment; loop/cross configurations), [43].

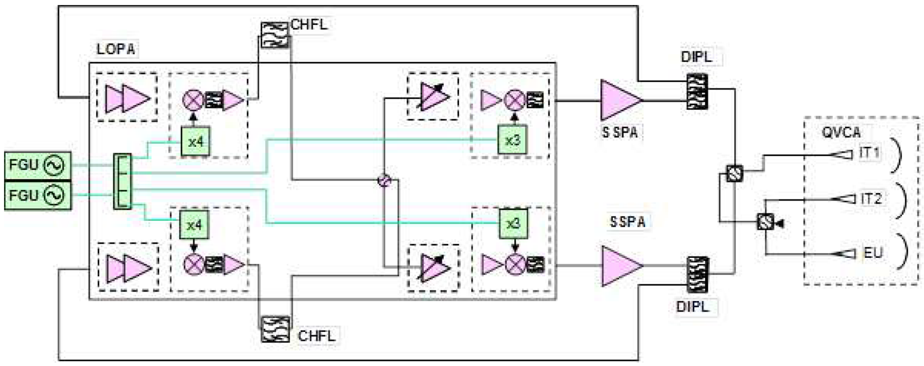

Figure 1.4: Aldo Paraboni ComEx payload block diagram (two transparent single-channel Q/V transponders; V-band Rx to Q-band Tx chains; switchable spot associations), [42].

P.618 exceedance models but add empirical detail on fade slopes, polarization cross-coupling, and short-term dynamics needed by modem designers [19, 14].

ComEx enabled end-to-end evaluation of on-board linearized SSPAs/TWTAs, mux/demux chains, and DVB-S2/S2X ACM operation. Reported results include ACM ladder tracking under induced attenuation with measured throughput vs. time-percentage curves: in practice, they induce controlled fades with a calibrated attenuator and record how the DVB-S2/S2X ACM ladder steps down/up in real time; from the resulting throughput time series they derive throughput-versus-time-percentage (availability) curves, which quantify the data rate sustained for 99-99.99% of the time and verify that the Q/V feeder link meets its service targets under fading. Other results include ULPC step response and stability and inter-gateway switching latencies. These experiments provided the reference operating envelopes later reused by ground segment designers of Q/V-capable HTS systems [43, 33, 21].

Inspired by the Aldo Paraboni results, two representative developments illustrate post-mission progress at the hardware level. On the receive side, a space-qualified miniaturized V-band front end down-converts a 43.1745 GHz uplink to a 5.0995 GHz IF using a 38.075 GHz LO and a hermetic WR-22–to–microstrip E-plane probe transition with cavity-mode suppression; the unit achieves $\sim$4.5 dB noise figure and > 50 dB gain over temperature, and passed full environmental qualification in a $208\times100\times125$ mm, 1.2 kg package [46]. On the transmit side, "Beyond Alphasat" documents the step from the TDP5 GaAs SSPAs (5–10 W at Q-band) to modern GaN MMIC architectures that target 50–100 W across 37.5–42.5 GHz with $\sim$25–30% PAE in similar outlines, enabled by higher power density, efficient corporate combiners, and improved thermal materials; reliability projections exceed 15 years for space service [47]. Together, these results indicate that receiver packaging/LO purity and linear chain stability have matured at V-band, while GaN power and combining techniques make Q-band downlinks reaching tens of watts practical in solid-state form.

2. Q/V band satellite front-end: philosophy and rationale

This chapter bridges the state-of-the-art review and the practical front-end (FE) design developed in Chapters 3 and 4. It first states the project objective and the design philosophy, highlighting the role of commercial off-the-shelf (COTS) components and their use in space. It then compares possible high-frequency transceiver topologies and motivates the chosen system architecture for Q/V band implementation.

2.1 Project objective and philosophy

The objective is to develop a Q/V band front-end covering the satellite feeder-link ranges used in practice: Q-band downlink around 37.5 - 42.5 GHz and V-band uplink around 47.2 - 52.4 GHz [48, 49]. The same FE shall operate in two modes: as a bent-pipe (transparent) transponder and as a front-end for a regenerative digital transceiver targeting 5G/6G non-terrestrial networks (NTNs). Regenerative payloads are widely regarded as a key step for future NTN capabilities (e.g., on-board gNB and inter-satellite processing), whereas the literature survey conducted for Chapter 1 did not identify publicly documented Q/V-band regenerative transceivers suitable for small satellites. This gap motivates the development of a research-grade prototype to explore feasibility, performance, and systems-level trade-offs; these topics are addressed in this work.

The project philosophy is to design a cost-contained, miniaturizable FE suitable for small-sat constellations using COTS components rather than custom devices. The process does not start from rigid requirements and a custom IC development path. Instead, it selects the best available devices, builds the most coherent architecture, and then measures and analyses the performance to map feasible application scenarios (see Chapter 5). This bottom-up, device-first approach reduces cost and time-to-prototype, and it lowers the barrier to the technology for both academia and new-space industry.

The use of COTS for space electronics is now very common under qualified processes, like the one called *Careful COTS* in [50]. Experience and test campaigns show that many modern parts tolerate the typical doses of LEO missions, provided that radiation effects are understood and mitigated, and that screening and lot control are enforced [50, 51, 52]. Key practices usually adopted include:

- **Radiation assessment and test:** mission dose modeling; radiation testing at board level where appropriate; attention to single-event effects (SEL/SEU/SEFI) and total ionising dose (TID) [50].
- **Design derating and protection:** operating voltages and currents derated per ECSS guidance oversizing absolute maximum voltages and currents of components; SEL current limiting via power converters; careful power-sequencing and watchdog/reset strategies [52, 51].
- **Process control and screening:** lot control and tracking; burn-in to retire infant mortality; conformal coating and tin-whisker mitigation when needed [50, 51].
- **Architectural resilience:** prefer highly integrated parts to reduce device diversity; disable non-essential blocks in idle operation to reduce SEE exposure [50].

This pragmatic approach supports rapid development while maintaining credible reliability targets for small-sat missions. In any case, implementation of these practices is outside the scope of the present prototype, in line with the exploratory research objectives of this study, and is deferred to future engineering iterations and flight-model developments.

2.2 Design topology and system architecture

High-frequency satellite transceivers are typically realised using one of three canonical architectures. The first is the classic superheterodyne, where the modem/SDR operates at an intermediate frequency (IF) and dedicated up and down conversion stages convert to and from RF. The main advantages are strong selectivity and image rejection thanks to IF filtering, straightforward gain distribution and calibration, and easy interoperability with legacy ground modems via IF interfaces. The main drawbacks are the extra conversions and local oscillators (LOs), which introduce and accumulate spurious responses such as LO feedthrough, images, intermodulation and conversion spurs.

A second option is direct conversion (homodyne), in which baseband I/Q streams are directly converted to the target RF using $f_{\mathrm{LO}} = f_{\mathrm{RF}}$ and accurate quadrature LOs. The main attractions are the single conversion step, a compact signal chain, and the absence of the classical IF image. The principal challenges are stringent LO generation at RF, DC offsets from self-mixing (LO leakage that mixes with the RF and collapses to DC), even-order distortion that also folds to DC and low frequencies, I/Q imbalance, and LO leakage [53, 54]. At Q/V bands (about 40–50 GHz), the production of precise, low-noise quadrature LOs directly at RF substantially increases LO-chain complexity and affects the associated power budget, making implementation and calibration demanding.

The third approach is direct RF sampling, where very-high-speed converters operate in higher Nyquist zones so that the RF is digitized or synthesized directly. This path is advancing rapidly; current Direct RF FPGA/SoC devices integrate converters up to about 64 Gsps with RF input bandwidths reaching 36 GHz [55, 56]. The key benefits are a simplified analogue front-end and strong digital flexibility, while the main limitations are the noise floor and SFDR at millimetre-wave frequencies, the need for careful analogue pre-/post-filtering and aliasing management. Also power consumption related to very high sampling rate are critical. Moreover, especially for Q/V applications, the present RF input bandwidth and sampling rates can not reach the full Q/V frequency span.

To sum up, given current device availability and the dual-mode objective (transparent FE and regenerative FE), a superheterodyne architecture is adopted. Direct-RF data converters do not yet span to Q and V band; state-of-the-art "Direct RF" devices offer RF input bandwidths around 36 GHz, leaving the portions around 40 GHz and around 50 GHz uncovered [55, 56]. A homodyne alternative would require setting LO = RF at roughly 40–50 GHz with accurate quadrature generation and tight phase-noise control, which significantly increases LO-chain complexity [53, 54]. In contrast, the superheterodyne approach simplifies the LO plan and image rejection through IF filtering, helping to keep phase noise, spurious responses, and linearity under control at millimetre-wave frequencies. It also aligns with both operating modes: for transparent operation, separate up and down converters can be interfaced through IF; for regenerative operation, the same IF ports connect to commercial modems or SDR, easing laboratory evaluation and integration with existing ground assets and industry compatibility with existing devices.

2.3 Intermediate Frequency

This section presents the analysis for the choice of the intermediate frequency (IF), which will then be used for the project. Since the FE requires to be used both as a bent-pipe transponder and as an up/down converter only, it was decided to choose a single intermediate frequency for both the receive and transmit chains.

The choice of the IF in a superheterodyne architecture is a critical design aspect that directly impacts both system performance and implementation complexity. Several factors must be considered in this selection. First, the IF value influences the level of local oscillator (LO) leakage: if the IF is chosen too close to zero, residual LO feedthrough may fall directly into the signal band, degrading sensitivity and dynamic range. Secondly, spurious responses and image products have to be carefully evaluated. In a downconversion chain, spurious signals appearing at the IF may overlap with the desired spectrum, while in an upconversion chain spurious products may fold into the RF band of interest, limiting the achievable spectral purity. Finally, there is a strong relation between the IF frequency and the required LO frequency. A lower IF implies that the LO must operate closer to the RF frequency, leading to higher absolute LO frequencies. This becomes particularly relevant in Q/V-band up/down converters, where an excessively high LO chain would demand phase locked loops (PLLs) and frequency multipliers with specifications that are increasingly difficult to meet in terms of phase noise, output power, and overall availability. For these reasons, the IF frequency is carefully chosen as a trade-off, balancing LO leakage, spurious-free dynamic range, and LO generation feasibility. There is also a requirement arising from the existing products which the front-end will have to interface to: in particular, the SDR developed by PICOSATS has an IF interface up to 7 GHz. The chosen intermediate frequency must therefore not exceed this limit.

An analysis based on spurious products of the frequency conversion has been conducted for both upconversion and downconversion, where

$$f_{spurs} = |m \cdot f_{IF} + n \cdot F_{LO}|$$

were plotted varying f_{IF} for upconversion and

$$f_{spurs} = |m \cdot f_{RF} + n \cdot F_{LO}|$$

were plotted varying $f_{IF} = f_{RF} - f_{LO}$ for downconversion.

Figure 2.1 shows downconversion spurious products with $m \in [-2, -1, 0, 1, 2]$ and $n \in [0, 1, 2, 4]$. The frequency band of interest is highlighted in light blue while the IF frequency is plotted in brown. The IF band of interest is highlighted in red. From the analysis it can be seen that no spurious products are interfering with the IF frequency (brown line) and no spurious products are overlapping the IF band of interest (red area) as the closest one is 3 GHz away even at $f_{IF} = 7$ GHz.

Figure 2.2 shows the same analysis in upconversion, with $m \in [-2, -1, 0, 1, 2]$ and $n \in [0, 1, 2, 4]$. The frequency band of interest is highlighted in light blue while the IF frequency is plotted in cyan. In this case, attention must be paid to spurious products that overlap the frequency band of interest. The analysis shows that over $f_{IF} = 5$ GHz no spurious is over the band of interest. In order to make the image easier to read, the analysis was repeated

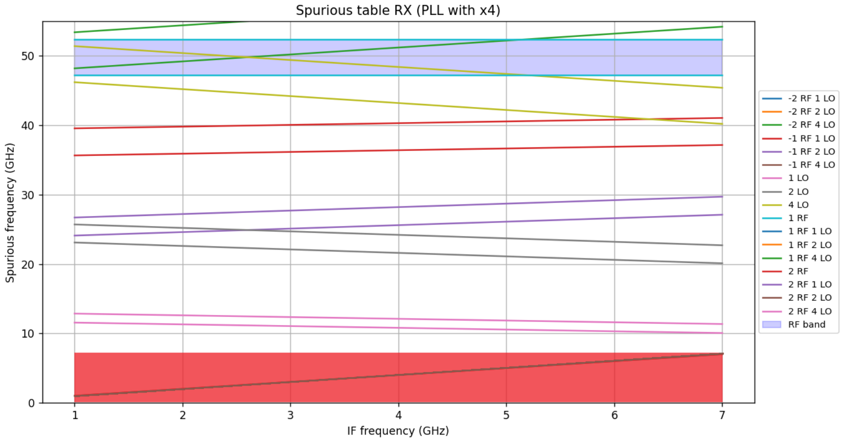

Figure 2.1: Spurious frequency and frequency band of interest vs intermediate frequency for the receiver chain.

with reduced order of the spurious products. Figure 2.3 shows the interference analysis of the spurious products with $m \in [-1, 0, 1]$ and $n \in [0, 4]$, leading to the same conclusions. Following these analysis and considerations, an intermediate frequency of 5.7 GHz was chosen as sufficiently lower than the maximum frequency of the SDR, 7 GHz, even to work with signal bandwidth greater than 1 GHz, and higher than 5 GHz where spurious interference occurs. Moreover, at 5.7 GHz several IF filters can be found (detailed in chapter 3).

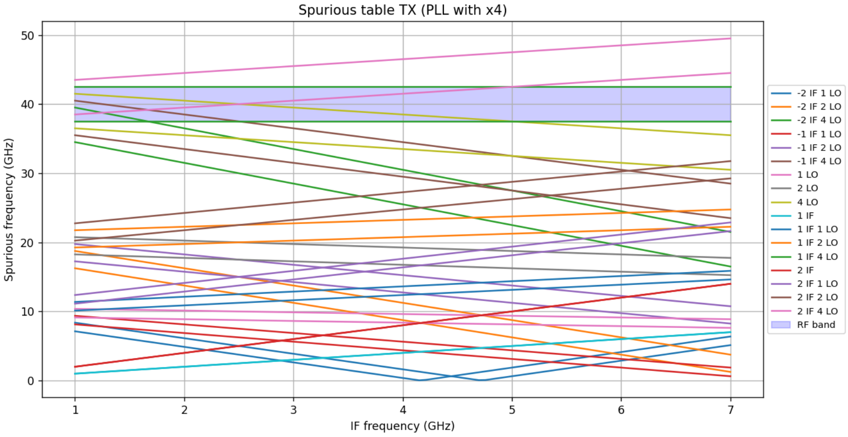

Figure 2.2: Spurious frequency and frequency band of interest vs intermediate frequency for the transmitter chain.

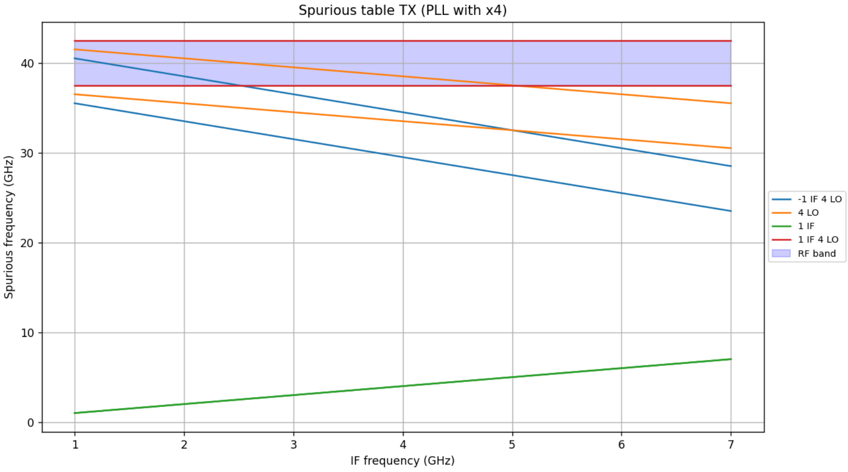

Figure 2.3: Spourious frequency and frequency band of interest vs intermediate frequency for the transmitter chain with reduced spurious order.

3. V-band Receiver design

As discussed in Section 2.2, the receiver will be a classic superheterodyne configuration with functional blocks starting from the antenna (not within the scope of this thesis), the receiver front end, the mixer, the local oscillator, and the intermediate frequency chain.

3.1 Receiver local oscillator chain

The receiver covers the 47.2–52.4 GHz band. With a selected IF of 5.7 GHz and a low-side injection scheme, the LO must tune from

$$f_{LO_{\min}} = f_{RF_{\min}} - f_{IF} = 47.2 - 5.7 = 41.5\,\text{GHz}$$

to

$$f_{LO_{\max}} = f_{RF_{\max}} - f_{IF} = 52.4 - 5.7 = 46.7\,\text{GHz}.$$

At V-band, monolithic, high-frequency voltage controlled oscillators (VCOs) inside integrated PLLs are still uncommon; many modern PLLs with integrated VCOs reach only about 10–13 GHz at their fundamental radio frequency (RF) outputs. An example of a V-band PLL including an on-chip VCO is reported in [34], but this is a custom complementary metal oxide semiconductor (CMOS) monolithic microwave integrated circuit (MMIC) prototype in die form, with relatively poor phase-noise performance and limited output power. This confirms the very low (almost null) availability of such devices as commercial off-the-shelf ICs in the market. Practical LO chains therefore rely on integrated PLL and VCO sources followed by active frequency multipliers to reach the target band while maintaining adequate drive for passive mixers that typically require more than 10 dBm at the LO port. A multiplication factor x4 is required to achieve the necessary frequency range for the LO chain. Another important factor to evaluate when choosing the local oscillator is the phase noise: in fact, the phase noise performance of the receive chain depends entirely on the phase noise of the local oscillator, which, when multiplied by a factor N, increases by $20\log(N)$[57].

Given the LO span and a practical ×4 multiplication strategy, the VCO needs to cover from 10.375 GHz to 11.675 GHz. Table 3.1 compares suitable synthesizers. The ADF4377 provides fundamental RF outputs up to

12.8 GHz meeting the needed band without engaging internal frequency multipliers. The ADF4371 (fundamental 4–8 GHz) requires its internal frequency multiplier/quadruplication path to exceed 8 GHz; also the TI's LMX2820 does not reach the required 11.675 GHz without its internal multiplier. Consequently, the ADF4377 is the best choice for the local oscillator.

Part Number	**VCO output frequency**	**Internal multiplier**	**Phase noise**
ADI ADF4377 [58]	6.4 GHz-12.8 GHz	No	−239 dBc/Hz
ADI ADF4371 [59]	4 GHz-8 GHz	Yes (×2, ×4)	−234 dBc/Hz
TI LMX2820 [60]	5.65 GHz-11.3 GHz	Yes (×2)	−236 dBc/Hz

Table 3.1: Integrated PLL and VCO options around 10–12 GHz.

Due to availability of components it is chosen to have two ×2 multiplication stages to reach the ×4 factor needed. Most common millimiter-wave mixers are passive, double-balanced devices that need more than 10 dBm to ensure adequate LO drive margin. For this reason only active multipliers are taken into consideration. The first multiplication stage is done by the HMC814LC3B, an SMT ×2 active multiplier able to deliver typically more than 15 dBm output power across 13 GHz - 24.6 GHz frequency range. Table 3.2 presents HMC573LC3B and HMC598 as alternatives but the first one does not cover the full range and the second one is only available in bare-die version, making them less attractive than the HMC814LC3B.

The baseline choice for the second multiplier is the HMC8342, an active ×2 multiplier specified for 22–42 GHz output with about 15 dBm typical output power. It is important to note that the upper portion of the required band (up to 46.7 GHz) lies beyond the HMC8342 limit. Table 3.3 analyses possible HMC8342 alternatives: there are connectorized/waveguide modules reaching up to 44 GHz that still do not cover the entire frequency range. The only option reaching 46 GHz is the HMC598 which is available only in bare-die.

Figure 3.1 shows the input-output characteristic (Figure 3.1a) and the output power as a function of the output frequency at different input powers (Figure 3.1b) of the HMC8342. From the latter, it can be seen that driving the multiplier in saturation still keeps the output power above 10 dBm even beyond 44 GHz.

In order to overdrive the final multiplier of the LO chain a gain block after the PLL was added. In this way also the HMC814LC3B was in saturation,

Part	**Input/Output Range**	**Typ. P_{out}**	**Form factor**
ADI HMC814LC3B [61]	in: 6.5–12.3 GHz out: 13–24.6 GHz	17 dBm	SMT
ADI HMC573LC3B [62]	in: 4–11 GHz out: 8–22 GHz	16 dBm	SMT
ADI HMC598 [63]	in: 11–23 GHz out: 22–46 GHz	13 dBm	Bare-die

Table 3.2: First ×2 multiplier candidates for the 21–23.35 GHz frequency range.

Part / Module	**Input/Output Range**	**Typ. P_{out}**	**Form factor**
ADI HMC8342 [64]	in: 11–21 GHz; out: 22–42 GHz	15 dBm	SMT
Eravant SFA-282SF-S1 [65]	in: 13.25–20 GHz; out: 26.5–40 GHz	20 dBm	Connectorized module
Eravant SFA-223443216-28SF-E1 [66]	in: 11–22 GHz; out: 22–44 GHz	16 dBm	Connectorized module
ADI HMC598 [63]	in: 11–23 GHz; out: 22–46 GHz	13 dBm	Bare-die

Table 3.3: Second ×2 multiplier candidates for 41.5–46.7 GHz.

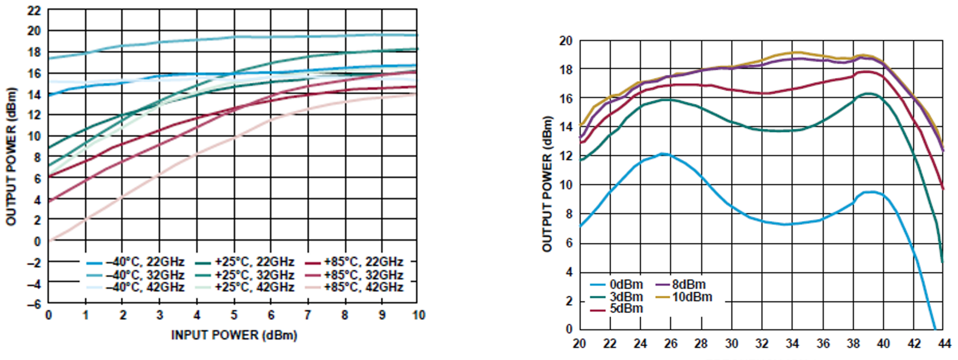

(a) Output power vs. input power at different temperatures and frequencies.

(b) Output power vs. output frequency at different input power.

Figure 3.1: From the datasheet of the HMC8342 x2 multiplier.

providing around 17 dBm at its output ensuring to overdrive the HMC8342. Figure 3.2 shows the block diagram of the final LO chain.

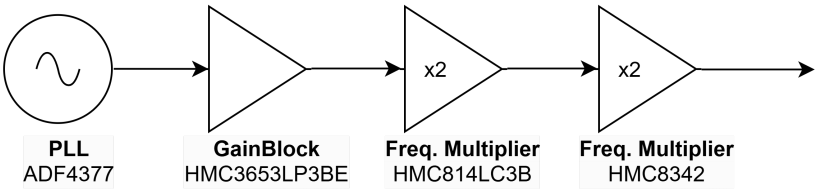

Figure 3.2: Block diagram of the Rx LO chain.

In Figure 3.3 a picture of the LO chain assembled in the receiver flat model is shown, where the main components (PLL, multipliers and bias circuit) are highlighted.

3.1.1 Breadboarding and measurements

In order to measure the receiver chain components the setup shown in Figure 3.4 was employed.

A signal generator was used to generate signals in the receiver RF frequency range and a spectrum analyzer was used to measure the IF frequency output. Although a waveguide measurement setup would have been more efficient, coaxial cables were chosen to carry the RF signal in order to facilitate assembly of the setup, improve its versatility and reduce its costs. For this reason, 1.85 mm connectors were used, which have an operating frequency of up to 67 GHz. The DUT was powered by several DC power supplies needed to generate all different the voltages needed by the EVBs.

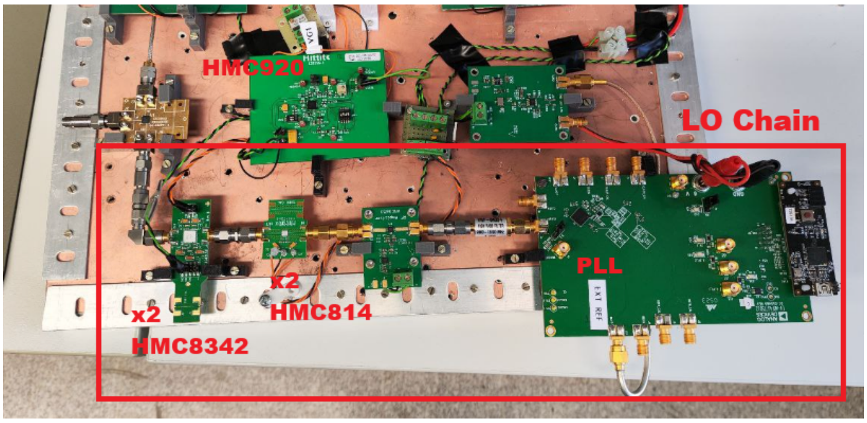

Figure 3.3: Picture of the LO chain assembled and tested in the receiver flat model.

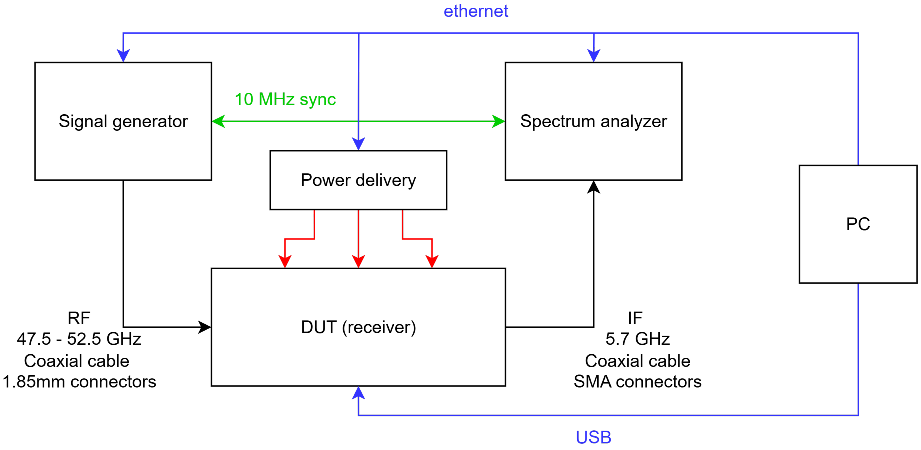

Figure 3.4: Receiver measurement setup block diagram.

The generator and the analyzer were synchronized using a 10 MHz reference and controlled using ethernet protocol as well as the power supplies. The DUT EVBs were controlled using an USB connection and the software provided by the manufacturer.

In Figure 3.5 a picture of the assembled measurements setup is shown.

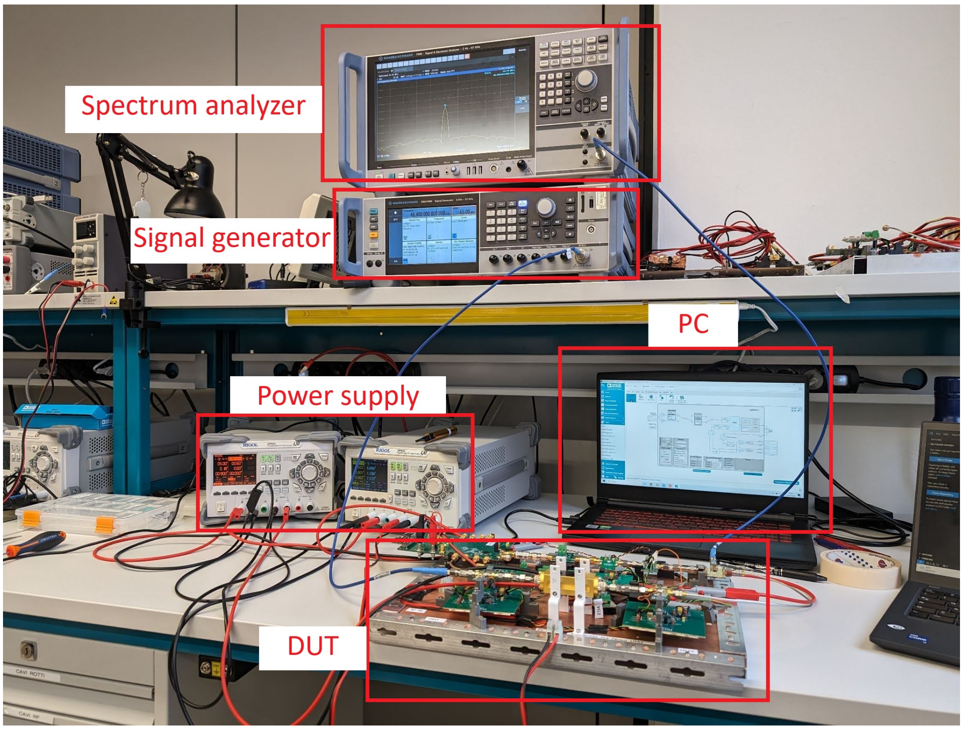

Figure 3.5: Picture of the receiver measurement setup.

The same setup was used to perform all the receiver measurements presented in this Chapter changing the DUT with the specific receiver chain portion.

While measuring the PLL chain, particular attention was paid to the polarization management of the HMC8342 Doubler. The HMC8342 is indeed implemented in GaAs technology, as are the majority of high-frequency amplifiers. Most integrated GaAs or GaN amplifiers are FET devices based on depletion-mode HEMT technology [67, 68]. These devices require a specific power-up procedure: in particular, the drain voltage V_D must never be applied before a negative voltage is applied to the gate. With $V_{GS} = 0\,\mathrm{V}$, the channel is already formed and allows strong conduction; applying the drain voltage before biasing the gate with a negative voltage would result in a large current flow and overheating of the device, eventually causing damage [68].

In addition, these devices tend to be unstable at low drain voltages V_D [69]. It is therefore recommended to first set the gate voltage below the threshold voltage ($V_{GS_{th}}$), so that the channel is completely pinched off, and then raise V_G to reach the desired bias point only after the drain voltage has been applied.

For this reason, an active bias controller is employed to automate the bias sequencing and ensure safe operation. In particular, the HMC920LP5E from Analog Devices is adopted [70]. It is a compact, 5 mm × 5 mm SMT IC that provides programmable gate bias control for GaAs and GaN FETs. The device continuously monitors the drain current and dynamically adjusts the gate voltage, guaranteeing repeatable bias conditions and preventing damage due to incorrect sequencing or thermal drift.

At first the Analog Devices HMC8342 was evaluated individually. The device requires two negative polarizations. Table 3.4 shows the voltages used during the measurement.

Vdd (V)	**Idd (mA)**	**Vgg1 (V)**	**Vgg2 (V)**
5	170	-1.25	-0.6 (controlled by HMC920)

Table 3.4: HMC8342 Polarization conditions.

In order to evaluate the frequency behavior of the HMC8342, critical for the mixer driving, its gain versus output frequency was measured in large signal gain conditions. These measurements are shown in Figure 3.6, where the drop at 42 GHz is well visible.

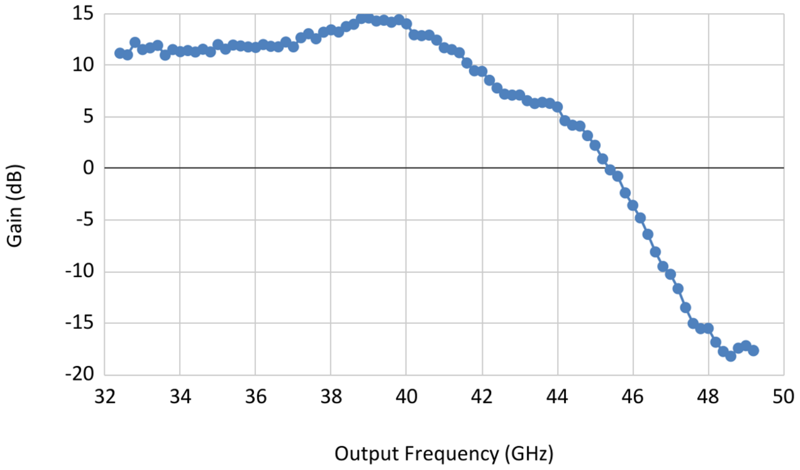

Figure 3.6: Gain and output power of the HMC8342 duplicator as a function of the output frequency (duplicated).

The performances of the first doubler were then evaluated. Figure 3.7 shows the power values as a function of the output frequency at the HMC814LC3B device. Across the entire frequency range of interest the output power value remains around 17 dBm. This performances allow to overdrive the HMC8342 and get an output power over 5 dBm even above 44 GHz. Attention must, however, be paid to the input power to the HMC8342 in order to remain within its absolute maximum ratings, which must not exceed 12 dBm.

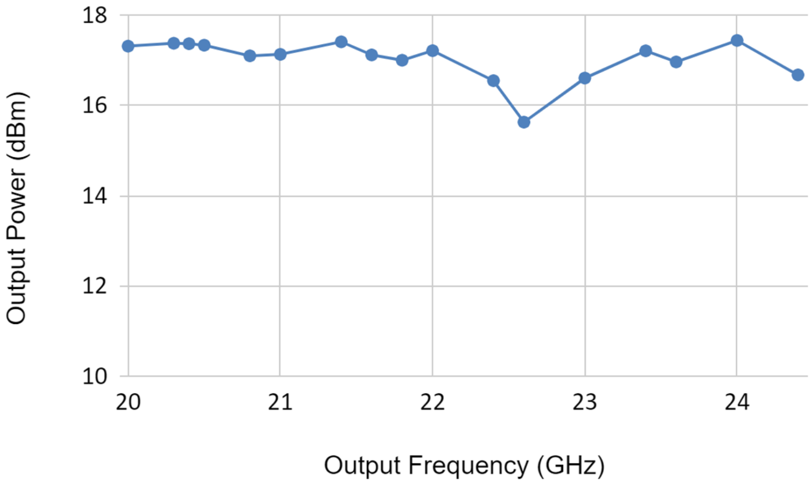

Figure 3.7: Power level as a function of the output frequency at the first LO chain duplicator (reference level *R1* in 3.2.

3.2 Front-end and mixer

Figure 3.8 shows the block diagram of the front-end with the mixer included. When designing satellite receivers having a low noise amplifier (LNA) as first block, even before the channel filter, it is crucial to reduce the noise figure of the system [71]. In addition a second LNA is added just after the filter to further reduce the cascade system noise figure.

In the 47.2 – 52.4 GHz window, the number of packaged, COTS LNA integrated circuit (IC)s is limited: many offers are either waveguide modules or bare-die MMICs. A notable exception is Analog Devices' ADL8106, a 5×5 mm LGA, 50 Ω-matched LNA specified up to 54 GHz [72]. Around 50 GHz it delivers 20.5 to 22 dB gain with 4 dB noise figure (NF) (typical) and integrates the signal AC-coupling and supply decoupling, which simplifies biasing and layout; these are key advantages over bare-die alternatives. For completeness, V-band bare-die options include ADI's ADL7003 (50–95 GHz) [73] and Qorvo's TGA4811 (DC-60 GHz)[74], both viable at 50 GHz but less attractive for this work due to assembly complexity and handling. Table 3.5 shows a comparison between the available V-band LNAs; it is easy to

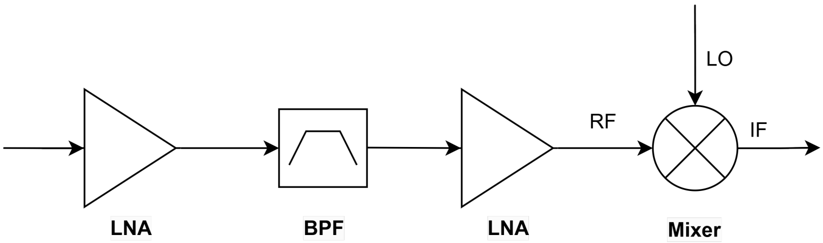

Figure 3.8: Block diagram of the front-end chain and mixer.

conclude that the ADL8106 is the only choice meeting all the requirements.

Part	**Freq. range**	**Gain (typ)**	**NF (typ)**	**Form factor**
ADI ADL8106	18–54 GHz	20–22 dB	4 dB	5×5 mm LGA
ADI ADL7003	50–95 GHz	14–15 dB	5 dB	Bare die
Qorvo TGA4811	DC–60 GHz	15 dB	3 dB	Bare die

Table 3.5: Comparison of available LNAs around the 47–52 GHz band.

At V-band, few mixers are available as packaged ICs: most solutions are still connectorized or bare-die. The Analog Devices ADMV1550 offers a practical alternative: a 4×4 mm SMT double-balanced mixer covering 15–65 GHz with IF frequency up to 20 GHz. Around 50 GHz it shows a conversion loss of around 8 dB and IIP3 of approximately 20 dBm, combining wideband performance with compact packaging. Thanks to its internal baluns and 50 Ω interfaces, it can be directly integrated on PCB without external matching, making it the most suitable choice for the 47–52 GHz downconverter front-end [75]. For completeness, broadband options such as the Marki Microwave MM1-1453LSM-2 (14–53 GHz) were also considered. Although the latter overlaps with the band of interest, its parameters are slightly worse than the ADMV1550, which makes it less attractive for this design [76]. Table 3.6 shows a comparison of the available V-band mixers.

In designing the downconverter front-end, the channel filter plays a key role in defining the RF passband while rejecting unwanted signals (harmonics, out-of-band interference, LO feed-through [77, 71]). Considering an im-

Part	**RF/LO Range**	**IF Range**	**Conv. Loss (typ)**	**Linearity (typ)**	**Form factor**
ADI ADMV-1550	15–65 GHz	DC–20 GHz	8 dB	IIP3 20 dBm, IP2 40 dBm, P1dB 11 dBm	4×4 mm SMT LGA
Marki MM1-1453LSM-2	14–53 GHz	DC–20 GHz	9–10 dB	IIP3 18 dBm	3×3 mm QFN

Table 3.6: Comparison of mixer options for the 47–52 GHz downconverter front-end.

age attenuation of 60 dB and an intermediate frequency value of 5 GHz or higher, the parameters shown in Table 3.7 were obtained following [78, 79].

Parameter	**Typical values**
f_0 (GHz)	49.3
1 dB bandwidth (GHz)	4.26
60 dB band (GHz)	15.8
60 dB/1 dB form factor	3.7
Fractional bandwidth	0.086

Table 3.7: Image filter design specifications.

Available filter options fall into three main categories: waveguide bandpass filters, connectorized or coaxial filters, and custom MMC/microstrip filters. Waveguide filters typically offer excellent insertion loss, high power handling, and good out-of-band rejection, but they are bulky and require waveguide transitions / flanges. Connectorized filters are more compact but often introduce higher loss or less ideal rejection near band edges. At this stage, no suitable commercial component has been identified.

The commercial component available that most closely matches the specifications is the Eravant SWF-52310350-15-B1 waveguide bandpass. It offers a passband from 47-57 GHz, low insertion loss (around 2.5 dB), high rejection

(40 dB) outside the band, and compatible rectangular waveguide designation (WR)-15 waveguide ports [80]. Table 3.8 shows a comparison between market available V-band filters where only waveguide filters were identified.

Part	**Passband (GHz)**	**Insertion Loss (typ)**	**Interface**	**Manufacturer**
SWF-52310350-15-B1	47–57	2.5 dB	WR-15	Eravant
VDI WR15BPF 50.1–57.7 [81]	50.1–57.7	<1 dB	WR-15	Virginia Diodes
VDI WR19BPFE 45.5–52.6 [82]	45.5–52.6	<1 dB	WR-19	Virginia Diodes

Table 3.8: Comparison of available channel filter options around 47–52 GHz.

Once the main building blocks of the receiver front-end were selected, the overall performance in terms of noise figure and gain was estimated through a theoretical cascade analysis. In particular, the equivalent noise figure F_{eq} was computed using the well-known Friis formula for cascaded stages:

$$F_{\mathrm{eq}} = F_1 + \frac{F_2 - 1}{G_1} + \frac{F_3 - 1}{G_1 G_2} + \dots \tag{3.2.1}$$

where F_i and G_i denote the noise factor and the linear gain of the i-th stage, respectively. The total gain of the chain is simply given by the product of the individual stage gains expressed in dB.

Table 3.9 summarizes the devices adopted in the front-end together with their main parameters and the resulting cascade values. Based on this analysis, the front-end achieves an overall noise figure of approximately 4.08 dB and an equivalent gain of about 29 dB.

Parameter	**LNA1**	**BPF**	**LNA2**	**M1**	**Cascade**
Name	ADL 8106	waveguide (WG) filter	ADL 8106	ADMV 1550	
NF [dB]	4	4	4	8	4.08
Gain [dB]	20.5	-4	20.5	-8	29

Table 3.9: Cascade chain specifications.

3.2.1 Breadboarding and measurements

Figure 3.9 shows the block diagram of the assembled flat model for the V-band FE. As previously discussed for the HMC8342, also the ADL8106 is

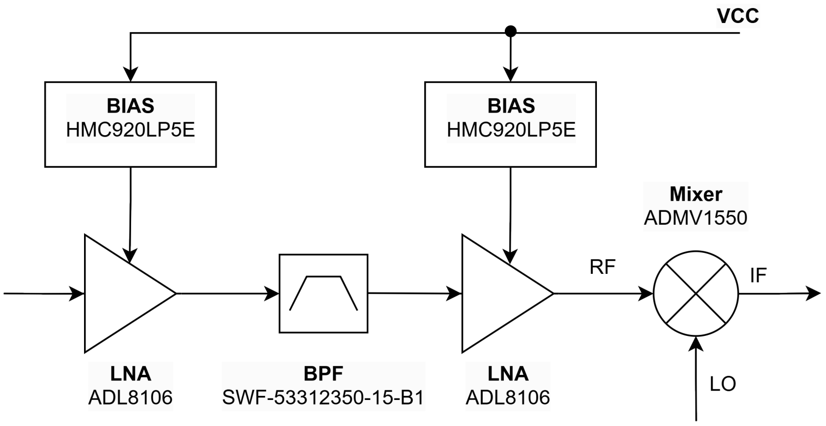

Figure 3.9: Block diagram of the flat model front-end chain and mixer.

a depletion-mode GaAs HEMT device and therefore it requires a controlled bias sequencing, where the gate voltage must be applied before the drain voltage to avoid excessive current flow and possible device damage. For this reason, the same active bias control solution (HMC920LP5E) is adopted, ensuring safe start-up and stable operation of the LNA.

Figure 3.10 reports a picture of the the assembled flat model of the V-band FE showing the two LNAs with their biasing circuit and the waveguide channel filter.

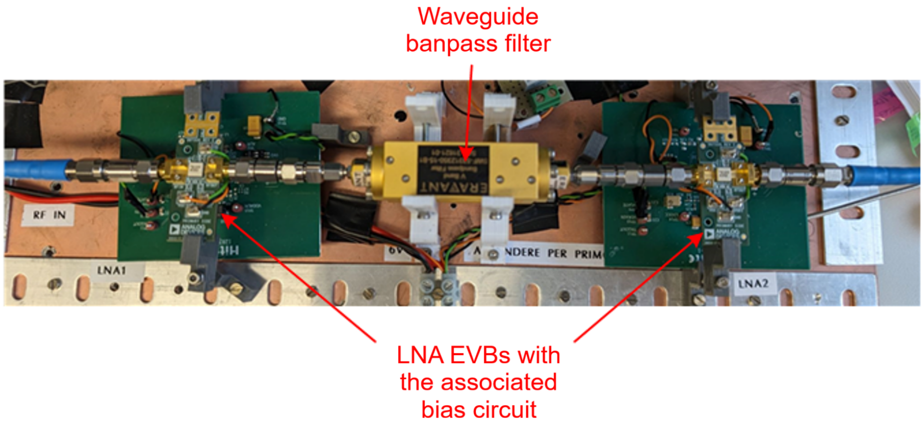

Figure 3.10: Complete front end with LNA1, waveguide image bandpass filter, and LNA2.

Measurements of output power varying the input power have been performed allowing to plot the input output characteristics of the FE and check its gain. Figure 3.11 shows gain and output power versus input power. The measurements were taken at 42.5 GHz.

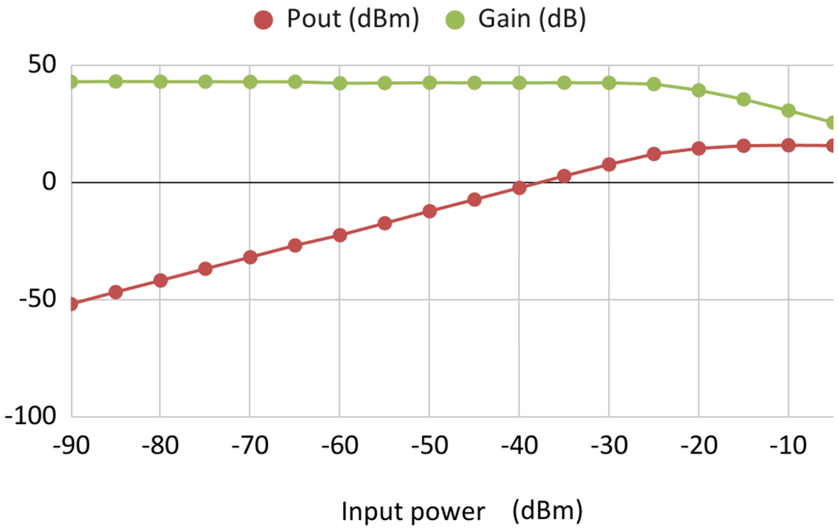

Figure 3.11: RX front-end output gain and power as a function of input power to the chain. Signal generator frequency $f = 47.2$ GHz.

These measurements were also repeated varying the frequency in order to understand frequency behavior of the system. Figure 3.12 shows gain measurements versus frequency: Figure 3.12a with input power of -40 dBm and 3.12b with input power of -70 dBm.

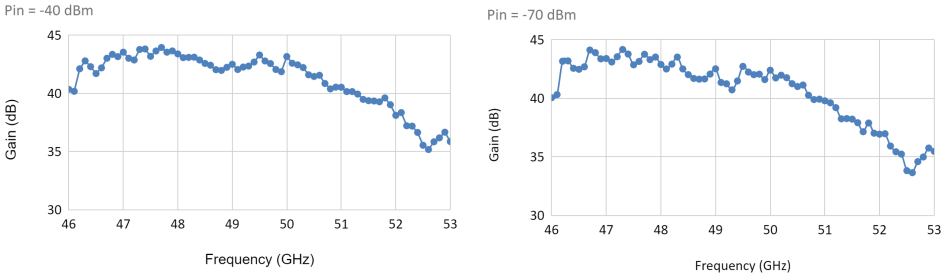

(a) (b)

Figure 3.12: Output gain at the front end of the Rx chain as a function of input frequency. Signal generator power $P = -70$ dBm on the left and $P = -40$ dBm on the right. Cable contributions compensated.

After measuring the RF part of the front-end, the mixer and the LO chain (described in Section 3.1) were added to the flat model demonstrator and measurements with frequency downconversion were performed. Table 3.10

shows the biasing specifications of the chain: LNAs and PLL shared the same supply voltage of 6 V draining 1.18 A while the LO chain frequency duplicator had its own supply of 5 V sourcing 0.17 A resulting in a total of 7.9 W power consumption.

Receiver (RF, LO)		**HMC8342 duplicator**			
Vdd (V)	**Idd (A)**	**Vdd (V)**	**Idd (A)**	**Vgg1 (V)**	**Vgg2 (V)**
6	1.18	5	0.17	-1.25	-0.6

Table 3.10: Receiver and duplicator supply specifications.

System gain measurements as a function of RF frequency and input power are shown in Figure 3.13. The system shows a gain of 25/30 dB for RF frequencies below 50.7 GHz while, for RF frequencies above 50.7 GHz, there is a progressive deterioration in performance due to poor mixer driving by the LO chain (detailed in 3.1).

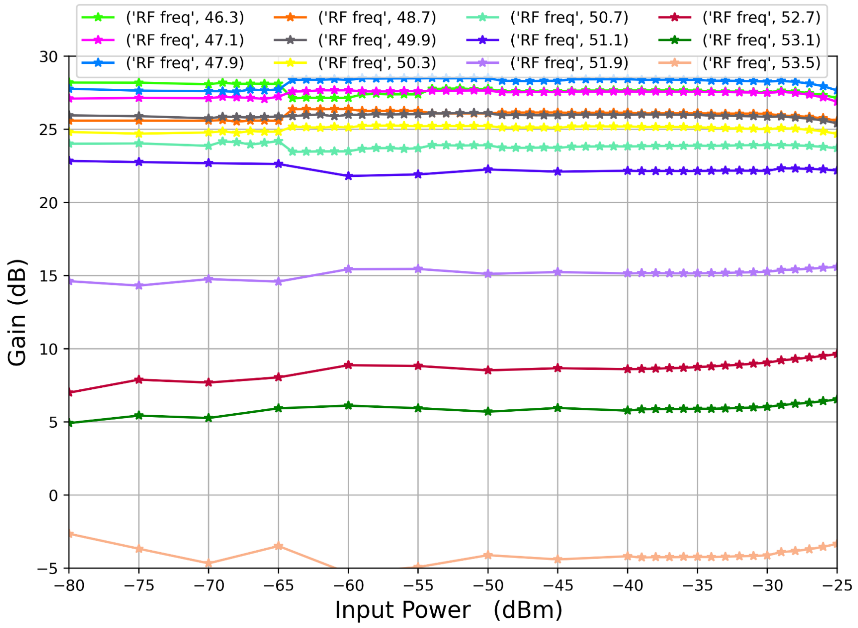

Figure 3.13: Output gain at the mixer of the Rx chain as a function of input power, for different RF input frequencies. Output power levels acquired at the IF frequency of 5.7 GHz.

In order to evaluate the driving performances of the LO chain, its power has been measured varying the LO frequency and comparing it with the LO power needed by the mixer (13 dBm, [75]). The results are shown in Figure 3.14 where a maximum loss of 5 dB is reported at 46.0 GHz.

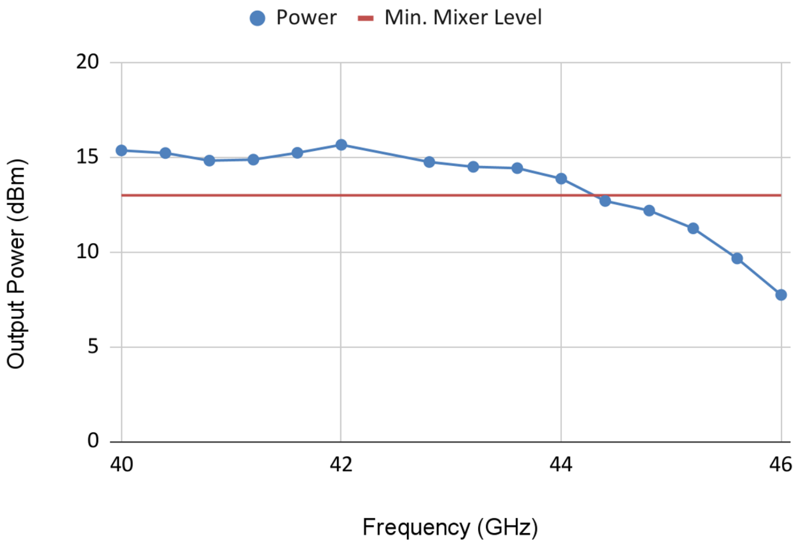

Figure 3.14: Power level at the output of the LO chain as a function of the generated signal frequency (reference level *R2* in 3.2). The red line outlines the minimum power level for driving the mixer.

The LO leakage study was initially conducted with a visual analysis of the full span spectrum. Figure 3.15 shows the acquired spectrum, in which the LO/2, 3/4LO, and 3/2LO harmonics are visible in addition to the 41.2 GHz LO signal. Harmonics were then acquired with the RF signal applied and measuring each harmonic power value in dBc with respect to the IF converted signal. Figure 3.16 shows the power values of harmonics and LO signal varying its frequency. Starting from 44 GHz, the mixer is driven with a power gradually lower than the optimal one, which is why the power of the harmonics reaches the power of the IF signal. These signals will, however, be filtered out by the IF chain.

3.3 Receiver IF frequency circuit

The IF gain budget is driven by the ADC input requirement. Let us define the maximum admissible gain as

$$G_{\max}\,[\mathrm{dB}] = FS\,[\mathrm{dBm}] - MDS\,[\mathrm{dBm}]\,, \tag{3.3.1}$$

where FS is the ADC full-scale (in dBm) and MDS is the minimum detectable signal at the RF input (in dBm).

The minimum detectable signal is set by the receiver noise floor and by the minimum signal-to-noise ratio required by the selected waveform:

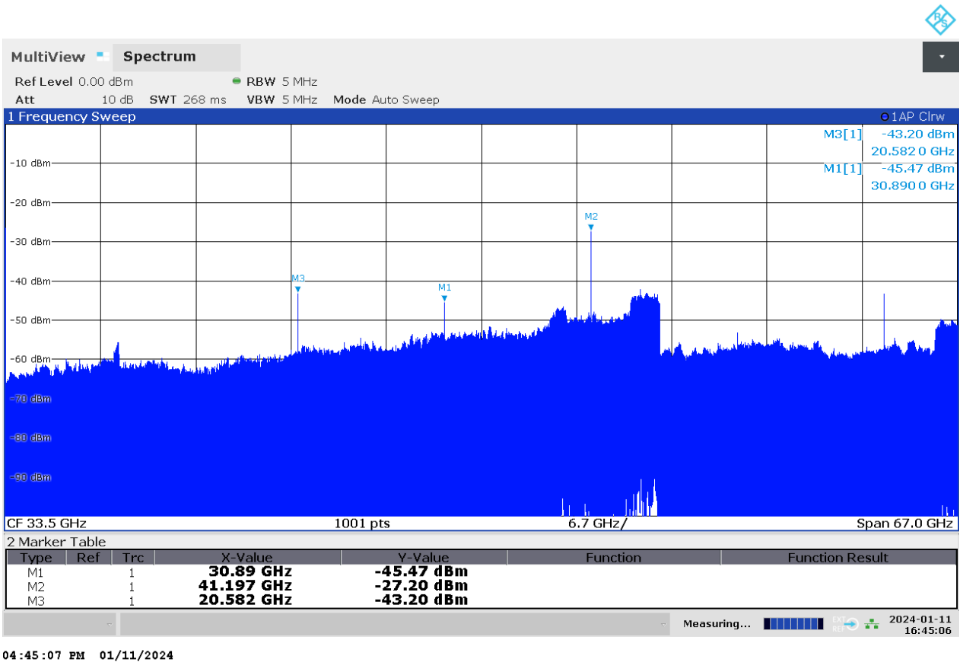

Ref Level 0.00 dBm
Att 10 dB SWT 268 ms
RBW 5 MHz
VBW 5 MHz Mode Auto Sweep

M3[1] -43.20 dBm 20.582 0 GHz
M1[1] -45.47 dBm 30.890 0 GHz

CF 33.5 GHz 1001 pts 6.7 GHz/ Span 67.0 GHz

2 Marker Table

Type	Ref	Trc	X-Value	Y-Value	Function	Function Result
M1		1	30.89 GHz	-45.47 dBm		
M2		1	41.197 GHz	-27.20 dBm		
M3		1	20.582 GHz	-43.20 dBm		

2024-01-11 16:45:06

04:45:07 PM 01/11/2024

Figure 3.15: Spectrum Analyzer capture of LO harmonics at the mixer output. Visible harmonics LO/2, 3/4LO, and 3/2LO.

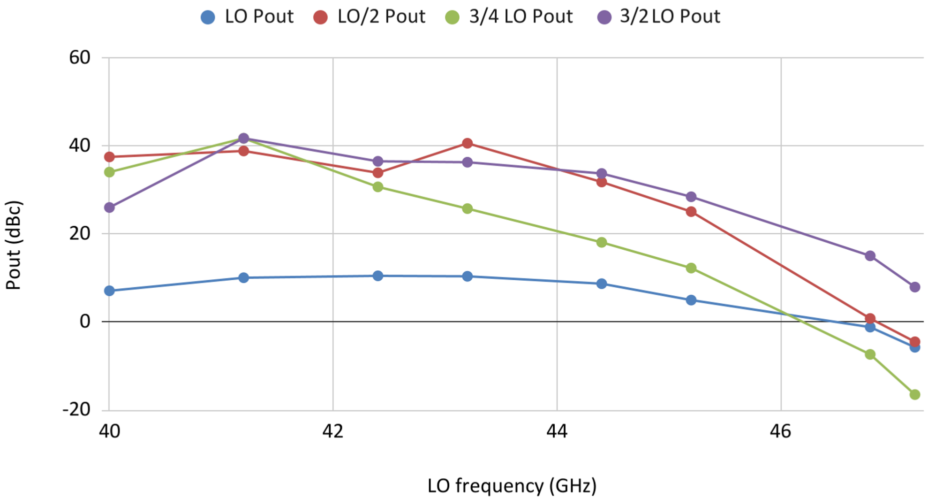

Figure 3.16: Output power of the LO signal and its harmonics as a function of the LO frequency. Power levels are shown in dBc relative to the IF signal power.

$$MDS\,[\text{dBm}] = N_{\text{floor}}\,[\text{dBm}] + SNR_{\min}\,[\text{dB}] \tag{3.3.2}$$

$$N_{\text{floor}}\,[\text{dBm}] = N_0\,[\text{dBm}] + 10\log_{10}(B) + NF\,[\text{dB}]$$

Here $N_0 \simeq -174$ dBm/Hz is the thermal noise density at 290 K, B is the IF noise bandwidth, and NF is the receiver noise figure.

State-of-the-art direct-RF transceivers (e.g., the AD9081 MxFE) provide multi-GS/s ADCs suitable for instantaneous bandwidths at IF, which motivates the choice $B = 1\,\text{GHz}$, [83]. With the receiver noise figure obtained in the RF design section, $NF = 4.08$ dB, the integrated noise power at the receiver input is

$$\begin{aligned} N_{\text{floor}} &= -174 \text{ dBm/Hz} + 10\log_{10}(1 \times 10^9) + 4.08 \text{ dB} \\ &= (-174 + 90 + 4.08)\text{dBm} \\ &= -79.92 \text{ dBm} \approx -79.9 \text{ dBm}. \end{aligned} \tag{3.3.3}$$

For robust operation and to maximize $G_{\max}$ in (3.3.1), the analysis considers the most conservative Digital Video Broadcasting Satellite Second Generation (DVB-S2) modulation and coding (MODCOD). DVB-S2 is widely adopted for high-rate point-to-point satellite links, including satcom feeder links where other protocols can be encapsulated in a DVB stream [22, 23]. Using QPSK with code rate 1/4, the demodulator minimum signal to noise ratio (SNR) in AWGN channel scenario, $\text{SNR}_{\min}$, can be inserted from the standard performance tables that report a value of ≈ -2.4 dB [22].

With the noise floor from (3.3.3) and inserting in (3.3.2) the minimum detectable signal becomes

$$\begin{aligned} MDS &= -79.9 \text{ dBm} - 2.4 \text{ dB} \\ &= -82.3 \text{ dBm} \end{aligned}$$

The full scale value of the AD9081 was taken as the maximum output level. From the datasheet [83] we get $FS = 1.475$ V_{pp} that, calculated in decibels over a differential impedance of $100\,\Omega$, is equal to 4.37 dBm. Therefore:

$$G_{\max}\,[\text{dB}] = 4.37\,\text{dBm} - (-82.3\,\text{dBm}) = 86.7\,\text{dB}$$

.

Considering the linearity conditions of the ADI converter [83], which suggest an input signal 10 dB lower than the full scale value, FS, the maximum gain considered is 76.7 dB. Knowing from the receiver front-end section that the gain up to the mixer stage is 29 dB, the gain of the subsequent IF stages will be:

$$G_{\mathrm{IF}}\,[\mathrm{dB}] = (76.7 - 29.0)\,\mathrm{dB} = 47.7\,\mathrm{dB}$$

rounded up to 48 dB, which is the value to be used for an initial evaluation of the overall receiver system.

The active devices adopted are three stages of the QPA9127 wideband gain block amplifiers. Each device provides a typical gain of about 20 dB in the IF band [84], with good linearity and output power margin (that will be evaluated in the complete receiver section). The use of three stages guarantees sufficient overall gain to meet the 48 dB requirement. The gain blocks are placed at different points in the chain, separated by filters and an attenuator, in order to improve stability and suppress unwanted spurious responses [85, 86].

To introduce flexibility in the overall chain gain, a digital step attenuator, the HMC1119 from ADI, is inserted between the first and second gain stages. This device can be programmed to adjust the gain over a wide dynamic range with fine resolution. The attenuator serves several functions: it allows trimming of the nominal gain to precisely meet the link budget specifications controlling the output power in case of varying input conditions and, in conjunction with an RSSI (Received Signal Strength Indicator) provided by the modem or software defined radio (SDR), enables the implementation of an automatic level control (ALC) loop, stabilizing the signal level delivered to the ADC.

In the demonstrator, the IF filtering stage was implemented with a wideband ceramic band-pass filter (Anatech AM5700B1128), providing a bandwidth of approximately 500 MHz around 5.7 GHz [87]. This choice allows the same hardware to accommodate both operating scenarios: the transparent transponder case, where the system acts as a bent-pipe payload, and the transceiver case, where the IF chain is connected to a modem or SDR. The wider bandwidth ensures compatibility with various modulation schemes and allows evaluation of different link configurations without redesigning the hardware.

In Figure 3.17 the block diagram of the designed IF chain is shown.

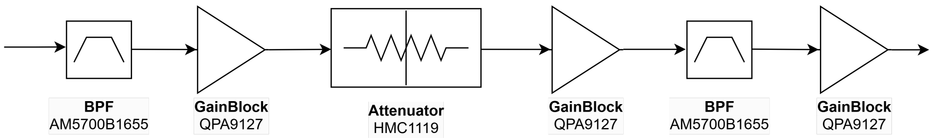

Figure 3.17: Block diagram of the IF Rx chain.

For a final prototype specifically optimized for the transparent bent-pipe transponder solution, narrower filters can be considered. A tighter channel filter would improve out-of-band rejection and potentially reduce the overall system noise figure, at the cost of flexibility, allowing also weaker link budget scenario to close successfully. Conversely, for an implementation involving a modem or SDR, a simple low-pass filter could be adopted, leaving the IF channel selection and shaping to the modem's DSP and demodulation algorithms. This approach simplifies the analog design and leverages the strong digital filtering capabilities of modern SDR platforms.

3.3.1 Breadboarding and measurements

First, the performance of the gain block was analyzed, as the chosen IF frequency is near the upper limit of its operation bandwidth. The gain of the amplifier as a function of the operation frequency was then measured. The measurements are shown in Figures 3.18 where a loss of less than 2 dB can be seen at 6.2 GHz compared with the gain at 6.0 GHz.

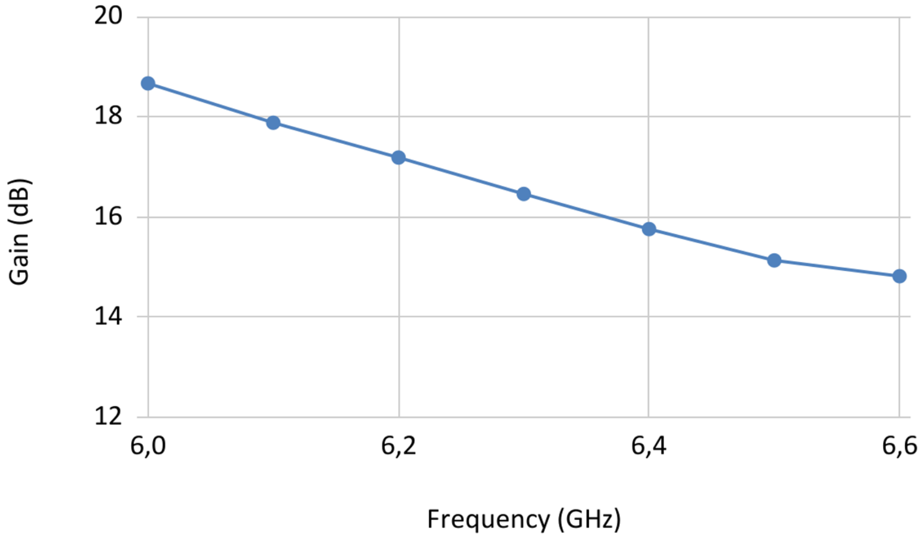

Figure 3.18: Gain vs frequency of the QPA9127 at frequencies higher than 6.0 GHz.

Also S-parameters were evaluated with a dual port VNA, showing that a degradation of the S_{11} is present bringing its value from less than -15 dB up to around -10 dB. Measurements are shown in Figure 3.19 where S_{11} and S_{22} are reported in the Smith chart (left) and plotted against frequency (right).

The loss of gain and the worsening of S_{11} do not affect the use of the gain block for the IF chain. For a final prototype, a gain block operating at higher frequencies may lead to slight improvements over the results reported in this study.

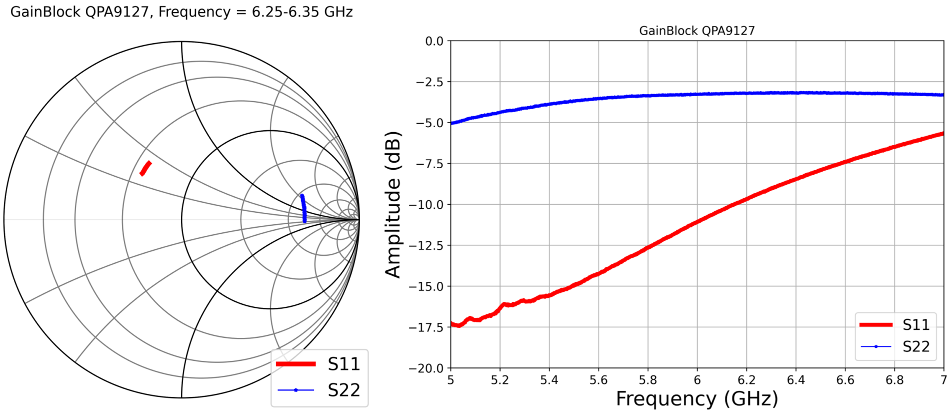

Figure 3.19: S parameters as a function of frequency.

The filter used for the IF chain is the Anatech AM5700B1655 [87], a 500 MHz band pass ceramic filter with center frequency at 5.7 GHz. The filter is supplied with an integrated filter-PCB solution and no evaluation board (EVB) is available, so a custom PCB was designed to interface with the filter through coaxial connectors. A picture of the final PCB with the filter mounted is shown in Figure 3.20. S-parameters of the filters were then measured to verify the PCB interface and are reported in Figure 3.21 showing losses around 2 dB and S_{11} under -5 dB.

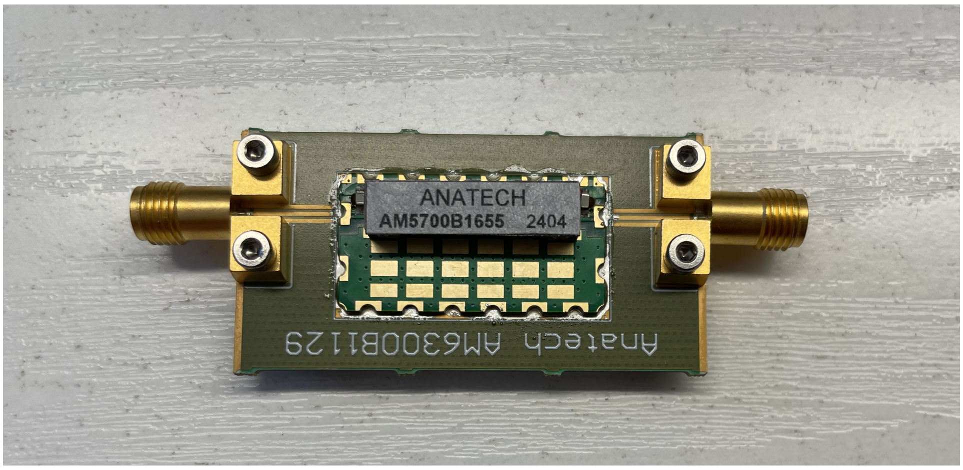

Figure 3.20: Photo of one of the two Anatech filters.

Finally, gain of the entire IF chain was evaluated versus frequency with particular attention on the out-of-band portion of the spectrum. Figure 3.22 compares output power measurements in two different conditions: with and without the input filter. The plot shows considerably better out-of-band

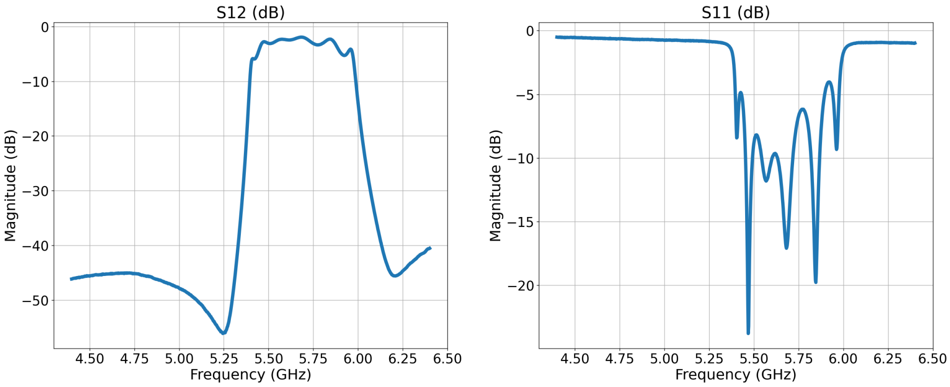

Figure 3.21: S-parameters as a function of the frequency of the Anatech AM5700B1655 filter used in the chain.

performances in the two filter chain case.

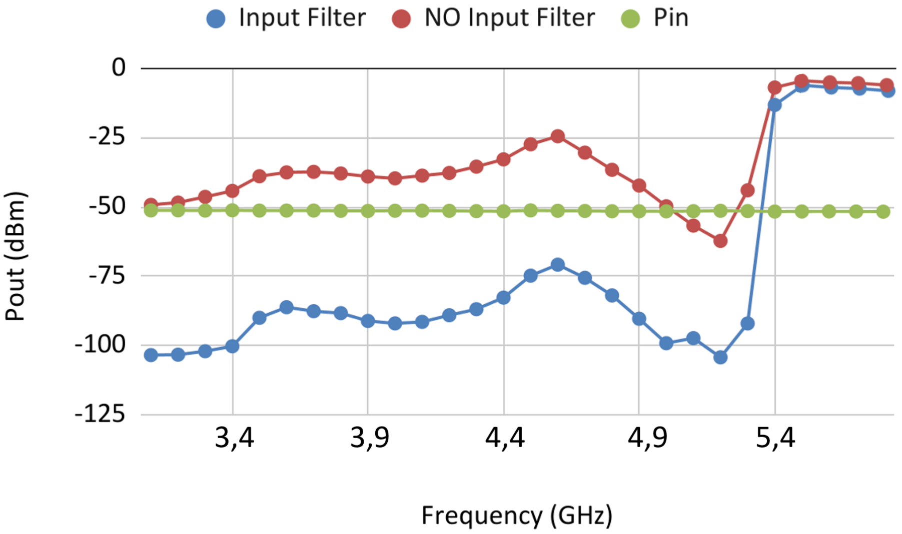

Figure 3.22: Output power of the IF Rx chain as a function of frequency. Comparison of solutions with and without the first filter in the chain.

3.4 Complete receiver

In Figure 3.23 the complete block diagram of the entire receiver chain is shown.

Before assembling all the sub-blocks of the chain shown in the previous chapters, the linearity performance of the receiver was evaluated, verifying

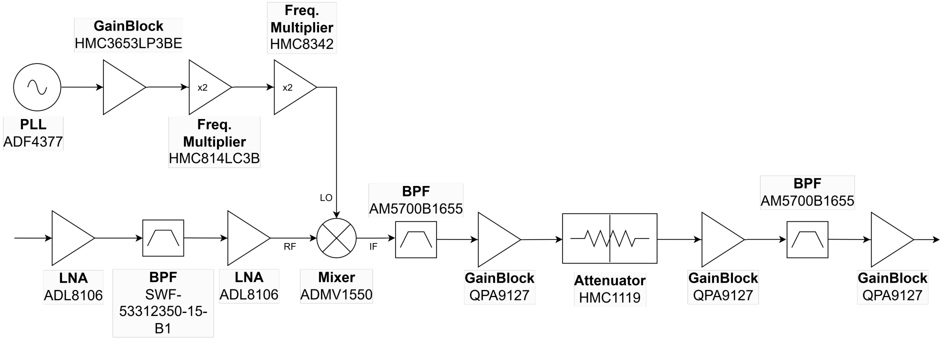

Figure 3.23: Block diagram of the entire V-band receiver demonstrator.

that each component worked in the linear zone, sufficiently far from its saturation point. To do this, in Figure 3.24 output saturation point is shown in red and output power is shown in blue for each stage of the chain. The input power to the chain used for the analysis is -85 dBm, approximately equal to the MDS calculated in the previous section. The attenuation of the variable attenuator was set to the minimum, -2.3 dB, in order to consider the maximum gain condition. For the passive stages no output compression power is reported.

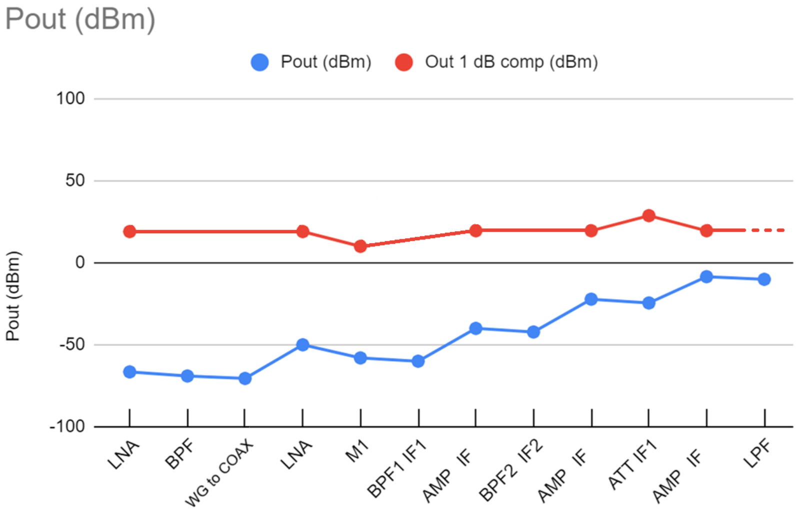

Figure 3.24: Output power and 1 dB compression point of the individual stages. Pin = -85 dBm and attenuator set to minimum attenuation IL = 2.3 dB.

It can be seen that even in the maximum gain condition the output of the chain is more than 20 dB lower from the saturation point at the output in each stage. By design, in the maximum gain condition the limit of the ADC input is reached with the MDS calculated considering 1 GHz bandwidth. This allows to receive even stronger signals due to the dynamics of the attenuator and also allows to receive weaker signals at narrower bandwidth due to the dynamic range and resolution of the ADC. This also ensures that each component of the chain is operating in a high linearity region decades below their saturation point. For this reason no specific linearity measurements were conducted on the complete receiver demonstrator.

3.4.1 Breadboarding and measurements

Complete receiver measurements are shown in this section. A picture of the assembled demonstrator is shown in Figure 3.25. The gain, measured with a digital attenuator level of 0, is shown in Figure 3.26. Measurements of gain over input power at different input frequencies were performed. The IF value was fixed at 5.7 GHz. Under correct mixer drive conditions, the system gains around 70 dB. As already explained before, due to losses in the LO chain when operating at high frequency, the gain decreases at the upper limit of the frequency range reaching around 55 dB at 52.0 GHz. In the measurements, an output power step is visible around -65 dBm of input power. This is due to the used instrumentation, which changes its internal attenuation: the step is also visible when directly measuring generator output power.

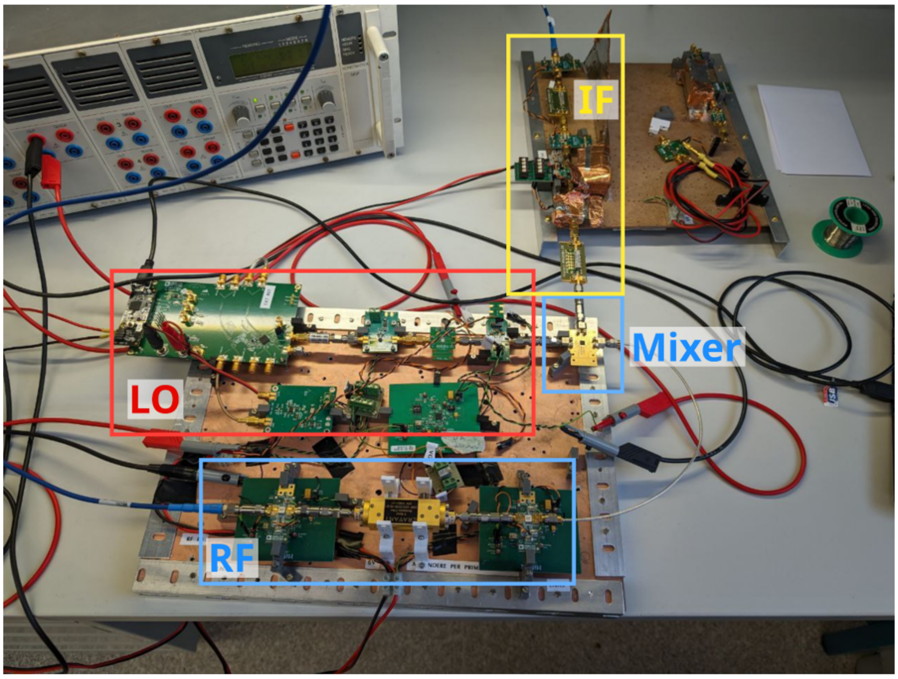

Figure 3.25: Receiver flat model demonstrator picture.

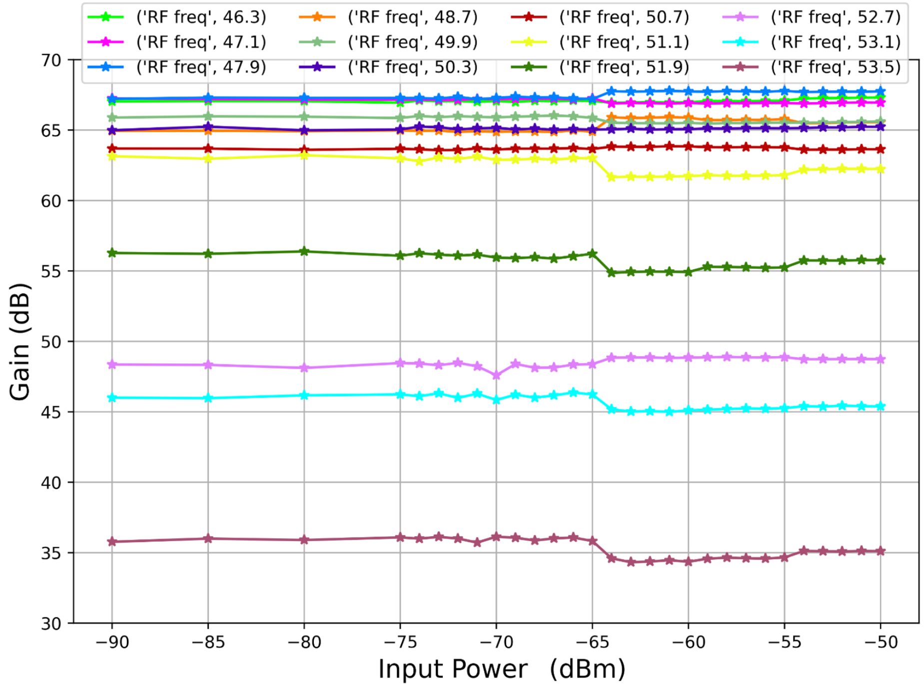

Figure 3.26: Output gain at the IF block of the Rx chain against input power, for different RF input frequencies. Output power levels acquired at an IF frequency of 6.3 GHz. Cable contributions compensated.

The noise floor was evaluated for the entire receiver and shown in Figure 3.27, where the power was normalized with respect to the frequency. Even in this case the measurements are in line with the expected values: at room temperature, the measure value of -100 dBm/Hz perfectly aligns with a system with a gain around 70 dB and a noise figure around 4 dB.

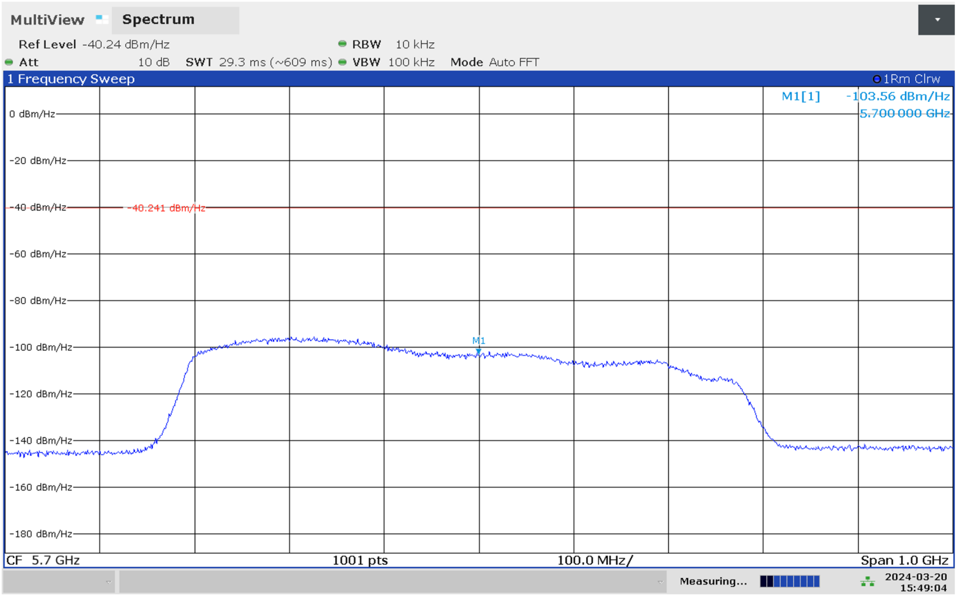

Ref Level -40.24 dBm/Hz
Att 10 dB
SWT 29.3 ms (~609 ms)
RBW 10 kHz
VBW 100 kHz
Mode Auto FFT
M1[1] -103.56 dBm/Hz
5.700 000 GHz
CF 5.7 GHz
1001 pts
100.0 MHz/
Span 1.0 GHz

Figure 3.27: Noise floor in the receiver band with the y-axis in dBm/Hz.

To conclude, the receiver evaluation phase noise measurements were performed considering the frequency offset from 100 Hz to 10 MHz. Figure 3.28 shows the phase noise of the system at different Phase Frequency Detector frequencies. All curves present the same phase noise in the VCO region, but they have slightly higher plateau and lower cutoff frequency as the phase frequency detector (PFD) frequency decreases. Additionally, lower PFD frequency curves show a resonance at the cutoff frequency that can compromise modulated signal reception. PFD frequencies of 100 MHz or 200 MHz will be used.

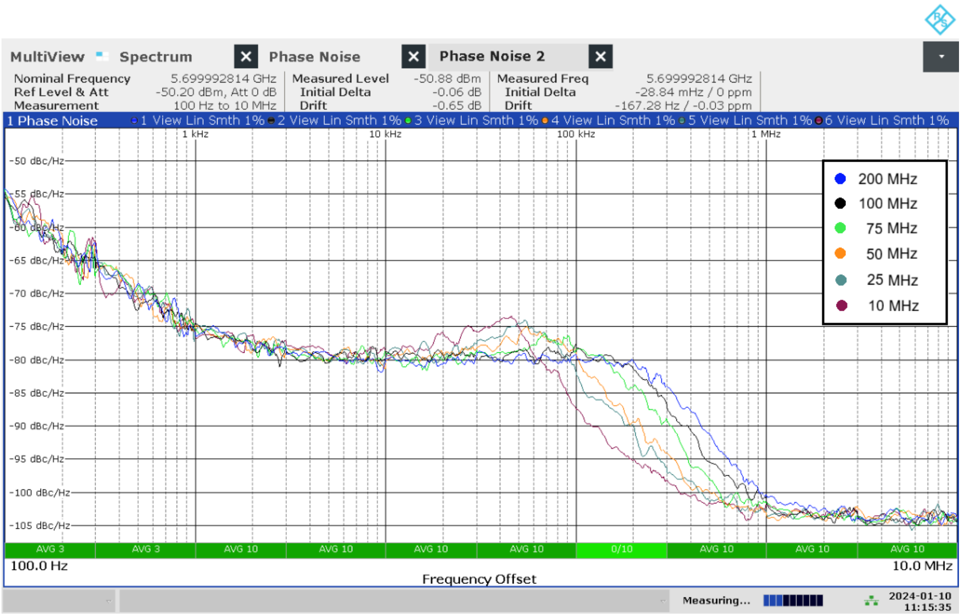

Nominal Frequency 5.699992814 GHz
Ref Level & Att -50.20 dBm, Att 0 dB
Measurement 100 Hz to 10 MHz

Measured Level -50.88 dBm
Initial Delta -0.06 dB
Drift -0.65 dB

Measured Freq 5.699992814 GHz
Initial Delta -28.84 mHz / 0 ppm
Drift -167.28 Hz / -0.03 ppm

11:15:36 01/10/2024

Figure 3.28: Phase noise at the receiver output for different PFD frequency values.

4. Q-band Transmitter Design

This chapter presents the design, implementation, and measured performance of the Q-band transmitter front-end operating in the 37.5–42.5 GHz frequency range, with an IF centered at 5.7 GHz. The architecture follows a superheterodyne upconverter employing a passive, double-balanced mixer. Section 4.1 develops the LO plan and synthesizer chain; section 4.3 addresses the IF chain; section 4.2 details the RF upconverter and filtering and section 4.4 consolidates cascade analysis and measurements.

4.1 Local Oscillator Chain

The required LO frequency is set by the desired RF band and the chosen IF. For a upper-sideband (USB) upconversion the frequency range spans from:

$$f_{LO_{\min}} = f_{RF_{\min}} - f_{IF} = 37.5 - 5.7 = 31.8\,\text{GHz}$$

to

$$f_{LO_{\max}} = f_{RF_{\max}} - f_{IF} = 42.5 - 5.7 = 36.8\,\text{GHz}.$$

As discussed in the receiver chapter, integrated VCOs and PLLs rarely exceed the 10–13 GHz fundamental range and usually reach an output power around 0 dBm. Active multiplying stages are therefore required to reach Q-band while preserving adequate LO drive for a passive mixer. Two main architectural options were evaluated for the transmitter LO chain.

The first option is to minimize the multiplication factor by adopting a single active tripler. In this scenario, a VCO operating in the range of 10.6–12.3 GHz could directly feed a ×3 multiplier, producing the required LO span of 31.8–36.8 GHz. Such a solution is attractive because it reduces the number of frequency conversion stages, which limits the cumulative increase of phase noise. Moreover, using a single multiplier simplifies the LO chain, reduces PCB area, and minimizes the filtering overhead. On the other hand, this approach presents significant limitations.

From a theoretical standpoint, frequency triplers are intrinsically less efficient and more challenging to design than doublers or quadruplers. The third harmonic component generated by a nonlinear device is typically much weaker than the even-order ones, as most semiconductor transfer characteristics are dominated by quadratic nonlinearities. Efficient tripling thus requires both the suppression of the stronger fundamental and second-harmonic components and the enhancement of the weaker cubic term, which demands complex impedance terminations and harmonic filtering networks at multiple frequencies [88]. These factors make the implementation of high-efficiency triplers particularly difficult, especially at millimeter-wave frequencies where matching networks become increasingly sensitive to parasitic effects [89].

Indeed, packaged, surface-mount active triplers capable of delivering sufficient output power in the 31.8–36.8 GHz range are not available. The few commercially available solutions are often bare-die devices or connectorized modules, both of which complicate integration into a compact transmitter front-end. In addition, the available output power margin may not be sufficient to drive a passive mixer directly, and filtering of residual fundamentals and unwanted harmonics becomes critical. A comparison of representative active tripler devices is given in Table 4.1.

Part / Vendor	**Type**	**Freq. (in/out)**	**Form factor**
Mini-Circuits CY3-453-D+, [90]	Passive ×3	in: 6.66–15 GHz; out: 20–45 GHz	Bare-die
Eravant Uni-Guide ×3 (28–32 GHz),[91]	Active ×3	in: 9.3-10.7 GHz; out: 28–32 GHz	Connectorized waveguide module (WR-28)
BQ Microwave / AT Microwave, [92]	Active/Passive (family)	up to 110 GHz (family)	Connectorized

Table 4.1: Representative ×3 frequency multipliers around the 32–37 GHz region. No suitable COTS SMT option meeting span and LO drive was found.

The second option is to reuse the same hardware developed for the receiver chain, based on two cascaded active doublers. In this case, a PLL+VCO operating in the range 7.95-9.2 GHz is followed by a first ×2 multiplier, which generates 15.9-18.4 GHz, and then by a second ×2 multiplier, which delivers the final 31.8-36.8 GHz. While this chain results in a higher multiplication factor overall, and therefore higher phase noise compared to the tripler approach, it has several practical advantages. Firstly, it allows reuse of the same bill of materials and PCB design blocks as the receiver, thereby reducing design risk, development time, and procurement effort. Secondly, robust and reliable packaged SMT components are readily available for both multiplier stages, and these devices are capable of delivering sufficient LO power (above +10 dBm) to drive a passive double-balanced mixer without additional amplification. The use of two doublers also facilitates better suppression of unwanted harmonics between stages, as filters between the two stages can be used to improve spectral purity. For these reasons, despite the theoretical benefits of a simpler tripler-based approach, the ×2 + ×2 architecture was ultimately preferred for the transmitter prototype.

In conclusion, the solution chosen for the LO chain is very similar to the one shown in Figure 3.2 for the receiver, with the only difference being that, by operating in the center of the frequency band of the HMC8342, the second multiplier, it is no longer necessary to operate at full saturation to overcome the problem of performance drop at the frequency band limit. For this reason, the gain block before the first multiplier, the HMC365LP3BE, is not included in the transmitter LO chain.

In this configuration, considering that the output power of the PLL is around -3 dBm [58], the first multiplier, the HMC814LC3B, can deliver around 10 dBm as output power as can be seen in Figure 4.1.

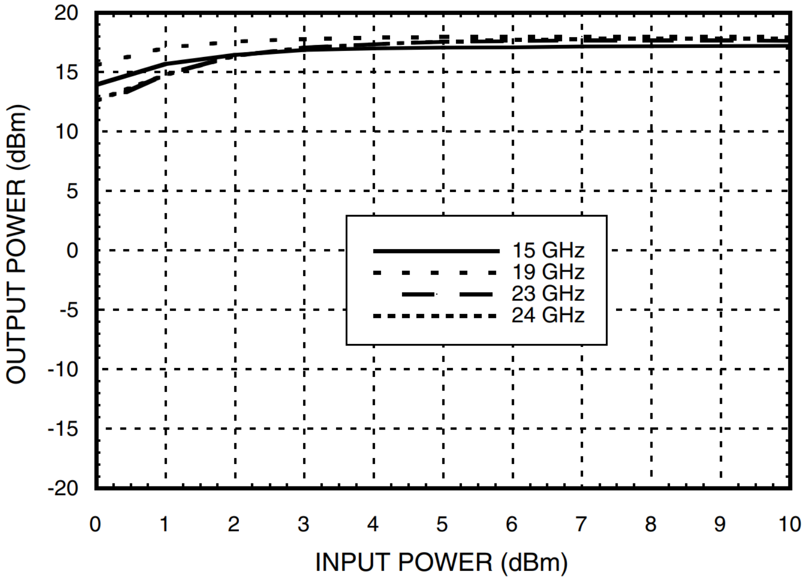

Figure 4.1: Input output power characteristics of the first multiplier of the LO chain, HMC814LC3B [61].

With the above specified power, the second multiplier can be driven up to deliver 15 dBm output power, as shown in Figure 3.1, which is typically enough for the LO chain of a passive double balanced mixer.

4.2 Mixer and transmitter RF Front-End

Recent advances in GaN-on-SiC technologies have enabled solid-state power amplifiers (SSPAs) to operate efficiently well into the Q-band (37–43 GHz), achieving output power levels that only a few years ago required vacuum devices [93]. In the open literature, GaN MMIC PAs around 37–43 GHz routinely exhibit multi-watt saturated output power, double-digit gain, and power-added efficiency (PAE) approaching 30%. For example, a 40 GHz GaN-on-Si MMIC presented in [94] demonstrated 12 W saturated output power with 30% power added efficiency (PAE). Similarly, a 39 GHz front-end MMIC reported in [95] achieved over 20 dB small-signal gain and 30 dBm output power, including the validation for emerging 5G multicarrier signals. A comprehensive review of millimetre-wave GaN power amplifier (PA) design techniques, including load modulation and balanced architectures, is given in [96], highlighting that Q-band transmitters can now reach the 4-10 W output class with 16-20 dB gain and mid-teens efficiency in compact MMIC form factors.

Similar performances are available also in the market from the main GaN RF components producers such as QORVO and MACOM. Table 4.2 compares representative COTS options around the 37.5–42.5 GHz band. Among these, Qorvo's QPA4346D was adopted due to its output power (it reaches more than 6 W of output power), integration effort (50 Ω match, dc blocking on I/O), and evaluation-board availability at the time of procurement.[1] Room-temperature operation enables approximately 40 dBm at saturation, decreasing to about 38 dBm near 85 °C.

To deliver the power levels just specified, the QPA4346D needs input power from 27 dBm to 30 dBm depending on frequency of operation and temperature, therefore a medium/high-power driver capable of delivering at least 30 dBm across 37.5–42.5 GHz is necessary. Table 4.3 surveys suitable COTS drivers.

The ADPA7008AEHZ offers a packaged, 50 Ω-matched solution with $P_{\mathrm{1dB}} = 30\,\mathrm{dBm}$ and $P_{\mathrm{SAT}} = 31\,\mathrm{dBm}$ up to 40 GHz, with typical required input drive in the 12–16 dBm range depending on frequency and temperature. Figure 4.2 shows output power, gain, PAE and drain current versus input power of the ADPA7008AEHZ. This device was therefore selected for the driver role, also due to its availability from the major distributors.

To reach the 12–16 dBm input level required by the driver, a pre-driver stage is included. The ADPA7009-2 provides from 17.5 to 19.5 dB small-signal gain, depending on the bias conditions, and 1 dB compression point above 28 dBm [103] as visible in Figure 4.3, that shows output power, gain, PAE and drain current versus input power of the ADPA7008AEHZ. These

---

[1] Characterization data used to size the line-up were provided under NDA; numerical graphs are not reproduced here.

Part / Vendor	**Freq. (GHz)**	P_{SAT} **(dBm)**	**Gain (dB)**	**Form factor / Notes**
QPA4246D (Qorvo), [97]	37.5–42.5	40 (10 W)	16	GaN/SiC MMIC, Bare die
QPA4346D (Qorvo), [98]	37.5–42.5	37.8 (6 W)	16	GaN/SiC MMIC, Bare die
QPA4446D (Qorvo), [99]	37.5–42.5	36 (4 W)	18	GaN/SiC MMIC, Bare die.
MAAP-011423-DIE (MACOM), [100]	37–43	39–40 (7.5–10 W)	20	GaN/SiC MMIC, Bare die
CHA8454-99F (UMS), [101]	37.5–43.5	40 (10 W)	24	GaN/SiC MMIC, Bare die

Table 4.2: Representative Q-band SSPA options around 37.5–42.5 GHz (vendor typical data).

Part / Vendor	**Freq. (GHz)**	P_{SAT} **(dBm)**	**Form factor / Notes**
ADPA7008AEHZ (ADI), [102]	22–40	31	SMT, 7×7 mm LCC_HS
ADPA7009-2 (ADI) [103]	20–54	28.5 (20–35 GHz)	SMT, 5×5 mm LGA
QPA2040D (Qorvo), [104]	20–40	33.5	GaN/SiC Bare die
MAAP-011379, [105]	20–55	30	SMT, 5x7 mm 12-Lead
MAAM-011291-DIE, [106]	20–45	30	GaAs pHEMT, Bare die

Table 4.3: Driver/medium-power amplifier candidates for the 30 dBm class output at Q-band.

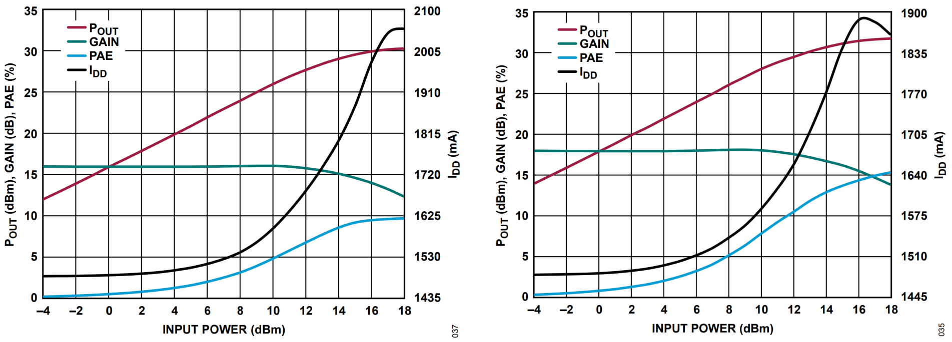

(a) P_{OUT}, Gain, PAE and I_{DD} vs. Frequency at 30 GHz of frequency of operation.

(b) P_{OUT}, Gain, PAE and I_{DD} vs. Frequency at 36 GHz of frequency of operation.

Figure 4.2: From the datasheet of the ADPA7008AEHZ Q-band driver amplifier, [?]

features ensure the achievement of 16 dBm output power while operating in linear domain with input powers below 0 dBm.

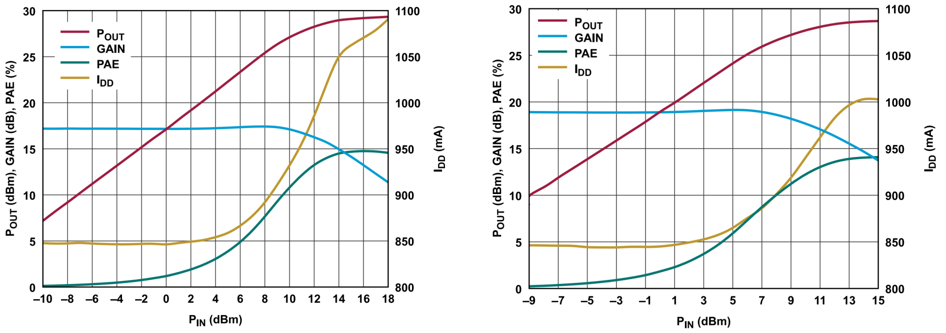

(a) P_{OUT}, Gain, PAE and I_{DD} vs. Frequency at 30 GHz of frequency of operation.

(b) P_{OUT}, Gain, PAE and I_{DD} vs. Frequency at 36 GHz of frequency of operation.

Figure 4.3: From the datasheet of the ADPA7009-2 Q-band driver amplifier [103].

The transmitter output requires selective filtering to suppress mixer spurious products, LO feedthrough, and out-of-band harmonics before the antenna interface. At Q-band, mainly two classes of components were found as COTS in the market: compact SMT ceramic filters, and high-performance waveguide band-pass filters. Table 4.4 shows a comparison of the COTS Q-band filter found.

Knowles offers multilayer SMT filters such as the B385MD0S and B424MB1S, covering portions of the Q-band. These components provide convenient PCB

Part / Vendor	Passband (GHz)	IL (dB)	Interface / Notes
SWF-40305340-22-B1 (Eravant), [107]	37–42	2.0	WR-22 waveguide
SWF-40320340-22-B1 (Eravant), [108]	30–50	1.5	WR-22 waveguide
B385MD0S (Knowles), [109]	30-40	2.5	SMT
B424MB1S (Knowles), [110]	40.5-43.5	2.7	SMT
PE-W28F002 (Pasternack), [111]	38-40	1.5	WR-28 waveguide

Table 4.4: Comparison of candidate channel filters at Q-band.

integration and good insertion loss performance; however, each device spans only a limited bandwidth (typically a few gigahertz) and does not fully cover the required 37.5–42.5 GHz range. In principle, they could be used together within a switched-filter bank as presented in [112], selecting the most appropriate unit according to the operating frequency. Nevertheless, such a switching assembly would introduce additional losses, control complexity, and integration challenges at millimetre-wave frequencies, making it unsuitable for a demonstrator. For this reason, a waveguide solution was preferred. The Eravant SWF-40305340-22-B1, a WR-22 band-pass filter with approximately 2 dB insertion loss, provides a continuous 37–42 GHz passband and excellent out-of-band rejection (above 40 dB below 34 GHz and above 46 GHz). The unit is delivered with WR-22 interfaces and used with coaxial-to-waveguide transitions to interface the PCB transmitter front-end.

Finally the mixer was chosen. It must cover RF in 37.5–42.5 GHz with IF at 5.7 GHz with reference to packaged SMT for consistency with the receiver chain and project philosophy constraints. Table 4.5 compares COTS mixer options: the ADMV1550, already qualified in the receiver, spans 15–65 GHz as up/downconverter with DC–20 GHz IF and is selected to simplify reuse and procurement [75]. As alternatives, the Marki MM1-1453LSM-2 provides a QFN SMT option covering 14–53 GHz RF/LO, while the UMS CHM2179b98F offers a bare-die solution.

In Figure 4.4 the block diagram of the assembled Q-band transmitter

Part / Vendor	**RF/LO Range (GHz)**	**IF Range (GHz)**	**Form factor / Notes**
ADMV1550 (ADI), [75]	15–65	DC–20	SMT LCC
MM1-1453LSM-2 (Marki), [76]	14–53	DC–22	SMT, 4×4 mm QFN
CHM2179b98F (UMS), [113]	24–44 (family)	up to 20	Bare-die

Table 4.5: Mixer candidates for 37.5–42.5 GHz RF upconversion with 5.7 GHz IF.

front-end including the mixer is shown.

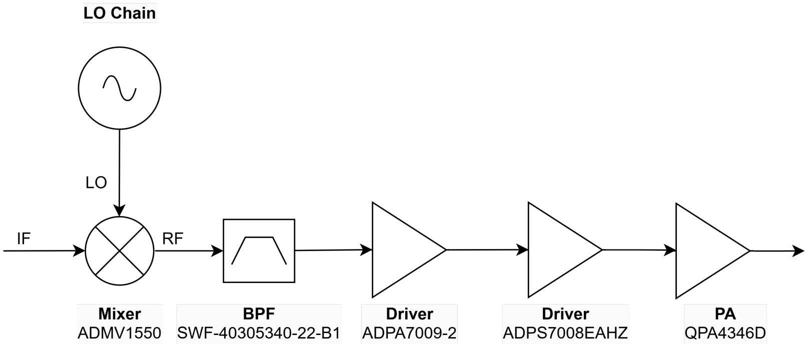

Figure 4.4: Block diagram of the assembled transmitter RF front-end and mixer.

The theoretical realized gain of the chain is shown in Table 4.6 where both small signal gain and large signal gain are calculated. Large signal gain is calculated starting by selecting the operating point of the PA which operates over its 1 dB compression point in order to maximize the PAE. From the datasheet input-output characteristics of the PA, the input power needed to drive it at its operating point is known and therefore also its large signal gain and the output power of the second driver. Doing the same for the second driver we can obtain its gain and the output power of the first driver. At this point the output power needed is around 16 dBm while the compression point of the first driver is around 29 dBm. The components are therefore operating in their linearity region where the small signal gain can be used.

	Mixer	**Driver 1**	**Driver 2**	**PA**	**TOT**
Small signal gain	-7 dB	17 dB	16 dB	16 dB	**42 dB**
Large signal gain	-7 dB	17 dB	14 dB	11 dB	**35 dB**

Table 4.6: Theoretical gain calculation for the designed transmitter RF front-end.

4.3 IF Chain

The IF chain was designed starting by the gain needed to reach the maximum output power at the output of the power amplifier. From the previous section, in Tab. 4.6 it is known that in the nominal operating conditions, so having the PA near its saturation point, the gain of the RF chain including the mixer is 35 dB.

It is also known that the maximum output power of the target SDR, in case of the transmitter being used ad upconverter, is 4 dBm and that the DAC has more than 15 dB of dynamics thanks to the digital attenuation feature [83]. In this case the minimum gain needed to drive the chain to its nominal maximum, 40 dBm, is 1 dB.

The transmitter shall also have enough gain to complete the bent-pipe transponder. In this case, it is known from the receiver chapter that the output power of the downconverter, calculated with the minimum input power and the LNA input and the maximum gain of the chain, is -6 dBm; this brings the needed transmitter IF gain to 11 dB.

It is chosen to reuse the same components of the receiver IF chain. Two gain block with 20 dB of nominal gain are used, the QPA9127, then a digital programmable attenuator, the HMC1119, is added to improve the dynamics and allow automatic level control systems. In the assembled and measured demonstrator, in analogy with what was done in the receiver, a 500 MHz filter was added. The final IF chain is shown in Figure 4.5.

4.4 Complete transmitter

In Figure 4.6 the complete block diagram of the assembled Q-band transmitter demonstrator is shown.

Linearity performances of the entire designed chain are evaluated in Figure 4.7 where output power and saturation power are plotted for each stage

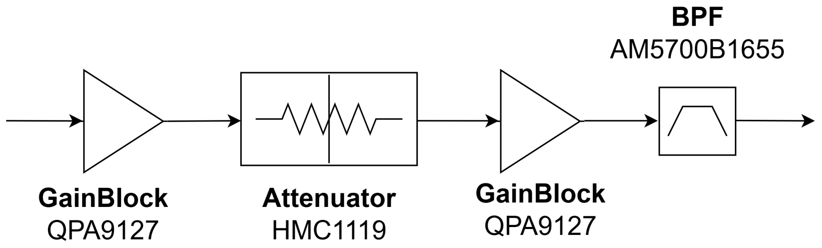

Figure 4.5: Block diagram of the assembled transmitter IF chain.

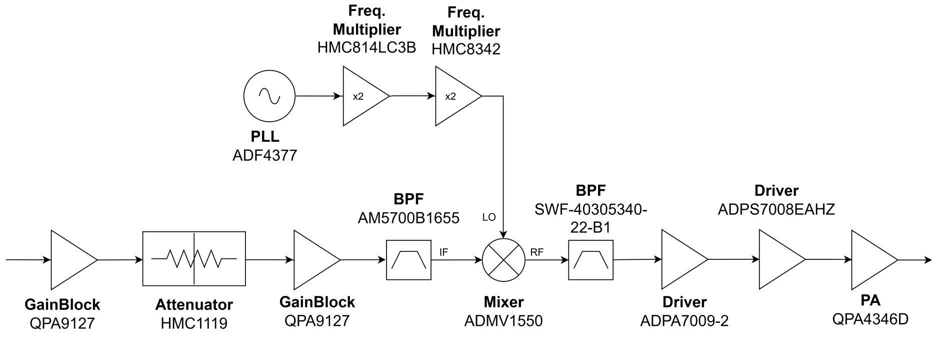

Figure 4.6: Block diagram of the assembled Q-band transmitter demonstrator.

of the chain. For this analysis, the bent pipe transponder case study is considered since it is more demanding from the gain point of view. For the analysis the attenuators of both the receiver and transmitter chains are set to 10 dB attenuation, under these conditions the input power to the transmitter is close to -20 dBm; it can be seen from the analysis that the operating point reached at the final power amplifier stage is slightly in compression, as desired. In this condition the maximum output power at the transmitter is reached with the minimum input power to the receiver and still having 20 dB of attenuator dynamics to increase gain in case of drops due to, for example, temperature rise. Dynamics in attenuation are also provided by the remaining 40 dB of the two attenuators.

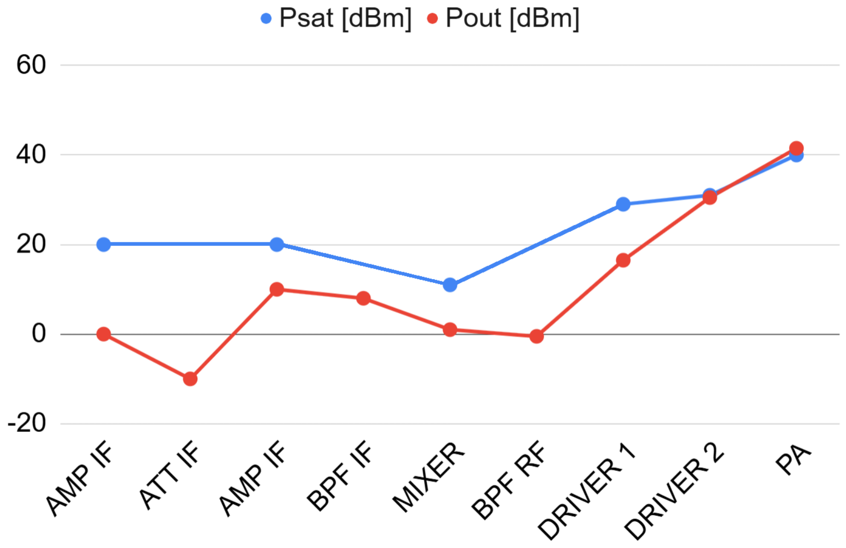

Figure 4.7: Output saturation point and output power at each stage of the transmitter chain.

4.4.1 Breadboarding and measurements

The complete Q-band transmitter demonstrator was assembled on a planar “flat” breadboard configuration, including the IF, LO, and RF front-end stages described in the previous sections. The prototype integrates the upconverter, driver, and solid-state power amplifier (SSPA) on a single metallic baseplate with coaxial interconnections. Figure 4.8 shows the assembled demonstrator.

In order to measure the transmitter chain components the setup shown in Figure 4.9 was employed.

A signal generator was used to generate signals at IF and a spectrum analyzer was used to measure the transmitter RF frequency output. 2.4 mm

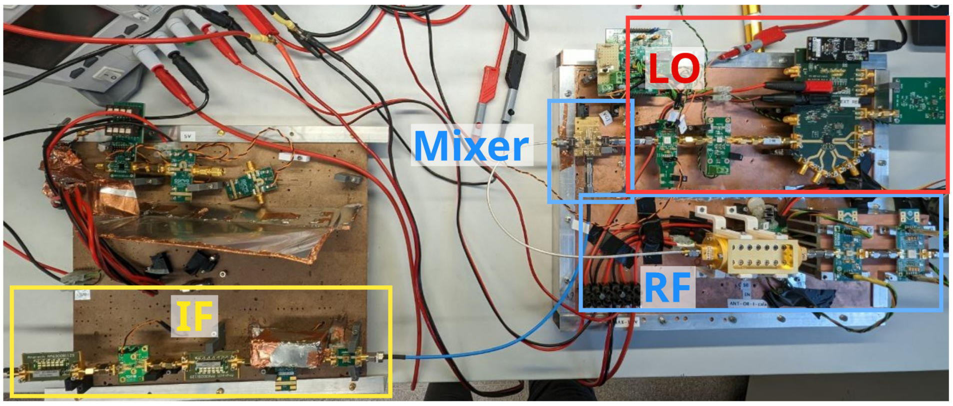

Figure 4.8: Photograph of the Q-band transmitter breadboard demonstrator.

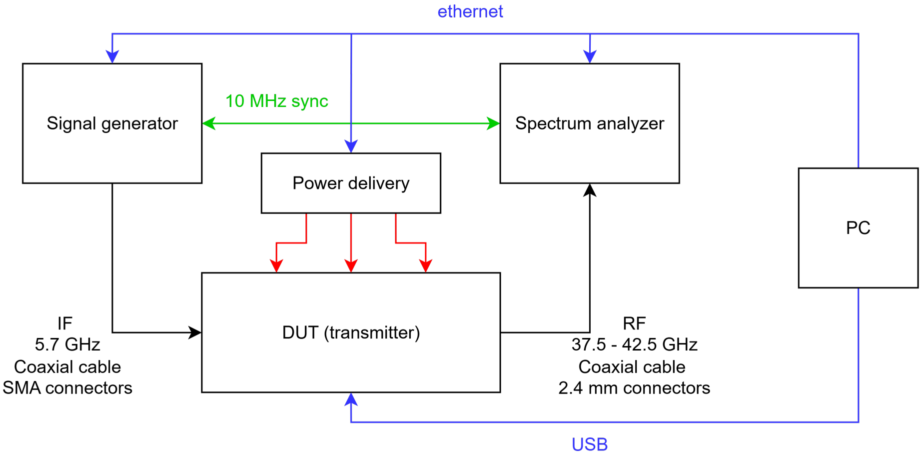

Figure 4.9: Transmitter measurement setup block diagram.

connectors were used, which have an operating frequency of up to 50 GHz. The DUT was powered by several DC power supplies needed to generate all different the voltages needed by the EVBs. The generator and the analyzer were synchronized using a 10 MHz reference and controlled by a PC using ethernet protocol as well as the power supplies. The DUT EVBs were controlled, by the same PC using an USB connection and the software provided by the manufacturer.

In Figure 4.10 a picture of the assembled measurements setup is shown.

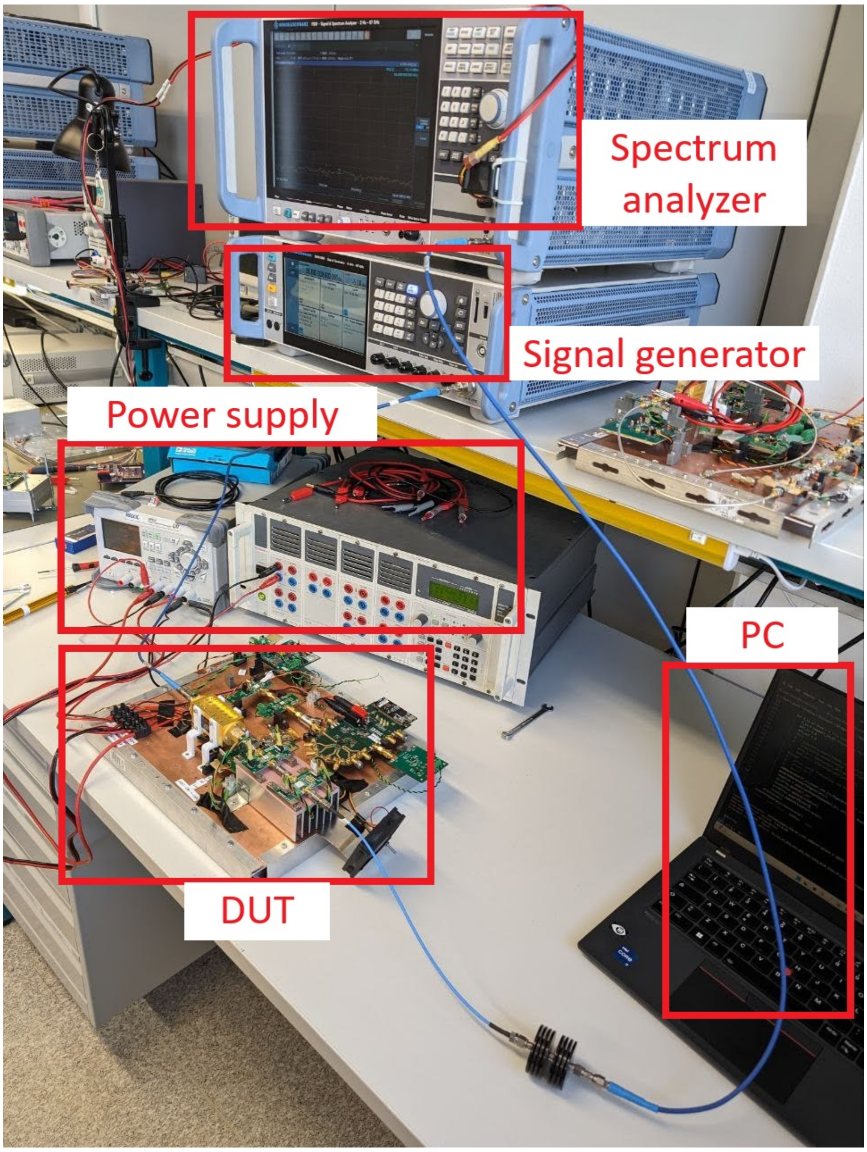

Figure 4.10: Picture of the transmitter measurements setup.

As a first measurement, the output power as a function of the input drive level was measured across the 37-43 GHz range. The results, reported in Figure 4.11, show a monotonic increase of the output power up to the SSPA saturation region, with a progressive reduction of gain for increasing input power as the amplifier approaches compression, totally in line with what was expected. A deterioration of the performances at frequencies higher than 42 GHz is also visible. This is due to the filter chosen, SWF-40305340-22-B1, which has its high cutoff frequency at 42 GHz and to the frequency response of the PA, which exhibits a slight drop in gain and saturation power starting at 42 GHz.

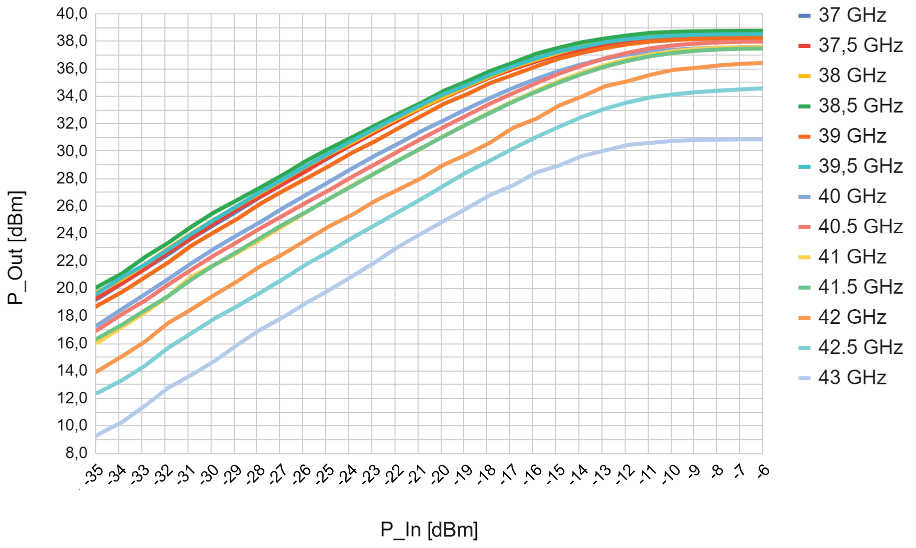

Figure 4.11: Measured output power (P_{out}) versus input power (P_{in}) across the operating frequency range. The curves illustrate the compression behaviour of the full transmitter chain.

Figure 4.12 presents the calculated gain as a function of the input power. The linear-region gain remains nearly constant in the 50 - 55 dB range up to approximately $P_{\text{in}} = -25\,\text{dBm}$. Beyond this point, gain compression progressively increases, reaching 1 dB degradation at $P_{\text{in}} = -18\,\text{dBm}$ (input $P_{1\text{dB}}$). As for the input-output characteristics at the upper band edge (42–43 GHz) a lower overall gain is observed, attributed to both the frequency response of the SSPA and the channel filter.

Figure 4.13 reports the measured local-oscillator leakage at the transmitter output, measured in dBc, as a function of input power. As expected, the leakage remains nearly independent of P_{in}, since it originates from imperfect isolation in the mixer and coupling paths rather than from the signal amplitude itself. At lower input powers, the leakage becomes dominant in relative terms because the modulated signal is weaker. At high input power, where

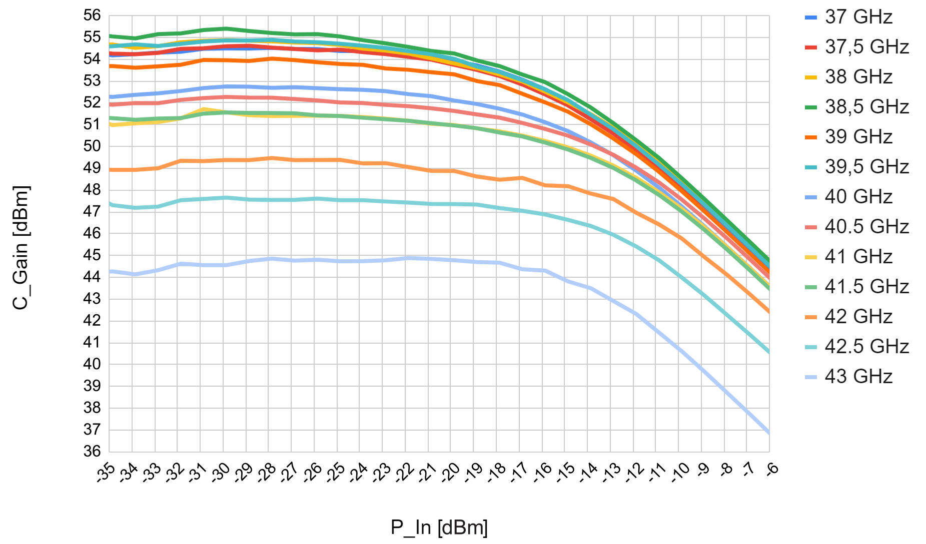

Figure 4.12: Measured overall gain versus input power. The chain provides about 47 dB small-signal gain with mild compression behaviour up to 0.5–1 dB near full drive.

the SSPA works at optimum efficiency, the LO leackage is also optimal and it is lower than -25 dBc up to 41.5 GHz output frequency. The leakage level increases toward higher RF frequencies, as the LO frequency approaches the low cutoff frequency of the channel filter.

To further increase the LO rejection, several strategies can be considered, although each presents non-negligible implementation complexity at breadboard level. The first approach consists in employing LO-nulling mixers, which integrate an adjustable cancellation network at the LO port to suppress leakage at the RF output. These architectures are often based on balanced or image-reject topologies with additional amplitude and phase trimming circuits [114, 115]. Despite their effectiveness, no commercially available COTS mixers implementing such LO-nulling capabilities were found at Q-band frequencies, making this solution impractical for the present demonstrator.

A second possible method is the adoption of a switched-sideband strategy, in which the upconversion mode is changed from upper-sideband (USB) to lower-sideband (LSB) when operating near the upper edge of the RF band. In this configuration, the LO frequency remains spectrally distant from the transmitted channel, thus mitigating the leakage issue. However, this approach requires LO generation frequencies exceeding 48 GHz in LSB mode for the highest output channels, which was incompatible with the available LO hardware and multiplier chain. A similar concept has been successfully

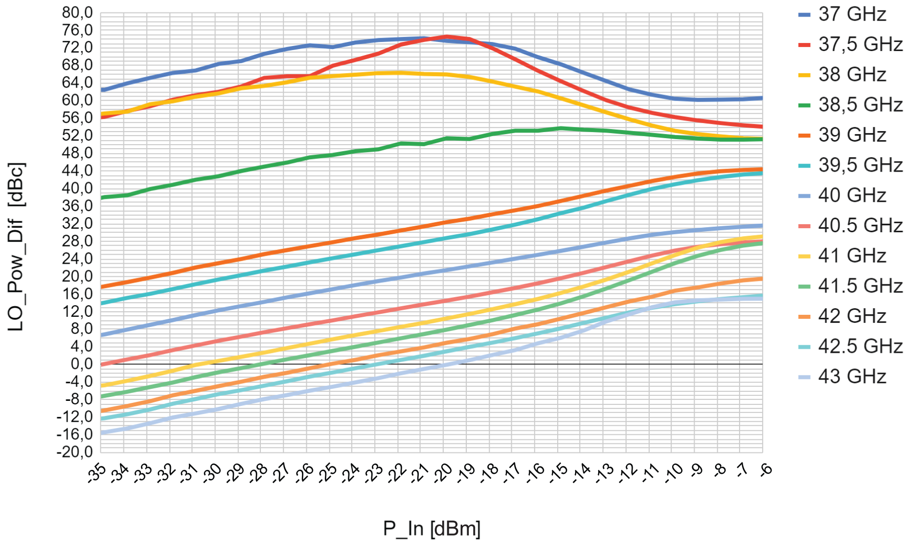

Figure 4.13: Measured LO leakage at the transmitter output versus input drive. The leakage is nearly independent of P_{in} and increases near the upper band due to reduced mixer isolation.

applied at Ka-band for flexible sideband selection in [116].

Finally, a complementary-filter system could be adopted, consisting of two switched band-pass filters where one filter operates in the lower portion of the band while the other covers the upper segment, ensuring that the LO always falls outside the active filter's transmission range. Nevertheless, this dual-path configuration requires additional routing, switching elements, and mechanical alignment, which were considered excessively complex for a flat demonstrator prototype.

In conclusion, the phase noise of the transmitted carrier was measured at 40 GHz with a measurement bandwidth from 100 Hz to 10 MHz offset. The trace shown in Figure 4.14 indicates a noise level of approximately -80 dBc/Hz at 10 kHz offset, gradually decreasing below -105 dBc/Hz beyond 1 MHz offset. The observed performance aligns with the expected scaling from the PLL reference, considering the overall ×4 LO multiplication factor of the transmitter chain.

When compared to typical communication system requirements, the obtained phase-noise spectrum comfortably satisfies the mask specified for DVB-S2 carrier modulations (e.g., QPSK and 8PSK) at 40 GHz, as defined by ETSI EN 302 307 [22]. The results confirm that the LO synthesis architecture preserve adequate spectral purity for broadband Q-band operation. Further analysis are presented in Chapter 5.

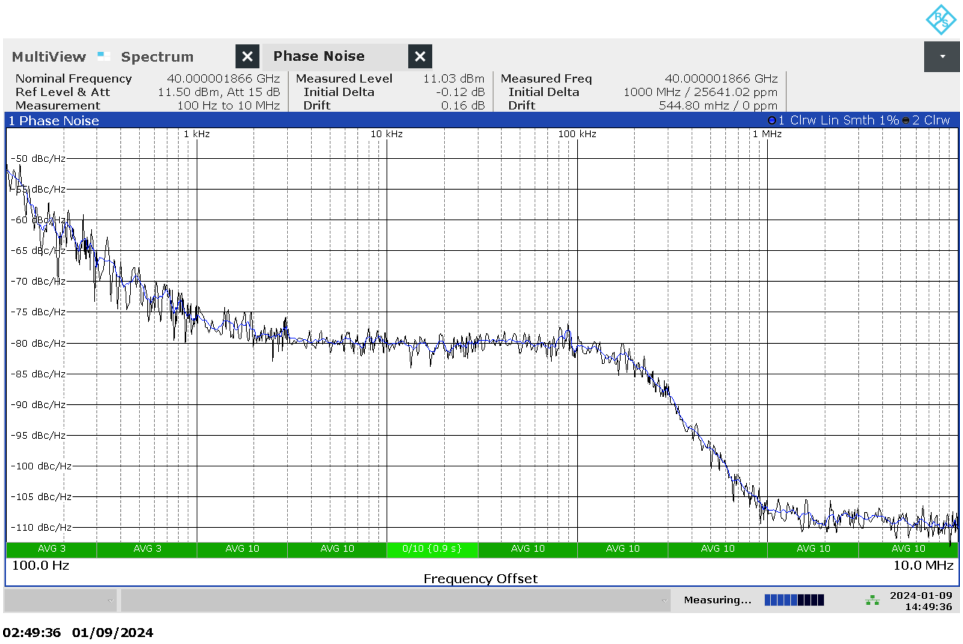

Nominal Frequency 40.000001866 GHz
Ref Level & Att 11.50 dBm, Att 15 dB
Measurement 100 Hz to 10 MHz

Measured Level 11.03 dBm
Initial Delta -0.12 dB
Drift 0.16 dB

Measured Freq 40.000001866 GHz
Initial Delta 1000 MHz / 25641.02 ppm
Drift 544.80 mHz / 0 ppm

Measuring...
2024-01-09
14:49:36

02:49:36 01/09/2024

Figure 4.14: Measured single-sideband phase noise of the transmitter at 40 GHz. The measured spectrum complies with the DVB-S2 mask requirements for Q-band transmission.

5. Performances evaluation

This chapter reports the transmitter and receiver measurements presented in Chapters 3 and 4. The measured front-end (FE) responses are abstracted into programmatic models for amplitude-to-amplitude (AM/AM) distortion, amplitude-to-phase (AM/PM) distortion, and phase noise (PN). The models are then exercised on digitally modulated DVB-S2 waveforms (QPSK, 8PSK, 16APSK, and 32APSK) to quantify constellation impairment and performance loss in symbol error rate (SER) as a function of signal-to-noise ratio (SNR) and output back-off (OBO). Finally, a feeder-link link budget is evaluated using the FE characteristics to demonstrate achievable margins for a Q/V-band LEO scenario.

All simulations are performed with a transmitter-centric view because the transmitter nonlinearity is the dominant source of constellation warping in the envisaged feeder links. Receiver figures (gain, NF) measured in Chapter 4 are used for the link budget.

No experimental measurements on modulated signals are presented, as the laboratory equipment used to perform the measurements reported in chapters 3 and 4 does not offer vector measurement options or protocol encoding/decoding.

5.1 Front-end behavioural modeling

The FE models are memoryless in the baseband sense (AM/AM and AM/PM depend only on the instantaneous input magnitude). This assumption is adequate for the measured chain of the transmitter, where the dominant nonlinear element is the saturated Solid State Power Amplifier (SSPA) operated with moderate OBO and where long electrical memory (bias networks, thermal droop) is negligible at the considered burst lengths and symbol rates [117, 118]. Phase noise is modeled as a separate multiplicative phase process applied to the complex envelope [119]. Additive white Gaussian noise (AWGN) is added after distortion to emulate the channel noise floor.

5.1.1 AMAM and AMPM distortion and model identification

Rather than enforcing a closed-form nonlinearity, the AM/AM law is taken directly from the measured TX input–output characteristic (Chapter 4). The procedure is as follows.

Let $x[n]$ denote the complex baseband input samples after pulse shaping and let $r_n = |x[n]|$. From swept measurements $\{P_{\text{in}}^{(k)}, P_{\text{out}}^{(k)}\}$ in dBm, the small-signal power gain in dB is computed as

$$G_{\text{dB}}^{(k)} = P_{\text{out}}^{(k)} - P_{\text{in}}^{(k)}.$$

An interpolating function is then constructed for both $P_{\text{out}}(P_{\text{in}})$ and $G_{\text{dB}}(P_{\text{in}})$. Values requested outside the measurement span are handled by holding the curve at the nearest measured endpoint. Classic closed-form amplifier model laws could have been implemented leading to similar results, such as the Rapp soft-limiter, which captures SSPA gain compression with a smoothness parameter p [120], and the Saleh model, which provides rational AM/AM and AM/PM laws originally developed for TWTAs [121]. For simplicity and in view of the adherence of the results to the theory and measurements in the datasheets, it was decided to use only interpolated measurements.

Let us define P_{sat} the measured saturation of the TX chain. Given a desired OBO (in dB), the target average output power is

$$\overline{P}_{\text{out}} = P_{\text{sat}} - \text{OBO}.$$

The corresponding average input power $\overline{P}_{\text{in}}$ is obtained by inverting the measured curve: $\overline{P}_{\text{in}} = P_{\text{in}}\left(\overline{P}_{\text{out}}\right)$ with $P_{\text{out}}(\cdot)$ from the interpolant. Let $E[r^2]$ denote the average symbol energy before distortion. Each sample is then power scaled by a factor p following the equation:

$$p_{\text{dB}} = \overline{P}_{\text{in}} - 10\,\log_{10}(E[r^2])$$

$$x'[n] = x[n] \cdot 10^{\frac{p_{\text{dB}}}{20}}$$

Consequently

$$P_{\text{in}}[n] = |x'[n]^2|$$

This preserves the constellation's PAPR and places its average at the input power that yields the chosen OBO. The instantaneous power gain $G_{\text{dB}}[n] = G_{\text{dB}}(P_{\text{in}}[n])$ is read from the interpolant. The amplitude scale factor is

$$a[n]{=}10^{G_{\text{dB}}[n]/20}.$$

The AM/AM-distorted baseband output is then

$$y_{\text{AMAM}}[n]{=}a[n] \cdot x[n]$$

For later use (AM/PM), the corresponding instantaneous *output* power is

$$P_{\text{out}}[n]{=}P_{\text{in}}[n]{+}G_{\text{dB}}[n].$$

This interpolation-based approach forces the simulation to follow the exact measured compression law of the implemented transmitter, including any gentle curvature around the knee and any gain droop at high drive.

Direct AM/PM measurements were not taken on bench. However, the device vendor supplied a phase rotation versus output power curve in the datasheet that is provided under NDA; therefore the curve is not reported here. Consequently, the simulations use the following purely empirical AM/PM mapping.

From pairs $\{P_{\text{out}}^{(k)}, \phi^{(k)}\}$ (phase in degrees) extrapolated from the datasheet, an interpolating function $\phi(P_{\text{out}})$ is built. As before, values outside the provided range are clamped. Using the instantaneous output powers $P_{\text{out}}[n]$ computed after AM/AM,

$$\phi[n]{=}\phi(P_{\text{out}}[n]) \quad \text{(degrees)} \quad \Rightarrow \quad \phi_{\text{rad}}[n]{=}\phi[n]\cdot\frac{\pi}{180}.$$

The final output is

$$y_{\text{AMPM}}[n]{=}y_{\text{AMAM}}[n]e^{j\,\phi_{\text{rad}}[n]}.$$

5.1.2 Phase-noise modelling

Phase noise is injected using the `comm.PhaseNoise` System object from MATLAB Communications Toolbox. Given a user-defined single-sideband (SSB) phase-noise mask $L(f)$ in dBc/Hz at specified offset frequencies, the object synthesises a discrete-time phase process $\{\phi_k\}$ by filtering Gaussian noise so that the spectrum of ϕ_k matches the target mask. Internally, for a single offset/level pair the object realises a $1/f$ spectrum via an IIR shaping filter; for vector specifications (multiple offsets/levels) it realises the mask with an FIR design that interpolates $L(f)$ on a $\log_{10} f$ grid, using appropriate regions (flat, $1/f^3$, and linear transitions) to approximate practical oscillator spectrum [122]. The complex output is then $y_k = x_k\, e^{j\phi_k}$.

The generation of the phase process ϕ_k and its application as a complex phasor is handled entirely by `comm.PhaseNoise`. In code, this corresponds to:

```
PN = comm.PhaseNoise(obj.dBc_Hz, obj.offsets, sampleRate);
reset(PN);
phasor = PN(ones(length(inputComplexSymbols),1));  % e^{j phi_k}
phi    = angle(phasor);
```

Here, `obj.dBc_Hz` and `obj.offsets` are the measured phase noise level/ offset pairs. The vector of ones simply requests a time series of phasors from the object with the required length; taking `angle` extracts ϕ_k. To emulate a receiver phase tracker (PLL) that removes slow phase drift but not fast jitter, the simulated phase is split into a slow component and a residual:

$$\phi_{\text{slow}}[k] = \text{LPF}\{\phi[k]\}_{f_c=\text{Band}}$$

$$\phi_{\text{res}}[k] = \phi[k] - \phi_{\text{slow}}[k].$$

The low-pass cutoff `Band` (Hz) represents the tracking bandwidth of the hypothetical carrier/phase loop. Only the residual is applied to the symbols:

$$y[k]{=}x[k]e^{j\,\phi_{\text{res}}[k]}.$$

In MATLAB this is:

```
phi_slow = lowpass(phi, Band, sampleRate);
phi_res  = phi - phi_slow;
outputSymbols = inputComplexSymbols .* exp(1j*phi_res);
```

This approach reproduces the observed behaviour in the constellations: arc-shaped spreading at high SNR (dominated by fast PN) while avoiding unrealistically large common-mode rotations that a practical tracker would remove. The same approach is explained in [119] and [123] for digital receivers and then applied specifically for OFDM in [124].

5.2 Waveform generation and impairment injection

Each DVB-S2 modulation is generated as follows. A long random symbol sequence (at least 10^6 symbols) is Gray-mapped onto the target constellation (QPSK, 8PSK, 16APSK, 32APSK) with ring radius and relative ratios per ETSI [22]. Symbols are upsampled and shaped with a root-raised-cosine (RRC) filter with roll-off $\alpha = 0.20$ unless otherwise stated. The complex envelope is then passed through the FE model:

1. ensure the desired OBO by scaling the PA input;
2. apply AM/AM and AM/PM;
3. sample and apply the PN process;
4. add AWGN to reach the target SNR.

SER is estimated by ideal coherent detection: after matched filtering with perfect timing and carrier recovery (up to an unknown but fixed complex gain), each received sample is decided by nearest–neighbour slicing on the known DVB-S2 reference constellation. No adaptive equaliser or decision-directed compensation is applied, so the measured SER reflects only the injected AM/AM, AM/PM, and residual phase-noise impairments plus AWGN.

5.3 Constellation impairment: visual assessment

A first, intentionally visual, test inspects the clouding of the received constellation as SNR varies while OBO is fixed at 3 dB. Figures 5.1–5.4 show QPSK, 8PSK, 16APSK and 32APSK examples with colour layers for different SNRs. The expected features are evident: at high SNR the phase-noise process produces arc-shaped spreads around the nominal angles and as SNR decreases, AWGN dominates and the symbol clusters overlap.

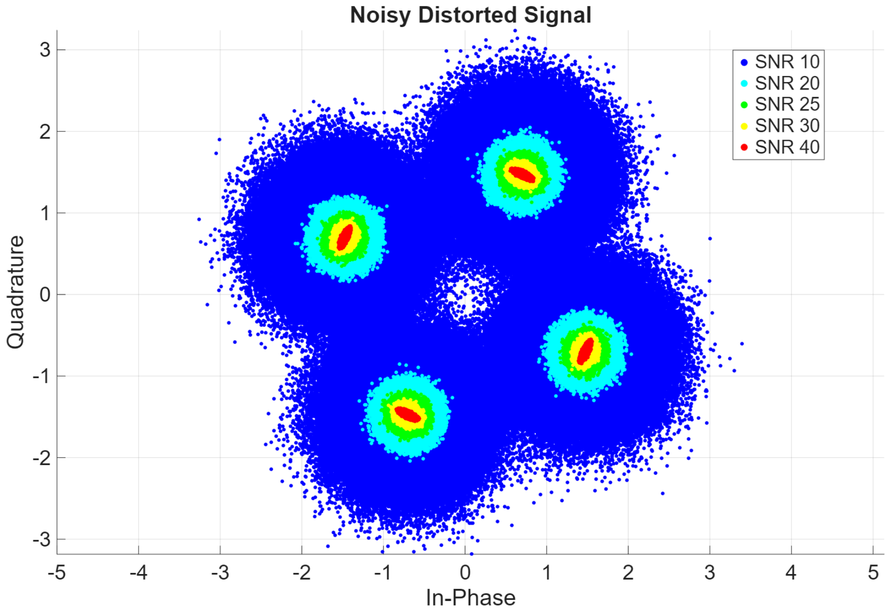

Figure 5.1: QPSK constellation with combined AM/AM, AM/PM and PN at OBO$=$ 3 dB and several SNR values.

5.4 SER versus SNR and back-off optimization

Quantitative performance is assessed by sweeping SNR and repeating the simulation for multiple OBO values. For each modulation, the resulting SER vs. SNR curves are compared with the theoretical AWGN reference where no phase noise and no nonlinearity are applied. As OBO increases, operation moves away from compression and the curves approach the theoretical limit, at the cost of reduced radiated power and hence reduced SNR for a given scenario.

To optimize the OBO value to be used for a given modulation, a useful compact metric is the SNR degradation at a fixed target SER (here 10^{-4}), that can be defined as

$$\Delta\gamma(\mathrm{OBO}){=}\gamma_{\mathrm{req}}(\mathrm{OBO}) - \gamma_{\mathrm{th}}, \tag{5.4.1}$$

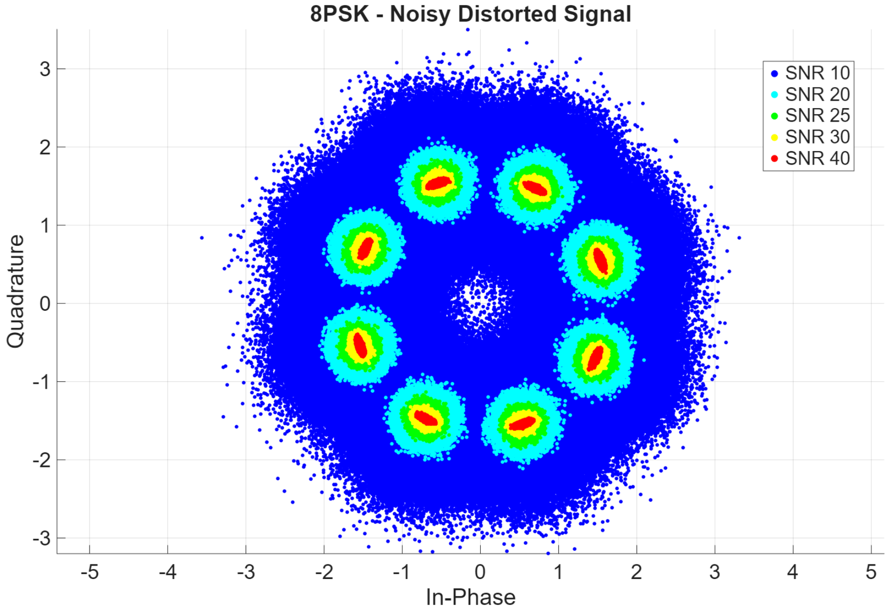

Figure 5.2: 8PSK constellation with combined AM/AM, AM/PM and PN at OBO= 3 dB and several SNR values.

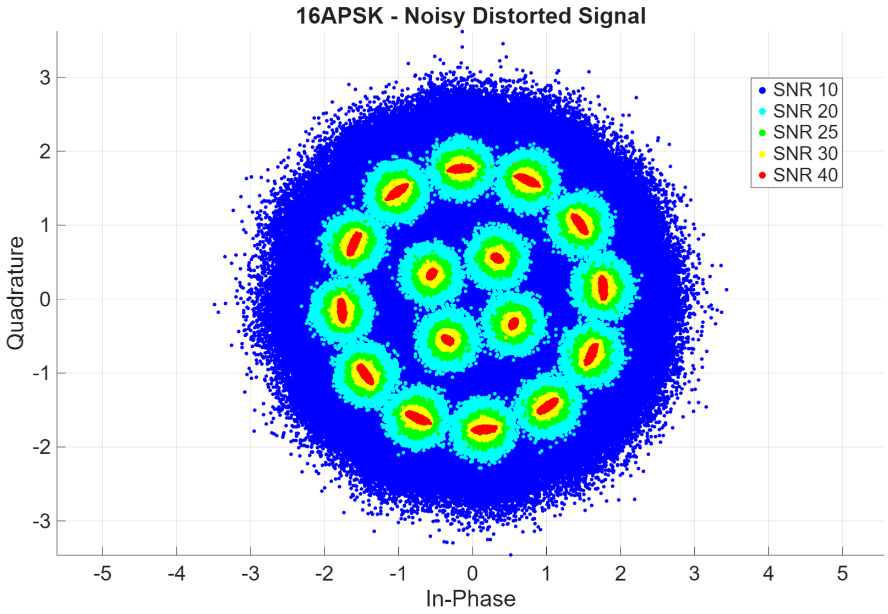

Figure 5.3: 16APSK constellation with combined AM/AM, AM/PM and PN at OBO= 3 dB and several SNR values.

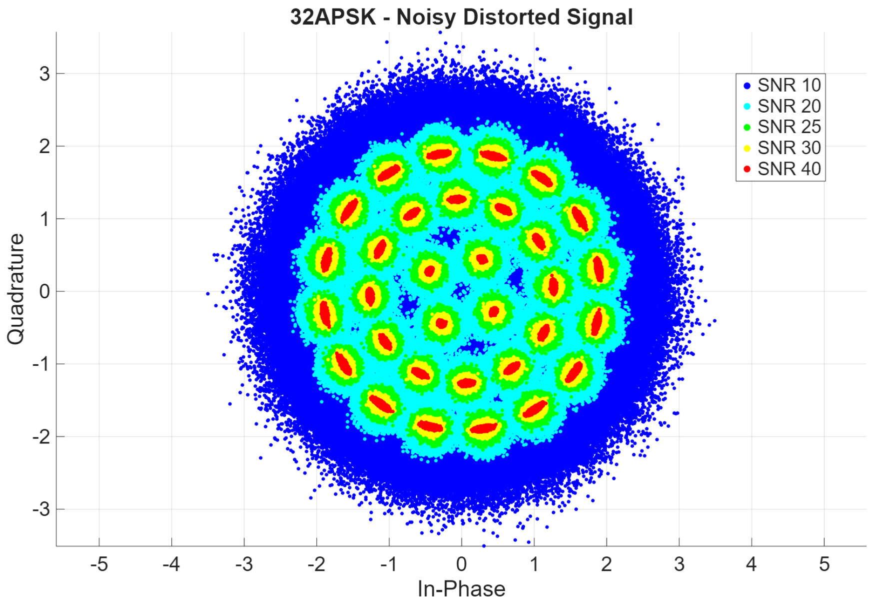

Figure 5.4: 32APSK constellation with combined AM/AM, AM/PM and PN at OBO= 3 dB and several SNR values.

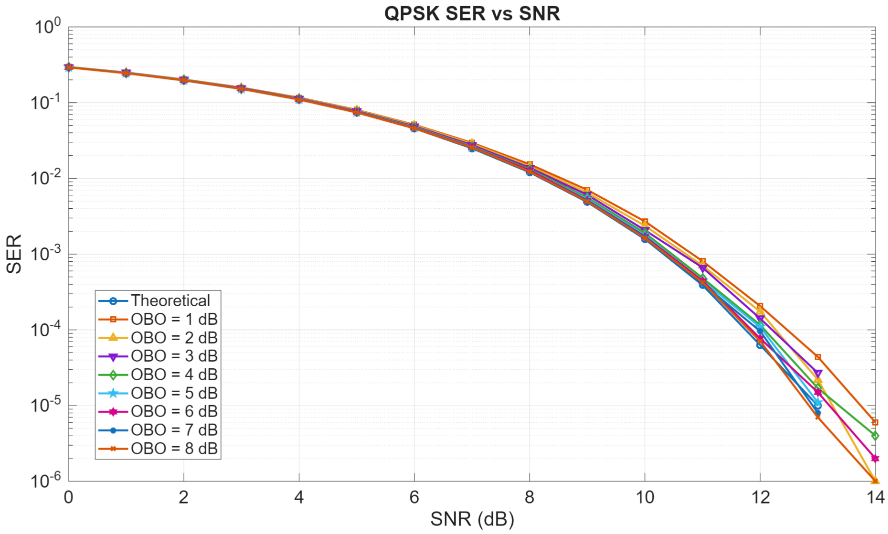

Figure 5.5: QPSK SER vs SNR for different OBO values. Theoretical reference included.

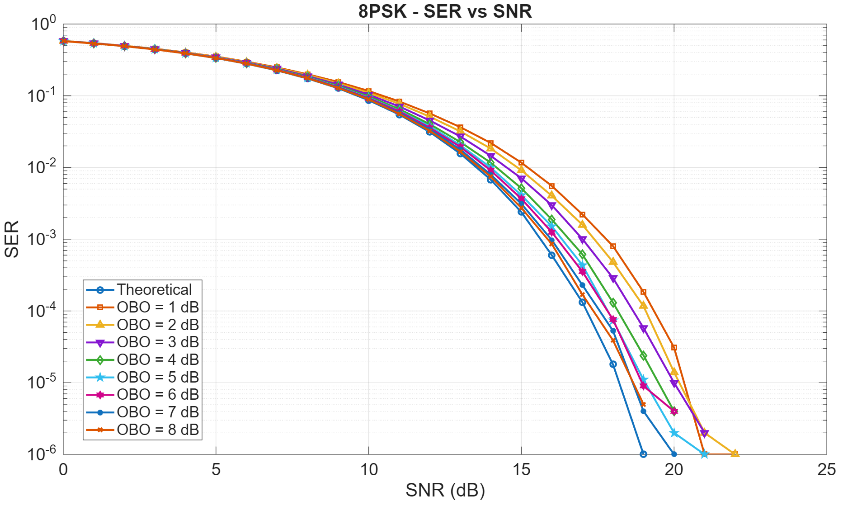

Figure 5.6: 8PSK SER vs SNR for different OBO values. Theoretical reference included.

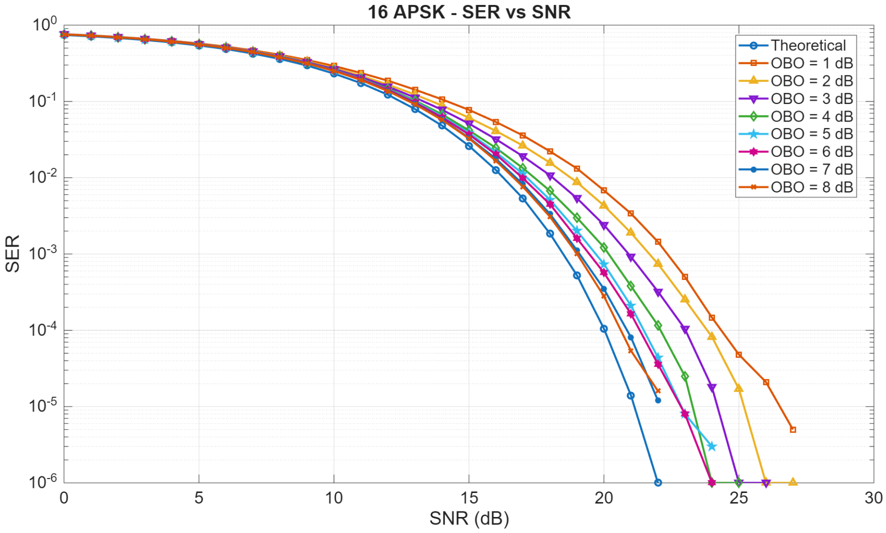

Figure 5.7: 16APSK SER vs SNR for different OBO values. Theoretical reference included.

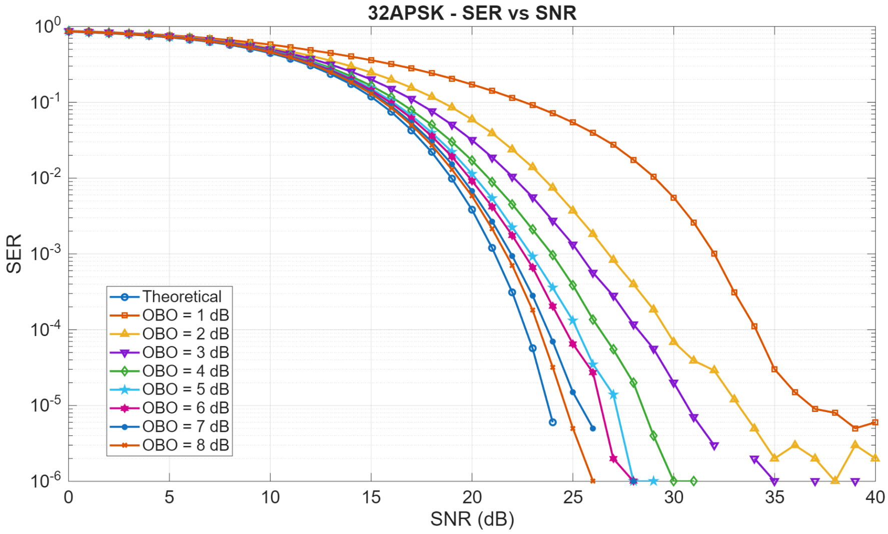

Figure 5.8: 32APSK SER vs SNR for different OBO values. Theoretical reference included.

where γ_{th} is the theoretical SNR required in AWGN and $\gamma_{\text{req}}(\text{OBO})$ is the SNR required with the impaired chain at a given OBO. For constant-envelope PSK the optimum is trivial (operate as close as possible to saturation). For APSK, because constellation rings have different instantaneous amplitudes, there exists an optimum that balances compression loss (small OBO) and radiated-power loss (large OBO). Figures 5.10 and 5.9 show the curve of SNR degradation vs. OBO respectively for 16APSK and 32APSK. It can be seen that for 32APSK the optimum OBO is around 4 dB while for 16APSK the optimum is around 1 dB. This is justified by the fact that the modulations considered have been standardized for satellite use and consequently designed to work well even close to saturation in order to maximize efficiency.

It is important to note that the simulations conducted do not take into account channel coding, which would have an improving effect on the SNR threshold required to obtain a given SER. Consequently, OBO optimizations would also shift in favour of lower OBOs, improving the final efficiency of the system.

5.5 Link budget using the synthesised FE

This section evaluates the results obtained through the study of a end-to-end link budget that uses the measured RX noise figure and the TX operating point at the selected OBO. Uplink and downlink are evaluated separately and then combined for a transparent bent-pipe payload.

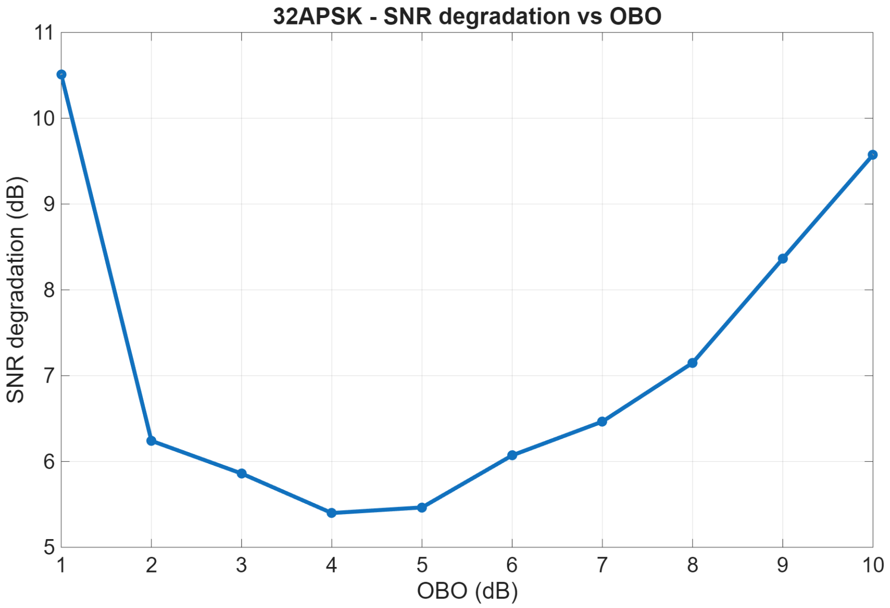

Figure 5.9: 32APSK: SNR degradation at SER=10^{-4} versus OBO. The minimum occurs at $\approx 4\,\text{dB}$.

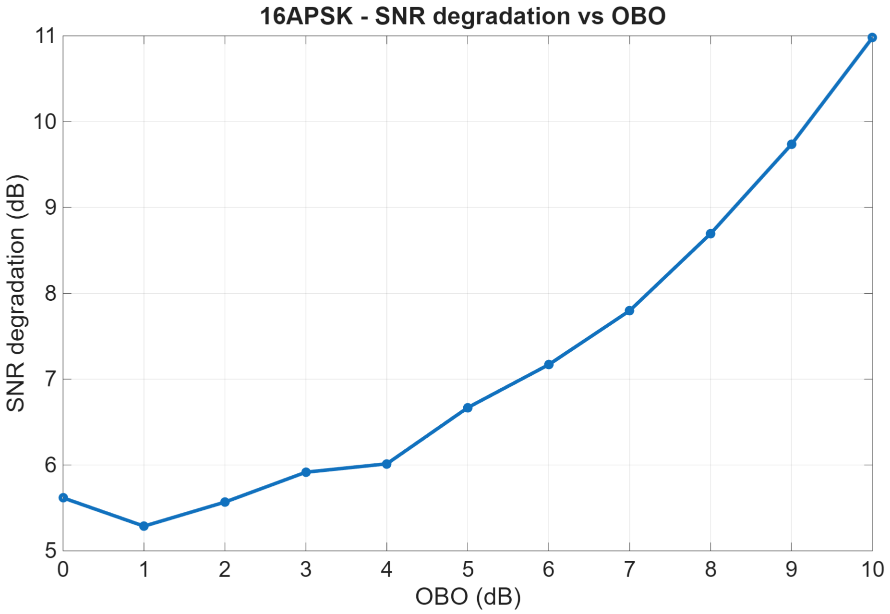

Figure 5.10: 16APSK: SNR degradation at SER=10^{-4} versus OBO. The minimum occurs at $\approx 1\,\text{dB}$.

5.5.1 Scenario and parameters

The satellite is a LEO platform at $h = 550\,\mathrm{km}$. Antenna pointing errors are neglected considering the state of practice: modern small-satellite ADCS and ground tracking can reach sub-degree accuracies with negligible pointing loss compared to the antenna beamwidth [125]. Atmospheric attenuation is modeled by a simple zenith loss with an elevation-dependent secant mapping [126, 127]. Table 5.1 summarizes the parameters used in the end to end link budget calculation.

On the satellite, a compact $\sim 30\,\mathrm{cm}$ aperture antenna is assumed. Modeling the gain as a paraboloid [128] with efficiency $\eta \approx 0.6$ yields to:

$$G\,[\mathrm{dBi}] = 10\log_{10}(\eta(\frac{\pi D}{\lambda})^2) \tag{5.5.1}$$

where D is the paraboloid diameter and λ is the wavelength. The formula gives about G=39.8 dBi at 40 GHz (λ=7.5 mm) and G=41.7 dBi at 50 GHz (λ=6 mm). On the ground, a 3 m feeder antenna (typical for LEO gateways) with η=0.6 provides about 60 dBi at 40 GHz and 61.7 dBi at 50 GHz.

Transmit powers and receiver noise figures on the satellite side are consistent with Chapters 3-4 while on the ground, to keep the budget conservative, the transmitter does not rely on TWT amplifiers; instead, a solid-state chain delivering about 20 W RF output is assumed. On the receiver side, a noise figure of 2 dB is adopted as a common reachable value for a temperature-controlled front end at 40 GHz.

5.5.2 Budget equations and results

The free-space path loss is $L_{\mathrm{fs}} = (4\pi R/\lambda)^2$ with slant range $R(e)$ as a function of elevation e (spherical Earth geometry [125]). The SNR at the receiver is

$$\gamma = \frac{P_{\mathrm{tx}} G_{\mathrm{tx}} G_{\mathrm{rx}}}{L_{\mathrm{fs}} L_{\mathrm{atm}} L_{\mathrm{tx}} L_{\mathrm{rx}}\, k T_{\mathrm{sys}} B}, \tag{5.5.2}$$

with k the Boltzmann constant, B the noise bandwidth, and T_{sys}, noise temperature of the system, derived from the noise figure and pre-LNA losses. Uplink and downlink SNRs $\gamma_{\mathrm{UL}}(e)$ and $\gamma_{\mathrm{DL}}(e)$ are computed separately.

For a transparent bent-pipe transponder where uplink and downlink noise contributions are independent and referred to the user receiver, the end-to-end SNR combines as the harmonic sum [125, 129]:

$$\frac{1}{\gamma_{\mathrm{TOT}}} = \frac{1}{\gamma_{\mathrm{UL}}} + \frac{1}{\gamma_{\mathrm{DL}}}. \tag{5.5.3}$$

Margins are defined as $\mathrm{Margin}(e) = \gamma(e) - \gamma_{\mathrm{min}}$, where γ_{min} is the SNR required for SER$= 10^{-4}$ with 32APSK (section 5.4). Figure 5.11 reports the uplink, downlink, and transparent bent-pipe case margins versus elevation. Positive margins are obtained across the full pass, including at 5° elevation.

Table 5.1: Key parameters for the LEO transparent feeder link budget.

Quantity	**Uplink (50 GHz)**	**Downlink (40 GHz)**
Carrier frequency f [GHz]	50.0	40.0
Signal bandwidth B [GHz]	1.0	
Satellite altitude h [km]	550	
Elevation range [deg]	5 to 90	
TX RF power P_{tx} [W]	20	2.8
TX antenna gain G_{tx} [dBi]	61.7	39.8
RX antenna gain G_{rx} [dBi]	41.7	60.0
TX chain loss L_{tx} [dB]	1.0	1.0
RX pre-LNA loss L_{rx} [dB]	1.0	1.0
RX noise figure NF_{rx} [dB]	4.0	2.0
Zenith atmospheric loss [dB]	0.3	0.2
Required SNR target [dB] (SER= 10^{-4}, 32APSK)	22.5	

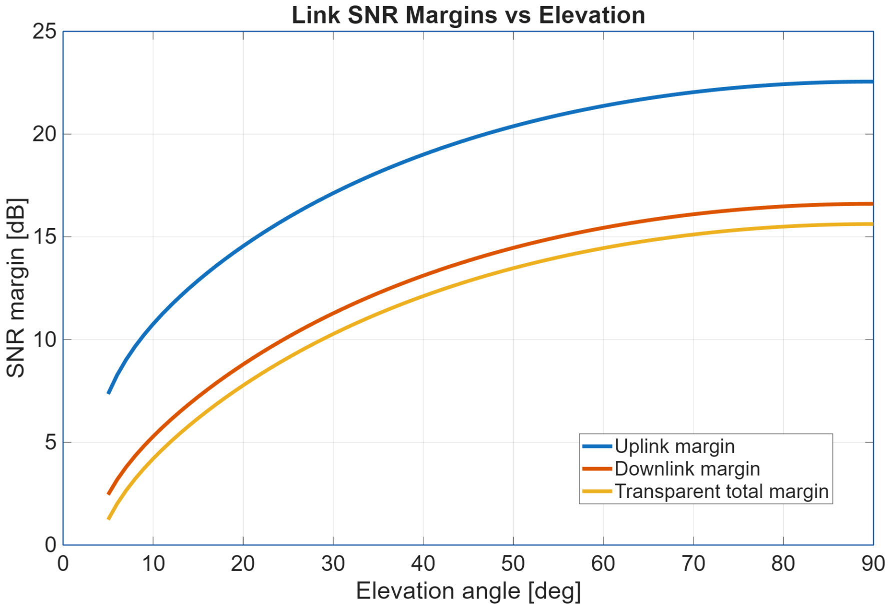

Figure 5.11: Uplink, downlink, and transparent SNR margins versus elevation for the parameters in Table 5.1.

With a roll-off $\alpha = 0.20$ and occupied bandwidth $B = 1\,\text{GHz}$, the symbol rate is

$$R_s = \frac{B}{1+\alpha} = \frac{1\,\text{GHz}}{1.2} \approx 833 \text{ Msym/s}. \tag{5.5.4}$$

For 32APSK with DVB-S2X code rate 9/10, the nominal spectral efficiency is $\eta \approx 4.45\,\text{bit/sym}$ [22], leading to a coded user rate of

$$R_{\text{user}} \approx \eta\, R_s \approx 3.71 \text{ Gbit/s}, \tag{5.5.5}$$

while the raw uncoded rate at 5 bits/sym is $\approx 4.17\,\text{Gbit/s}$. These values exclude framing and higher-layer overheads.

In conclusion the chapter presents an end-to-end modeling flow that starts from laboratory FE measurements and produces realistic DVB-S2 impairment simulations and a consolidated feeder-link budget. Memoryless AM/AM and AM/PM models fitted to the measured transmitter, together with a measured-based phase-noise process, reproduce the observed constellation spreading. SER analyses versus SNR and OBO quantify the trade-off between compression loss and radiated power loss for APSK. With these settings, the transparent LEO Q/V-band feeder link using COTS hardware achieves positive margins down to low elevations and supports multi-Gbit/s user rates, confirming the viability of the proposed architecture.

6. Conclusions

This thesis aimed to demonstrate that a Q/V–band satellite front–end suitable for small satellites can be designed, assembled, and validated using commercial off–the–shelf components while supporting both transparent and regenerative operating modes. The motivation comes from the growing demand for high–capacity feeder links and the relative lack of documented regenerative Q/V prototypes for small spacecraft in the academic literature. By adopting a device–first, modular methodology the work delivers a practical architecture, measured hardware, and modeling tools that together form a reproducible baseline for future research and early stage industrialization.

A superheterodyne transceiver architecture with a common IF at 5.7 GHz was developed to cover the Q/V feeder–link ranges (downlink 37.5–42.5 GHz, uplink 47.2–52.4 GHz). On the receiver side, a V–band front–end based on packaged LNAs and a broadband SMT mixer was built and characterized. Measurements confirm a cascade gain in the 55–65 dB range and an overall noise figure around 4 dB for the RF front–end, driven by an LO chain that however, according to the data sheets, operates up to 44 GHz only. Actual required LO frequency is up to 46 GHz but measurement demonstrated how, with sufficient drive thanks to cascaded active doublers, the conversion was performed correctly. The IF section integrates gain control to accommodate both narrowband transparent operation and SDR–based regenerative tests. On the transmitter side, a Q–band up–conversion chain was realized reusing the IF and the LO chains of the receiver. Particular attention was payed to the power amplification chain composed by two driving stages (medium power amplifiers) and a SSPA reaching more than 6W of output power. End–to–end behavioural modeling (AM/AM, AM/PM, phase noise) was used together with measured device data to generate constellations, to estimate symbol–error rates versus SNR, and to guide output–back–off choices that balance efficiency and waveform integrity. Finally, a link–budget analysis conducted with the synthesized FE parameters demonstrated clear–sky margins compatible with small–satellite feeder links and highlighted the sensitivity to propagation fades demonstrating the feasibility of multi-Gigabit links.

The results show that Q/V–band front–ends for small satellites can be reliably prototyped at low cost using packaged COTS parts, provided that bias sequencing, LO generation, and filtering are treated carefully. Moreover, the same hardware supports a regenerative mode by attaching commercial SDRs/modems at IF, an operating scenario largely missing in the academic literature at these frequencies.

This dual–mode capability directly serves academic evaluation of advanced waveforms and on–board processing, while offering industry a rapid path to de–risk architectures ahead of custom MMIC or flight–model developments. Beyond the specific hardware, the thesis contributes a design and measurement methodology that is accessible to research laboratories and teaching environments, thereby reducing barriers to practical experimentation with millimeter waves.

The prototype is a flat-model demonstrator optimized for functionality and measurement access rather than mass, volume, or space qualification. Going forward, the local-oscillator chain should be improved to provide higher drive beyond 46 GHz with greater margin and lower phase noise. Improving the LO frequency response and spectral purity will also benefit the mixer's frequency conversion by reducing spurious responses and relaxing constraints in the IF/LO plan. In parallel, channel filtering can be refined (e.g., using SIW/LTCC or groove-gap waveguide solutions) to raise out-of-band rejection while minimizing insertion loss. On the path to space readiness, two main future actions can be envisioned. The first consolidates a "careful COTS" approach (part screening and derating, radiation analyses for TID/SEE, and environmental/lifetime testing) to build the qualification evidence base. The second is the engineering and industrialization track, in which the prototype is miniaturized and mechanically integrated into the target flight-oriented form factor (thermal design, harnessing, mass/volume reduction), culminating in the Engineering Model (EM) to be taken forward to qualification. As a more academic future plan, integration with active antennas for multibeam scenario suggests a system-level study—covering beamforming and allocation strategies, gateway diversity, interference and spurious coexistence, and constellation-level capacity impacts. Each of these developments can be pursued incrementally, leveraging the modularity of the present design.

In summary, this thesis demonstrates the feasibility of Q/V–band front–ends for small satellites using COTS, and provides measured evidence, models, and design choices that are directly reusable by the community. In doing so, it bridges a concrete gap between the state of the art on transparent Q/V payloads and the emerging interest in regenerative transceivers, offering a pragmatic platform for further research and industrial maturation.

Bibliography

[1] Oltjon Kodheli, Eva Lagunas, Nicola Maturo, Shree Krishna Sharma, Bhavani Shankar, Jesus Fabian Mendoza Montoya, Juan Carlos Merlano Duncan, Danilo Spano, Symeon Chatzinotas, Steven Kisseleff, Jorge Querol, Lei Lei, Thang X. Vu, and George Goussetis. Satellite communications in the new space era: A survey and future challenges. *IEEE Communications Surveys & Tutorials*, 23(1):70–109, 2021. `doi:10.1109/COMST.2020.3028247`.

[2] Amazon Web Services. AWS Ground Station. Online, 2025. URL: `https://aws.amazon.com/ground-station/`.

[3] European Space Agency. European Data Relay Satellite System (EDRS) Overview. Online, 2024. URL: `https://www.esa.int/Applications/Connectivity_and_Secure_Communications/EDRS`.

[4] ITU-R. IMT Vision—Framework and Overall Objectives of the Future Development of IMT for 2020 and Beyond. Technical Report M.2083-0, International Telecommunication Union, 2015. URL: `https://www.itu.int/dms_pubrec/itu-r/rec/m/R-REC-M.2083-0-201509-I!!PDF-E.pdf`.

[5] 3GPP. Tr 38.811: Study on new radio (NR) to support non-terrestrial networks. Technical Report V15.4.0, 3rd Generation Partnership Project, 2020.

[6] 3GPP. Tr 38.821: Solutions for NR to support non-terrestrial networks (NTN). Technical Report V16.1.0, 3rd Generation Partnership Project, 2021.

[7] 3GPP. Study on Using Satellite Access in 5G. TR 38.822, 3rd Generation Partnership Project, 2018. Release 16, v16.0.0. URL: `https://www.3gpp.org/`.

[8] K. Liolis, A. Geurtz, D. Sperber, D. Schulz, S. Watts, G. Poziopoulou, B. Evans, N. Wang, O. Vidal, B. Tiomela Jou, M. Fitch, S. Sendra Diaz, P. Sayyad Khodashenas, and N. Chuberre. Use cases

and scenarios of 5G integrated satellite–terrestrial networks for enhanced mobile broadband: The SaT5G approach. *International Journal of Satellite Communications and Networking*, 37(2):91–112, 2019. `doi:10.1002/sat.1245`.

[9] N. H. Crisp, P. C. E. Roberts, S. Livadiotti, V. Oiko, et al. The Benefits of Very Low Earth Orbit for Earth Observation Missions: Thematic Analysis and Parametric Study. *Acta Astronautica*, 176:104–119, 2020. `doi:10.1016/j.paerosci.2020.100619`.

[10] X. Cao, P. Yang, M. Alzenad, X. Xi, D. Wu, and H. Yanikomeroglu. Airborne communication networks: A survey. *IEEE Journal on Selected Areas in Communications*, 36(9):1907–1926, 2018. `doi:10.1109/JSAC.2018.2864423`.

[11] S. Karapantazis and F.-N. Pavlidou. Broadband communications via high-altitude platforms: A survey. *IEEE Communications Surveys & Tutorials*, 7(1):2–31, 2005. `doi:10.1109/COMST.2005.1423332`.

[12] CCSDS. TM Synchronization and Channel Coding, Blue Book. Technical Report 131.0-B-3, Consultative Committee for Space Data Systems, 2017. URL: `https://ccsds.org/Pubs/131x0b3s.pdf`.

[13] CCSDS. TC Synchronization and Channel Coding, Blue Book. Technical Report 231.0-B-3, Consultative Committee for Space Data Systems, 2017. URL: `https://ccsds.org/Pubs/231x0b3s.pdf`.

[14] A. D. Panagopoulos, P.-D. M. Arapoglou, and P. G. Cottis. Satellite communications at Ku, Ka, and V bands: Propagation impairments and mitigation techniques. *IEEE Communications Surveys & Tutorials*, 6(3):2–14, 2004. `doi:10.1109/COMST.2004.5342290`.

[15] E. Cianca, T. Rossi, A. Yahalom, Y. Pinhasi, J. Farserotu, and C. Sacchi. EHF for satellite communications: The new broadband frontier. *Proceedings of the IEEE*, 99(11):1858–1881, 2011. `doi:10.1109/JPROC.2011.2158765`.

[16] Recommendation ITU-R P.676-13: Attenuation by atmospheric gases, 2019.

[17] Recommendation ITU-R P.838-3: Specific attenuation model for rain, 2005.

[18] Recommendation ITU-R P.840-8: Attenuation due to clouds and fog, 2019.

[19] Recommendation ITU-R P.618-13: Propagation data and prediction methods for the design of earth–space telecommunication systems, 2017.

[20] E. Cianca, C. Stallo, M. Lucente, T. Rossi, M. Ruggieri, G. Parca, A. D'Amico, and L. Bruca. Transponders: Effectiveness of propagation impairments mitigation techniques at Q/V band. In *Proc. IEEE GLOBECOM Workshops*, 2008. `doi:10.1109/GLOCOMW.2008.ECP.12`.

[21] A. Gharanjik, K. Liolis, M. R. B. Shankar, and B. Ottersten. Large scale transmit diversity in Q/V band feeder link with multiple gateways. In *Proc. IEEE PIMRC*, pages 766–770, 2013. `doi:10.1109/PIMRC.2013.6666239`.

[22] Digital video broadcasting (DVB); second generation framing structure, channel coding and modulation systems for broadcasting, interactive services, news gathering and other broadband satellite applications (dvb-s2), 2014. URL: `https://www.etsi.org/deliver/etsi_en/302300_302399/30230701/01.04.01_20/en_30230701v010401a.pdf`.

[23] Digital video broadcasting (DVB); part 2: DVB-S2 extensions (DVB-S2X), 2021. URL: `https://www.etsi.org/deliver/etsi_en/302300_302399/30230702/01.03.01_20/en_30230702v010301a.pdf`.

[24] E. Cha. *InP HEMT Design for Cryogenic Low-Noise Amplifiers*. PhD thesis, Georgia Institute of Technology, 2019.

[25] J. Schleeh. Ultra-low noise InP HEMTs for cryogenic amplification. Technical report, Chalmers University of Technology, 2012.

[26] Patrick Ettore Longhi, Lorenzo Pace, Sergio Colangeli, Walter Ciccognani, and Ernesto Limiti. Technologies, design, and applications of low-noise amplifiers at millimetre-wave: State-of-the-art and perspectives. *MDPI Electronics*, 8(11), 2019. URL: `https://www.mdpi.com/2079-9292/8/11/1222`, `doi:10.3390/electronics8111222`.

[27] Masaru SATO, Yoshitaka Niida, Toshiaki Suzuki, Yasuhiro NAKASHA, Yoichi KAWANO, Takehisa Iwai, Naoki HARA, and Kazukiyo JOSHIN. Robust Q-band InP- and GaN-HEMT low noise amplifiers. *IEICE Transactions on Electronics*, E100.C:417–423, 05 2017. `doi:10.1587/transele.E100.C.417`.

[28] R. Giofrè, F. Costanzo, A. Massari, A. Suriani, F. Vitulli, E. Limiti, et al. A 20 W GaN-on-Si solid state power amplifier for Q-band space communication systems. In *Proc. IEEE MTT-S International Microwave Symposium (IMS)*, 2020. `doi:10.1109/IMS30576.2020.9223808`.

[29] R. Giofrè, E. Limiti, A. Massari, A. Suriani, F. Vitulli, et al. 20 W linearized Q-band solid state power amplifier for satellite communication application. In *Proc. European Microwave Conference (EuMC)*, 2021. `doi:10.23919/EUMC48046.2021.9338114`.

[30] Shane Verploegh, Mauricio Pinto, Laila Marzall, Daniel Martin, Gregor Lasser, and Zoya Popović. Analysis of process variations in W-band GaN MMIC PAs using nonparametric statistics. volume 69, pages 2304–2318, 2021. `doi:10.1109/TMTT.2021.3058270`.

[31] H. Lee, I. Han, and I. Ju. Design of a compact, highly efficient, and high-power Q-/V-band SiGe HBT cascode power amplifier with a four-way wilkinson power combiner balun. *IEEE Journal of Solid-State Circuits*, 60(5):1594–1606, 2025. `doi:10.1109/JSSC.2024.3523867`.

[32] Neal Robbins, David Eze, Helen Cohen, Xiaoling Zhai, William McGeary, William Menninger, Morgan Chen, and Eddie Rodgers. Space qualified 200-Watt Q-band linearized traveling-wave tube amplifier. In *2018 IEEE International Vacuum Electronics Conference (IVEC)*, pages 13–14, 2018. `doi:10.1109/IVEC.2018.8391521`.

[33] M. Aloisio, P. Angeletti, F. Coromina, and R. De Gaudenzi. Exploitation of Q/V-band for future broadband telecommunication satellites. In *Proc. IEEE IVEC*, 2012. `doi:10.1109/IVEC.2012.6262191`.

[34] W. Abbas, Z. Mehmood, and M. Seo. A V-band phase-locked loop with a novel phase-frequency detector in 65 nm CMOS. *MDPI Electronics*, 9(9):1502, 2020. `doi:10.3390/electronics9091502`.

[35] V.-S. Trinh et al. A 78.8–84 GHz phase-locked loop synthesizer for a W-band FMCW radar in 65 nm CMOS. *MDPI Sensors*, 22(9), 2022. `doi:10.3390/s22103626`.

[36] C.-C. Wang, Z. Chen, and P. Heydari. W-band silicon-based frequency synthesizers using injection-locked and harmonic triplers. *IEEE Transactions on Microwave Theory and Techniques*, 60(5):1307–1320, 2012. `doi:10.1109/TMTT.2011.2180399`.

[37] Augustine O. Nwajana and Emenike Raymond Obi. A review on SIW and its applications to microwave components. *MDPI Electronics*, 11(7), 2022. URL: `https://www.mdpi.com/2079-9292/11/7/1160`, `doi:10.3390/electronics11071160`.

[38] T.-H. Yang, C.-F. Chen, T.-Y. Huang, C.-L. Wang, and R.-B. Wu. A 60 GHz LTCC transition between microstrip line and substrate integrated waveguide. In *Proc. Asia-Pacific Microwave Conference*, 2005. `doi:10.1109/APMC.2005.1606294`.

[39] C. Máximo-Gutiérrez et al. Compact wideband groove-gap waveguide bandpass filter. *MDPI Sensors*, 23(13):6234, 2023. `doi:10.3390/s23136234`.

[40] Yiqun Liu, Xiaoli Xi, Xinyu Niu, Fengjuan Wang, and Kai-Da Xu. E-plane waveguide bandpass filters based on high-order modes of spoof surface plasmon polaritons. *Materials & Design*, 246:113309, 2024. URL: `https://www.sciencedirect.com/science/article/pii/S0264127524006841`, `doi:10.1016/j.matdes.2024.113309`.

[41] C. Stallo, M. Lucente, T. Rossi, E. Cianca, M. Ruggieri, A. Paraboni, et al. Transponders: Research and analysis for the development of telecommunication payloads in Q/V bands. In *Proc. IEEE Aerospace Conference*, pages 1–5, 2009. `doi:10.1109/AERO.2009.4839341`.

[42] F. Di Cola, A. Pandolfi, G. Di Paolo, J. Rivera, E. Benzi, A. Martellucci, M. Schmidt, J. Ebert, F. Cuervo, S. Falzini, P. Salaris, E. Coviello, E. De Viti, C. Riva, L. Luini, G. Codispoti, E. Russo, and G. Parca. Alphasat Aldo Paraboni payload IOT campaign and status after the first year of operation. In *2016 IEEE Aerospace Conference*, pages 1–13, 2016. `doi:10.1109/AERO.2016.7500946`.

[43] Tommaso Rossi, Mauro De Sanctis, Marina Ruggieri, Carlo Riva, Lorenzo Luini, Giuseppe Codispoti, Enrico Russo, and Giorgia Parca. Satellite communication and propagation experiments through the alphasat Q/V band Aldo Paraboni technology demonstration payload. *IEEE Aerospace and Electronic Systems Magazine*, 31(3):18–27, 2016. `doi:10.1109/MAES.2016.150220`.

[44] Tommaso Rossi, Mauro De Sanctis, Ernestina Cianca, Giuseppe Codispoti, Giorgia Parca, and Marina Ruggieri. A decade of EHF scientific research: Unveiling insights from alphasat q/v-band satellite communication experiments. *International Journal of Satellite Communications and Networking*, n/a(n/a). URL: `https://onlinelibrary.wiley.com/doi/abs/10.1002/sat.1532`, `arXiv:https://onlinelibrary.wiley.com/doi/pdf/10.1002/sat.1532`, `doi:10.1002/sat.1532`.

[45] C. Riva et al. Four-year propagation results from the asi alphasat experiment, 2021. Politecnico di Milano repository.

[46] Jyotsna Ladkani, Naman Agarwal, Eramangalath Geeta S, Jayesh Thakkar, Abhay Jain, and Dinesh Kumar Singh. Space qualified Q/V band receiver for high throughput communication satellites. In *2022 IEEE Microwaves, Antennas, and Propagation Conference (MAPCON)*, pages 259–263, 2022. `doi:10.1109/MAPCON56011.2022.10047010`.

[47] Naresh Deo. High power transmitters for Q/V-band communications-beyond alphasat. In *2019 IEEE Aerospace Conference*, pages 1–6, 2019. `doi:10.1109/AERO.2019.8741907`.

[48] Q/V-feed project (dual-CP feed covering 37.5–43.5 GHz and 47.2–51.4 GHz). `https://connectivity.esa.int/projects/qvfeed`, 2017.

[49] ECC decision (21)01 on the use of the bands 47.2–50.2 GHz and 50.4–52.4 GHz by the fixed-satellite service (earth-to-space). `https://docdb.cept.org/download/3733`, 2021.

[50] Doug Sinclair and Jonathan Dyer. Radiation effects and cots parts in smallsats. In *27th Annual AIAA/USU Conference on Small Satellites (SSC13-IV-3)*, Logan, UT, USA, 2013.

[51] EEE-INST-002: Instructions for EEE parts selection, screening, qualification and derating. `https://nepp.nasa.gov/docuploads/FFB52B88-36AE-4378-A05B2C084B5EE2CC/EEE-INST-002_add1.pdf`, 2003.

[52] ECSS-Q-ST-30-11C Rev.2: Derating – EEE components. `https://ecss.nl/standard/ecss-q-st-30-11c-rev-2-derating-eee-components-23-june-2021/`, June 2021.

[53] Behzad Razavi. Design considerations for direct-conversion receivers. In *IEEE Transactions on Circuits and Systems II: Analog and Digital Signal Processing*, volume 44, pages 428–435, 1997. URL: `https://www.seas.ucla.edu/brweb/papers/Journals/RTCAS97.pdf`, `doi:10.1109/82.592569`.

[54] Behzad Razavi. *RF Microelectronics*. Prentice Hall, 2 edition, 2012. URL: `https://picture.iczhiku.com/resource/eetop/WYKgsQqKzSDpFmbM.pdf`.

[55] Direct RF-series FPGAs and SoCs: Wideband devices product brief. `https://cdrdv2-public.intel.com/785876/direct-rf-wideband-product-brief.pdf`, September 2025.

[56] B. Esposito et al. Intel Agilex 9 Direct RF-series FPGAs (hot chips 2023 handout). `https://hc2023.hotchips.org/assets/program/conference/day2/FPGAs%20Cooling/HC2023.Intel.Agilex9DirectRF.FPGAs.Handout.final.29Aug2023.pdf`, 2023.

[57] Michael Curtin and Paul O'Brien. *Ask the Applications Engineer—30: PLL Synthesizers*, 2002. Analog Dialogue. URL: `https://www.analog.com/en/resources/analog-dialogue/articles/pll-synthesizers.html`.

[58] Analog Devices, Inc. *ADF4377: Low Jitter Dual-Output Microwave Synthesizer with Integrated VCO*, 2022. URL: `https:`

//www.analog.com/media/en/technical-documentation/data-sheets/adf4377.pdf.

[59] Analog Devices, Inc. *ADF4371: Microwave Wideband Synthesizer with Integrated VCO*, 2021. URL: `https://www.analog.com/media/en/technical-documentation/data-sheets/adf4371.pdf`.

[60] Texas Instruments. *LMX2820: 22.6-GHz Wideband RF Synthesizer*, 2021. URL: `https://www.ti.com/lit/ds/symlink/lmx2820.pdf`.

[61] Analog Devices, Inc. *HMC814LC3B: x2 Active Broadband Frequency Multiplier, 13–24.6 GHz Output*, 2015. URL: `https://www.mouser.com/datasheet/3/1014/1/hmc814-1370601.pdf`.

[62] Inc. Analog Devices. *HMC573LC3B: x2 Active Broadband Frequency Multiplier, 8–22 GHz Output*, 2014. v03 datasheet. URL: `https://www.analog.com/media/en/technical-documentation/data-sheets/hmc573.pdf`.

[63] Inc. Analog Devices. *HMC598: GaAs MMIC x2 Active Frequency Multiplier, 22–46 GHz Output*, 2015. v01.0809 datasheet. URL: `https://www.analog.com/media/en/technical-documentation/data-sheets/hmc598.pdf`.

[64] Analog Devices, Inc. *HMC8342: x2 Active Broadband Frequency Multiplier, 22–42 GHz Output*, 2020. URL: `https://www.analog.com/media/en/technical-documentation/data-sheets/hmc8342.pdf`.

[65] Eravant. SFA-282SF-S1: 26.5 to 40 GHz, +20 dBm X2 active frequency multiplier, 2024. URL: `https://www.eravant.com/26-5-to-40-ghz-20-dbm-output-power-wr-28-waveguide-ka-band-x2-active-frequency-multiplier`.

[66] Eravant. 22 to 44 GHz X2 active frequency multiplier (uni-guide series), 2024. URL: `https://www.eravant.com/22-to-44-ghz-16-dbm-output-power-in-line-wr-28-wg-ka-band-x2-active-frequency-multiplier-uni-guide`.

[67] Kagan Kaya. *AN-1363 - Meeting Biasing Requirements of Externally Biased RF/Microwave Amplifiers with Active Bias Controllers.* Analog Devices, August 2018. Rev. A.

[68] Qorvo. *Application Note - GaN Bias Circuit Design Guidelines*, October 2019. Rev. A.

[69] Ampleon. *AN11130 - Bias module for 50 V GaN demonstration boards*, September 2015. Rev. 2.

[70] Inc. Analog Devices. *HMC920LP5E: Bias Controller for GaAs/ GaN pHEMT Power Amplifiers*, 2018. Datasheet, Rev. A. URL: `https://www.analog.com/media/en/technical-documentation/data-sheets/hmc920.pdf`.

[71] Analog Devices. *MT-080: Mixers and Modulators*, 2009. Tutorial. URL: `https://www.analog.com/media/en/training-seminars/tutorials/MT-080.pdf`.

[72] Analog Devices, Inc. *ADL8106: GaAs, pHEMT, Low Noise Amplifier, 18 GHz to 54 GHz*, 2023. Rev. B Datasheet. URL: `https://www.analog.com/media/en/technical-documentation/data-sheets/adl8106.pdf`.

[73] Analog Devices, Inc. *ADL7003: 50 GHz to 95 GHz, GaAs, pHEMT, MMIC, Wideband LNA*, 2021. Datasheet. URL: `https://www.analog.com/media/en/technical-documentation/data-sheets/adl7003.pdf`.

[74] Inc. Qorvo. *TGA4811: DC–60 GHz Low Noise Amplifier (gain block)*, 2006. URL: `https://www.qorvo.com/products/p/TGA4811`.

[75] Inc. Analog Devices. *ADMV1550: General-Purpose Double Balanced Mixer, 15 GHz to 65 GHz*, 2023. Datasheet Rev. 0. URL: `https://www.analog.com/media/en/technical-documentation/data-sheets/admv1550.pdf`.

[76] Marki Microwave. *MM1-1453LSM-2: 14–53 GHz GaAs MMIC Double-Balanced Mixer, QFN*, 2024. Datasheet. URL: `https://markimicrowave.com/assets/ff5e53fd-30d4-40c2-865b-93ae450ba1ce/MM1-1453LSM-2-GaAs%20MMIC%20Double%20Balanced%20Mixer.pdf`.

[77] Analog Devices. *AN-1039: Correcting Imperfections in IQ Modulators to Improve RF Signal Fidelity*, 2012. Application Note. URL: `https://www.analog.com/en/resources/app-notes/an-1039.html`.

[78] Richard J. Cameron, Chandra M. Kudsia, and Raafat R. Mansour. *Microwave Filters for Communication Systems: Fundamentals, Design, and Applications.* Wiley, Hoboken, NJ, 2 edition, 2018. URL: `https://onlinelibrary.wiley.com/doi/book/10.1002/9781119292371`.

[79] Reger Eline. Image rejection requirements and transmit power control requirements for low cost IEEE 802.16 OFDM radio transceiver implementations. Technical Report C80216d-03/77, IEEE 802.16 Broadband Wireless Access Working Group, 2003. URL: `https://www.ieee802.org/16/tgd/contrib/C80216d-03_77.pdf`.

[80] Inc. / Eravant SAGE Millimeter. *SWF-52310350-15-B1: Waveguide Bandpass Filter, V-Band, 47 to 57 GHz*, 2018. URL: `https://sftp.eravant.com/content/datasheets/SWF-52310350-15-B1.pdf`.

[81] Inc. Virginia Diodes. WR15BPF50.1-57.7 waveguide bandpass filter, 2025. URL: `https://www.vadiodes.com/en/products-6/waveguide-filters-bpf-lpf-hpf`.

[82] Inc. Virginia Diodes. WR19BPFE45.5-52.6 bandpass filter, wr-19 waveguide, 2025. URL: `https://www.vadiodes.com/en/products-6/waveguide-filters-bpf-lpf-hpf`.

[83] Analog Devices, Inc. *AD9081: MxFE Quad, 16-Bit, 12 GSPS RF DAC and Quad, 12-Bit, 4 GSPS RF ADC*, 2021. URL: `https://www.analog.com/media/en/technical-documentation/data-sheets/ad9081.pdf`.

[84] Inc. Qorvo. *QPA9127: High Linearity Gain Block Amplifier, 1 GHz to 6 GHz*, 2024. Datasheet Rev. C, Feb 26, 2024. URL: `https://www.qorvo.com/products/p/QPA9127`.

[85] Analog Devices. *RF Signal Chain Discourse Part 2: Essential Building Blocks*, 2022. Analog Dialogue article. URL: `https://www.analog.com/en/resources/analog-dialogue/articles/rf-signal-chain-discourse-part-2-essential-building-blocks.html`.

[86] Analog Devices. *AN-2618: RF System Development with High-Speed Data Converters*, 2020. Application Note. URL: `https://www.analog.com/en/resources/app-notes/an-2618.html`.

[87] Inc. Anatech Electronics. 5700 MHz ceramic band pass filter (AM5700B1128), 2023. Product page / datasheet listing. URL: `https://anatechelectronics.com/in-stock/band-pass-filters/ceramic-band-pass-filters/5700-mhz-ceramic-band-pass-filter.html`.

[88] D. Shin, D. Kang, and K. Lee. A highly efficient E-band CMOS frequency tripler with a third-harmonic boosting technique. In *IEEE MTT-S International Microwave Symposium (IMS)*, pages 1–3, 2013. `doi:10.1109/LMWT.2023.3269065`.

[89] P. Chou, C. Lee, and T. Wu. A 60-GHz CMOS frequency tripler with broadband performance. *IEEE Microwave and Wireless Components Letters*, 20(1):31–33, 2010. `doi:10.1109/LMWC.2009.2036792`.

[90] Mini-Circuits. *CY3-453-D+: 3X Die Frequency Multiplier, Output 20–45 GHz*, 2023. Product page. URL: `https://www.minicircuits.com/WebStore/dashboard.html?model=CY3-453-DG%2B`.

[91] Eravant (SAGE Millimeter). *Uni-Guide™ X3 Active Frequency Multiplier, 28–32 GHz, +18 dBm (WR-28)*, 2024. URL: `https://www.eravant.com/28-to-32-ghz-18-dbm-output-power-in-line-wr-28-wg-ka-band-x3-active-frequency-multiplier-uni-guide`.

[92] BQ Microwave / AT Microwave. Coaxial frequency multipliers up to 110 ghz (family overview), 2025. Brochure. URL: `https://www.bq-microwave.de/wp-content/uploads/2025/02/Coaxial-Frequency-Multipliers-up-to-110-GHz-www.bq-microwave.de_.pdf`.

[93] S. Nayak et al. 0.15 μm GaN MMIC manufacturing technology for 2–50 GHz applications. In *CS MANTECH Conference*, pages 1–4, 2015. URL: `https://csmantech.org/wp-content/acfrcwduploads/field_5e8cddf5ddd10/post_2933/3.1_013.pdf`.

[94] Joel Moron, Remy Leblanc, Francois Lecourt, and Peter Frijlink. 12w, 30% PAE, 40 GHz power amplifier MMIC using a commercially available GaN/Si process. pages 1457–1460, 06 2018. `doi:10.1109/MWSYM.2018.8439689`.

[95] Bumjin Kim and Vivian Li. 39GHz GaN front end MMIC for 5G applications. pages 1–4, 10 2017. `doi:10.1109/CSICS.2017.8240473`.

[96] Hao Lu, Meng Zhang, Ling Yang, Bin Hou, Rafael Perez Martinez, Minhan Mi, Jiale Du, Longge Deng, Mei Wu, Srabanti Chowdhury, Xiaohua Ma, and Yue Hao. A review of GaN RF devices and power amplifiers for 5G communication applications. *Fundamental Research*, 5(1):315–331, 2025. URL: `https://www.sciencedirect.com/science/article/pii/S2667325823003023`, `doi:10.1016/j.fmre.2023.11.005`.

[97] Inc. Qorvo. *QPA4246D: 37.5–42.5 GHz 10 W GaN Power Amplifier (die)*, 2024. Product page. URL: `https://www.qorvo.com/products/p/QPA4246D`.

[98] Inc. Qorvo. *QPA4346D: 37.5–42.5 GHz 6 W GaN Power Amplifier (die)*, 2024. Product page. URL: `https://www.qorvo.com/products/p/QPA4346D`.

[99] Inc. Qorvo. *QPA4446D: 37.5–42.5 GHz 4 W GaN Power Amplifier (die)*, 2024. Product page. URL: `https://www.qorvo.com/products/p/QPA4446D`.

[100] MACOM Technology Solutions. *MAAP-011423-DIE: 37–43 GHz 7.5 W GaN Power Amplifier (die)*, 2024. Product page. URL: `https://www.macom.com/products/product-detail/MAAP-011423-DIE`.

[101] United Monolithic Semiconductors (UMS). *CHA8454-99F: 37.5–43.5 GHz 10 W High Power Amplifier (die)*, 2024. Product brief / distributor page. URL: `https://www.microrel.com/mmic/ums-cha8454-99f-a-37-5-43-5ghz-10w-high-power-amplifier/`.

[102] Inc. Analog Devices. *ADPA7008: 22–40 GHz, 31 dBm PSAT, 17.5 dB Gain, Packaged PA*, 2023. Product page. URL: `https://www.analog.com/en/products/adpa7008.html`.

[103] Analog Devices, Inc. *ADPA7009-2: 20 to 54 GHz, 0.5 W Power Amplifier with On-Chip Detector*, 2022. Datasheet (Rev. 0). URL: `https://www.analog.com/media/en/technical-documentation/data-sheets/adpa7009-2.pdf`.

[104] Inc. Qorvo. *QPA2040D: 20–40 GHz 2 W GaN Power Amplifier (die)*, 2023. Product page. URL: `https://www.qorvo.com/products/p/QPA2040D`.

[105] MACOM Technology Solutions. *MAAP-011379-DIE: 20–55 GHz, 1 W Distributed Power Amplifier (die)*, 2024. Datasheet. URL: `https://cdn.macom.com/datasheets/MAAP-011379.pdf`.

[106] MACOM Technology Solutions. *MAAM-011291-DIE: 20–45 GHz, 1 W Power Amplifier (die)*, 2020. Datasheet, Rev. V1. URL: `https://cdn.macom.com/datasheets/MAAM-011291-DIE.pdf`.

[107] Eravant (SAGE Millimeter). *SWF-40305340-22-B1: Q-Band Waveguide Bandpass Filter, 37 to 42 GHz*, 2023. Product page. URL: `https://www.eravant.com/37-to-42-ghz-passband-40-db-rej-dc-to-34-ghz-and-46-to-60-ghz-q-band-wr-22-wg-bandpass-filter`.

[108] Eravant (SAGE Millimeter). *SWF-40320340-22-B1: Q-Band Waveguide Bandpass Filter, 30 to 50 GHz*, 2023. Datasheet. URL: `https://sftp.eravant.com/content/datasheets/SWF-40320340-22-B1.pdf`.

[109] Knowles Precision Devices. *B385MD0S: 38.5 GHz SMT Bandpass Filter*, 2023. URL: `https://www.knowlescapacitors.com/brands/dielectric-labs/b385md0s`.

[110] Knowles Precision Devices. *B424MB1S: 42.4 GHz SMT Bandpass Filter*, 2023. URL: `https://www.knowlescapacitors.com/brands/dielectric-labs/b424mb1s`.

[111] Inc. Pasternack Enterprises. *PE-W28F002: WR-28 Waveguide Bandpass Filter, 38–40 GHz*, 2023. URL: `https://shop.rojone.com/assets/brochures/PE-W28F002.pdf`.

[112] G. Orecchini, G. Schiavolini, P. Mezzanotte, S. Pauletto, A. Loppi, A. Beltramello, F. Dogo, D. Manià, V. Palazzi, G. Simoncini, L. Roselli, A. Gregorio, M. Fragiacomo, and F. Alimenti. Low-noise Ku-band receiver frontend with switchable SIW filters for cubesat applications. 2022. URL: `https://www.scopus.com/inward/record.uri?eid=2-s2.0-85145352980&doi=10.1109%2fICECS202256217.2022.9971113&partnerID=40&md5=6a26610e6eab98c10bbd659533081536`, `doi:10.1109/ICECS202256217.2022.9971113`.

[113] United Monolithic Semiconductors (UMS). *CHM2179b98F: Single-Channel Mixer MMIC (die)*, 2024. Datasheet. URL: `https://www.ums-rf.com/wp-content/uploads/2017/01/CHM2179b98F-Full-0301.pdf`.

[114] Peigen Zhou, Pinpin Yan, Jixin Chen, Zhe Chen, and Wei Hong. A 40–50 GHz RF front-end with integrated local oscillator leakage calibration. *Micromachines*, 14(11), 2023. URL: `https://www.mdpi.com/2072-666X/14/11/2105`, `doi:10.3390/mi14112105`.

[115] Jesse Baldwin and Dale Dubbert. Quadrature mixer LO leakage suppression through quadrature DC bias. *NASA STI/Recon Technical Report N*, 01 2002. `doi:10.2172/800958`.

[116] Francesco Adamo, Guendalina Simoncini, Simone Pauletto, Sergio Carrato, and Anna Gregorio. Design of a 17.3-21.2 GHz SATCOM upconverter based on COTS with low spurious emission. page 12 – 15, 2025. URL: `https://www.scopus.com/inward/record.uri?eid=2-s2.0-105000780140&doi=10.1109%2fSHARC63955.2025.10908962&partnerID=40&md5=3263a7e80f4b31848f04c078200d6464`, `doi:10.1109/SHARC63955.2025.10908962`.

[117] Andrzej Borys. When can a narrowband power amplifier be considered to be memoryless and when not? *International Journal of Electronics and Telecommunications*, 64(2):229–242, 2018. URL: `https://pdfs.semanticscholar.org/4d20/3879d535f9eb1a53d9e7967be382ba1f6011.pdf`, `doi:10.24425/119393`.

[118] Raviv Raich. *Nonlinear System Identification and Analysis with Applications to Power Amplifier Modeling.* PhD thesis, Georgia Institute of Technology, Atlanta, GA, USA, 2004. URL: `https://repository.gatech.edu/bitstreams/8f06685b-89d4-414c-ade8-999851669ea3/download`.

[119] Heinrich Meyr, Marc Moeneclaey, and Stefan A. Fechtel. *Digital Communication Receivers: Synchronization, Channel Estimation, and*

Signal Processing. Wiley Series in Telecommunications and Signal Processing. John Wiley & Sons, New York, 1998. `doi:10.1002/0471200573`.

[120] C. Rapp. Effects of hpa-nonlinearity on a 4-DPSK/OFDM system for digital radio. In *Proceedings of the Second European Conference on Satellite Communications (ECSC-2)*, pages 179–184, 1991.

[121] A. A. M. Saleh. Frequency-independent and frequency-dependent nonlinear models of twt amplifiers. *IEEE Transactions on Communications*, 29(11):1715–1720, 1981. `doi:10.1109/TCOM.1981.1094911`.

[122] MathWorks. *comm.PhaseNoise — Apply phase noise to baseband signal*, 2025. Accessed: 26-Oct-2025. URL: `https://www.mathworks.com/help/comm/ref/comm.phasenoise-system-object.html`.

[123] Amina Piemontese, Giulio Colavolpe, and Thomas Eriksson. Discrete-time models and performance of phase noise channels. *IEEE Open Journal of the Communications Society*, 5:2211–2225, 2024. `doi:10.1109/OJCOMS.2024.3383593`.

[124] Ana García-Armada. Understanding the effects of phase noise in orthogonal frequency division multiplexing (OFDM). *IEEE Transactions on Broadcasting*, 47(2):153–159, Jun 2001. `doi:10.1109/11.937489`.

[125] Gérard Maral, Michel Bousquet, and Zhili Sun. *Satellite Communications Systems: Systems, Techniques and Technology.* Wiley, 6th edition, 2020.

[126] ITU-R. Propagation data and prediction methods required for the design of earth-space telecommunication systems, 2019. Recommendation ITU-R P.618-14.

[127] ITU-R. Attenuation by atmospheric gases, 2019. Recommendation ITU-R P.676-12.

[128] Constantine A. Balanis. *Antenna Theory: Analysis and Design.* Wiley, 4th edition, 2016.

[129] Timothy Pratt, Charles W. Bostian, and Jeremy E. Allnutt. *Satellite Communications.* Wiley, 3rd edition, 2003.